

THULIUM DOPED FIBER LASER AND ITS APPLICATIONS

by

Masoud Mollae

Copyright © Masoud Mollae 2020

A Dissertation Submitted to the Faculty of the

JAMES C. WYANT COLLEGE OF OPTICAL SCIENCES

In Partial Fulfillment of the Requirements

For the Degree of

DOCTOR OF PHILOSOPHY

In the Graduate College

THE UNIVERSITY OF ARIZONA

2020

THE UNIVERSITY OF ARIZONA
GRADUATE COLLEGE

As members of the Dissertation Committee, we certify that we have read the dissertation prepared by **Masoud Mollaei**, titled *Thulium Doped Fiber Laser and Its Applications* and recommend that it be accepted as fulfilling the dissertation requirement for the Degree of Doctor of Philosophy.



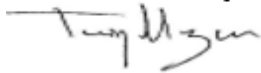
Professor Nasser N. Peyghambarian, Chair

Date: 5/14/20



Professor Xiushan Zhu

Date: 5/14/20



Professor Tariq Manzur

Date: 5/15/20

Final approval and acceptance of this dissertation is contingent upon the candidate's submission of the final copies of the dissertation to the Graduate College.

I hereby certify that I have read this dissertation prepared under my direction and recommend that it be accepted as fulfilling the dissertation requirement.



*Professor Nasser N. Peyghambarian
Dissertation Committee Chair
Wyant College of Optical Sciences*

Date: 5/14/20

ACKNOWLEDGEMENTS

I would like to express my deep and sincere gratitude to my research supervisor, Dr. Nasser Peyghambarian for putting his trust in me and for giving me the opportunity to do research and providing invaluable guidance throughout this research. Many thanks to Dr. Xiushan Zhu for his dedication in coaching me. He has taught me the methods to carry out the research and to present the research works as clearly as possible. It was a great privilege and honor to work and study under the guidance of these two great men. I would like to thank Dr. Tariq Manzur for his support and for accepting to be part of my Ph.D. dissertation committee.

From the University of Arizona, it was an honor to know Dr. Warren Beck, as his office door was always open to me as he kindly and patiently listened to my concerns and supported me in any way needed. Many thanks to Dr. Wright, Dr. Lucas, Minghong Tong, Shijie Fu, Julien, Junfeng Wang, Jingwei Wu, Khawlah Al Yahyaiei, Sasaan Showghi, Linda Schadler, Leonid Kotov, Michal Lukowski who have been there for me throughout my research and studies.

From NP Photonics, I would like to thank Dr. Arturo Chavez, Kort Wiersma , Jie Zong, Holly Griffin, Adam Escobar, Feng Kuo, Mehmet Akbulut, Michael Li, and Roger Trimmer for their guidance throughout my work at NP Photonics.

To my caring, loving, and supportive wife, Razeeyeh: my deepest gratitude. Your encouragement and patience when the times got rough are much appreciated and noted. It was a great comfort and relief to know that you were willing to provide management of our household activities alongside your own studies, while I completed my work. My heartfelt thanks.

I would also want to thank my sister and brother for their ongoing support, even though we are all in different parts of this world, they would always be there for me.

Last but not least, I am extremely grateful to my parents for their love and prayers, and tremendous sacrifices they have made for me. I have never heard them say “You cannot do it”, and I truly believe if it wasn’t for them and their belief in me, I would not be writing this acknowledgment today.

DEDICATION

I would like to respectfully and lovingly dedicate this dissertation to the memory of Dr. Mostafa Chamran whose spiritual support and guidance I have felt through each step of my life.

Table of Contents

List of Figures	8
List of Tables	15
Abstract.....	16
Chapter 1 Blue Laser Fiber Amplifier	19
1.1 Introduction.....	19
1.2 Spectroscopy of thulium doped ZBLAN for blue emission	22
1.2.1 ZBLAN glass	24
1.2.2 Blue emission of thulium doped ZBLAN.....	35
1.3 Single frequency blue laser fiber amplifier.....	45
1.4 Blue laser fiber amplifier for under water optical communication	69
Chapter 2 Tm ³⁺ -Doped Fluoride Fiber Laser at 785 nm.....	80
2.1 Introduction.....	80
2.2 Spectroscopy	81
2.3 Experiment, result and discussion.....	84
Chapter 3 Tm ³⁺ -Doped Silica Fiber Laser in 2 μm.....	92
3.1 Introduction.....	92
3.2 Spectroscopy of thulium doped silica for mid IR emission	95
3.3 Experimental results and discussion	99

Chapter 4 Magneto Optical Properties of Dy ³⁺ -Doped Glasses	106
4.1 Introduction.....	106
4.2 Theory of Faraday rotation	108
4.3 Glass fabrication and characterization	110
4.4 Experiment, result and discussion.....	118
Chapter 5 Magneto Optical Properties of New Chalcogenide Glasses.....	127
5.1 Introduction.....	127
5.2 Glass preparation and experimental setup	128
5.3 Result and discussion	132
Chapter 6 Summary and Prospect.....	138
6.1 Blue Laser Fiber Amplifier	138
6.2 Tm ³⁺ doped fluoride fiber laser at 785 nm.....	139
6.3 Magneto optical properties of Dy ³⁺ doped glasses and chalcogenide glasses	140
References.....	144

List of Figures

Fig. 1.1: Infrared transmission spectra for SiO ₂ , ZBLAN, and three different chalcogenide glasses[34].....	24
Fig. 1.2: thermal cycle for ammonium bi-fluoride process[38].	26
Fig. 1.3: Electronic structure of fluorine atom and fluoride ion.	27
Fig. 1.4: Intrinsic loss for a range of materials[37].....	29
Fig. 1.5: Transmission loss spectrum of a ZBLAN fiber[40].	30
Fig. 1.6: Refractive index vs wavelength of ZBLAN glasses[37].	31
Fig. 1.7: Materials dispersion of different fluoride glasses[41].	32
Fig. 1.8: Raman spectroscopy of ZBLAN sample at different temperature[42].	33
Fig. 1.9: Tm ³⁺ partial energy diagram.....	35
Fig. 1.10: Excitation spectra for 350 nm and 363 nm. The ¹ G ₄ absorption spectra is also shown[47].....	36
Fig. 1.11: The intensity dependence of 292, 350, 363 nm fluorescence[47].	37
Fig. 1.12: Partial energy diagram of Tm ³⁺ showing the cooperative up conversion (red lines)..	38
Fig. 1.13: Absorption cross section of Tm ³⁺ ZBLAN glass.....	39
Fig. 1.14: Bulk Tm ³⁺ ZBLAN glass emission setup.	40
Fig. 1.15: Measured fluorescence of Tm ³⁺ ZBLAN glass from ¹ G ₄ energy level.	41
Fig. 1.16: Lifetimes of different states of Tm ³⁺ in ZBLAN and silica glasses.	43
Fig. 1.17: Partial energy diagram of Tm ³⁺ related to the blue light emission.....	45
Fig. 1.18: Power spectra of amplified stimulated emission of Tm ³⁺ ZBLAN fiber pumped by 465 nm laser diode at different pump power.	46
Fig. 1.19: Absorption and emission cross section of Yb: Silica[52].	47

Fig. 1.20: Partial energy diagram of Yb related to lasing at 1125 nm.	48
Fig. 1.21: The schematic setup of all fiber laser operating at 1125 nm.	48
Fig. 1.22: Output laser with respect to launched pump power.	49
Fig. 1.23: The optical spectrum of fiber laser operating at 1125 nm.	50
Fig. 1.24: The schematic setup of external cavity laser diode Littrow configuration fiber coupled.....	51
Fig. 1.25: The output spectrum of GaN laser diode (blue), and external cavity Littrow configuration (red).	51
Fig. 1.26: Optical spectra of the Toptica laser at different applied currents.....	52
Fig. 1.27: (a) Microscope image of an end face and (b) 2D refractive index profile of the single- mode Tm ³⁺ -doped ZBLAN fiber.	53
Fig. 1.28: Cutback experiment, using 10 m Tm ³⁺ ZBLAN fiber.....	54
Fig. 1.29: Experimental setup of the all-fiber blue laser amplifier. Inset: the picture of the splice joint between the silica fiber and the fluoride fiber.	55
Fig. 1.30: Measured output power of the 478 nm fiber amplifier as a function of the launched pump power. Upper left inset: Optical spectra of the input and output of the fiber amplifier. Lower right inset: Single-frequency operation of the GaN diode laser confirmed with a scanning Fabry-Perot Interferometer.	56
Fig. 1.31: (a) 2D profile of the fiber amplifier output beam; (b) Cross-section of the output beam profile and its Gaussian fit.	57
Fig. 1.32: Optical spectra of the fiber amplifier when the pump power is 2 W (red curve) and 2.5 W (blue curve), respectively. The black curve: Transmission of a 1-cm thick Tm ³⁺ -doped ZBLAN glass.	58

Fig. 1.33: Loss due to fiber bending.	59
Fig. 1.34: Loss of bended fiber for different bending diameter as a function of wavelength.....	60
Fig. 1.35: (a) Experimental setup to study the effect of coiling;	61
Fig. 1.36: Optical spectrum of signal output when there is no pumping, 0.3 W pumping without coiling, and 0.3 W pumping with coiling.	62
Fig. 1.37: (a) Experimental setup to study the effect of coiling which input fiber and output fiber are coiled; (b) optical post was used to coil the fiber.	63
Fig. 1.38: Optical spectra of fiber amplifiers with pump power at 1.2 W and 1.5 W with bending and without bending.....	64
Fig. 1.39: The optical spectrum of fiber amplifier at different pump power when the output power is coiled.	65
Fig. 1.40: Output optical power as a function of pump power for a fresh fiber, 1st curing, and 2nd curing test.....	66
Fig. 1.41: The dynamic process of curing fiber by blue signal power as a function of time for the second time.	67
Fig. 1.42: Measured loss of 1 meter fresh (unpumped) fiber, 1 meter segment of the end and 1 meter segment of the beginning of the photodarkened amplifier fiber.	69
Fig. 1.43: Schematic design for creating a circular beam from an elliptical laser diode beam. ..	72
Fig. 1.44: The cross section of schematic design of the setup for coupling an elliptical beam to PM 460HP fiber and spot size evolution after lens #2, lens #3, and at the fiber.	73
Fig. 1.45: The amplified spontaneous emission of Tm ³⁺ - ZBLAN fiber. Inset: Amplified spontaneous emission at different pump powers.	74

Fig. 1.46: Amplified spontaneous emission of Tm^{3+} ZBLAN fiber pumped by 1210 nm laser diode.....	75
Fig. 1.47: Experimental setup for single mode fiber blue laser amplifier.	76
Fig. 1.48: a) 2D profile of the fiber output beam at 478 nm; (b) Cross section of the output beam profile and its Gaussian fit.	77
Fig. 1.49: Output power with respect to the launched pump power for 7.5 m Tm^{3+} -ZBLAN. Upper left: The optical spectrum of laser diode. Lower right: Mode field diameter of 980 HP, 780 HP, and gain fibers.	78
Fig. 2.1: Partial energy level diagram of Tm^{3+} and the transitions related to the laser emission at 785 nm.....	82
Fig. 2.2: Power dependence of upconversion emissions on pump power.	83
Fig. 2.4: Measured fluorescence of Tm^{3+} ZBLAN glass from $^1\text{G}_4$ energy level.	85
Fig. 2.5: Experimental setup of the all-fiber laser at 785 nm. Inset: microscopic image of the splice joint between the silica fiber and the ZBLAN fiber.	86
Fig. 2.6: Output power with respect to the launched pump power for the 3-m and 6-m Tm^{3+} ZBLAN fiber lasers.	87
Fig. 2.7: The measured absorption cross-section of Tm^{3+} ZBLAN glass.....	88
Fig. 2.8: Output optical spectrum of the all-fiber Tm^{3+} -doped ZBLAN laser measured in from 450 nm to 1000 nm. Inset shows the spectrum measured in the range from 783 nm to 786 nm with a resolution of 0.05 nm.	89
Fig. 2.9: Temporal evolution of signal power to test self-pulsing in μs interval. Inset: Temporal evolution of signal power to test self-pulsing in ms interval.	90

Fig. 3.1: Absorption and penetration depth in water and other biological tissue constituents for different wavelengths [79].	93
Fig. 3.2: Summary of shortest pulses durations observed over time in mode-locked Tm-doped fiber laser systems[87].	94
Fig. 3.3: Energy level diagram of Tm ³⁺ doped silica for 2 μm region emission.	97
Fig. 3.4: The optical absorption and emission spectra of thulium doped silica fiber[97].	98
Fig. 3.5: The cross relaxation process between two thulium ions labeled as “a” and “b”	99
Fig. 3.6: A schematic of laser setup operating at 1950 nm.	100
Fig. 3.7: The output signal as a function of pump power. Lower right inset: The spectrum of laser output.	101
Fig. 3.8: A schematic of laser setup operating at 1940 nm with PR FBG of 10% reflection.	101
Fig. 3.9: The output signal as a function of pump power for 1.6 m gain. Lower right inset: The residual pump as a function of pump power.	102
Fig. 3.10: The schematic setup for Q-switched laser ring cavity design.	103
Fig. 3.11: (a) The schematic setup of linear cavity design for Q-switched laser;(b) the average signal output power as a function of pump power.	104
Fig. 3.12: The pulse width and repetition rate of output signal.	105
Fig. 4.1: (a) 20 wt.% Dy ³⁺ doped germanate glass; (b) 20 wt.% Ce ³⁺ doped germanate phosphate glass;(c) 25 wt.% Tb ³⁺ doped phosphate glass.	110
Fig. 4.2: The transmission spectra of the three glasses of 20 wt.% Dy ³⁺ doped germanate glass, 20 wt.% Ce ³⁺ doped germanate phosphate glass.	111
Fig. 4.3: Transmission spectra of 40 and 50 wt.% Dy ₂ O ₃ doped phosphate glass.	112

Fig. 4.4: The refractive indices of Dy ³⁺ -doped phosphate glasses measured at 633, 816, 1305, and 1555 nm and the fitting curves with Cauchy equation.....	113
Fig. 4.5: Optical transmission spectra of Dy ³⁺ -doped borate glass samples with different concentrations.	115
Fig. 4.6: XRD measurement result for the Dy75 glass.	115
Fig. 4.7: The refractive indices of Dy ³⁺ -doped borate glasses measured at 633, 816, 1305, and 1555 nm and the fitting curves with Cauchy equation.	116
Fig. 4.8: The refractive indices of the Dy ³⁺ -doped borate glasses as a function of Dy ³⁺ concentration at (a) 633 nm; (b) 816 nm; (c) 1305 nm; (d) 1555 nm.	117
Fig. 4.9: The schematic of the experimental setup for the Verdet constant measurement.	119
Fig. 4.10: Verdet constant measurement for 20 wt.% Ce doped germanate-phosphate glass at 976 nm.....	120
Fig. 4.11: The Verdet constant of Tb ³⁺ doped phosphate glass at different wavelengths. Fitted curve is based on Van Vleck-Hebb single oscillator model.	121
Fig. 4.12: Verdet constants of the Dy ³⁺ -doped borate glasses with different concentrations measured at 478, 633, 976, 1480, and 1950 nm. Inset shows the results at 1480 and 1950 nm in a small scale.	122
Fig. 4.13: Inverse of the Verdet constant as a function of squared wavelength for Dy40, Dy50, Dy60, Dy65 and Dy75. Inset shows the experimental data and fitted lines at a squared wavelength range of 0-1 μm ²	124
Fig. 4.14: The Verdet constants of Dy40, Dy50, Dy60, Dy65, and Dy75 at 478nm, 633 nm, 976 nm, 1480nmn, and 1950 nm.	125

Fig. 4.15: The Verdet constants of 40 and 50 wt.% Dy ₂ O ₃ doped phosphate glasses at different wavelengths.....	125
Fig. 5.1: Optical transmission loss spectra of Te ₂₀ As ₃₀ Se ₅₀ , Ge ₁₀ Se ₉₀ , and Ge ₂₅ As ₁₅ S ₆₀ . The crossing point of two dashed lines show the bandgap absorption edge.....	129
Fig. 5.2: IR transmission spectra of Te ₂₀ As ₃₀ Se ₅₀ , Ge ₁₀ Se ₉₀ , and Ge ₂₅ As ₁₅ S ₆₀	130
Fig. 5.3: The schematic setup for Verdet constant measurement.	131
Fig. 5.4: Verdet constants of the three glasses measured at 1240, 1476, 1555, and 1950 nm. The dashed lines are the fitting curves.	133
Fig. 5.5: Verdet constants of the three glasses were plotted at the $\lambda * 2$ for the light wavelengths of 1240, 1476, 1555, and 1950 nm.	134
Fig. 5.6: FOMs of Te ₂₀ As ₃₀ Se ₅₀ , Ge ₂₅ As ₁₅ S ₆₀ , and Ge ₁₀ Se ₉₀ glasses as a function of the wavelength. The solid dots show the measured FOM.....	135
Fig. 5.7: Refractive index of Te ₂ As ₃ Se ₅ glass measured by <i>Aio et al.</i> and the dashed line is fitted Cauchy equation. Inset shows the magneto optical anomaly factor as a function of wavelength.	136
Fig. 6.1: Two stages fiber amplifiers to increase the output power.	139
Fig. 6.2: Dual wavelength pumping schemes for 785 nm fiber laser	140
Fig. 6.3: Magnetic field distribution of cylindrical N52 magnets with 5mm inner radius, 120 mm outer radius and thickness of 20 mm.	141
Fig. 6.4: Faraday rotation as a function of thickness of magnetic tube for Dy ₇₅ glass.....	142
Fig. 6.5: Faraday rotation as a function of thickness of magnetic tube for tellurium based glass.	143

List of Tables

Table 1.1: Fluorozirconate compositions[37]	25
Table 1.2: Comparison of basic properties between silica and ZBLAN glasses[17].	28
Table 1.3: Minimum dispersion wavelength of different materials.....	32
Table 1.4: Summary of laser wavelength and pump wavelength of rare earth doped ZBLAN fiber laser.	34
Table 1.5: The branching ratio of different optical transitions of Tm^{3+} ZBLAN glass.....	42
Table 1.6: Measured lifetimes of 3F_4 , and 3H_4 manifolds for thulium doped silica and ZBLAN[49].....	44
Table 3.1: Basic properties of silica glass[17].	96
Table 3.2: signal output as a function of repetition rate.	103
Table 4.1: The coefficient of Cauchy equation for Dy^{3+} -doped phosphate glasses.....	113
Table 4.2: Coefficients of the Cauchy equation for Dy^{3+} -doped borate glasses.....	116

Abstract

Laser as one of the core components of the photonics industry plays a crucial role in keeping the compound annual growth rate (CAGR) of this industry much higher than the average of global GDP growth. The exceptional performance of fiber laser and its advantages, including robustness, excellent heat dissipation capability, compactness, high beam quality, free from alignment, low cost, etc. are the reasons that fiber laser shares about 50% of laser market revenue. The extensive applications of fiber lasers in industry, medicine, research, defense and other areas make them demanding for the future of our lives. Thulium doped fiber laser has been demonstrated to be able to operate from ultraviolet to mid infrared. The work presented in this dissertation, includes demonstration of single frequency blue laser fiber amplifier using thulium doped fiber; study of thulium doped fiber laser operating at 785 nm; investigation of 2 μm thulium doped fiber laser and magneto optical glasses for all fiber optical isolator and circulator in 2 μm region.

In chapter 1, the performance of blue laser fiber amplifier was studied. A single frequency blue laser all-fiber amplifier was demonstrated for the first time. Over 150 mW continuous-wave single transverse-mode, and single longitudinal mode blue laser output was obtained with a 10-m 1000 ppm thulium-doped fluoride fiber pumped by a 1125 nm fiber laser at a power of 2 W. The output power was limited due to the onset of the competitive lasing at 784 nm. The concept of blue laser MOPA for underwater optical communication system was also demonstrated by using a GaN diode laser at 478 nm as the seed laser and a 7.5 m Tm^{3+} -doped ZBLAN fiber amplifier as the power amplifier. A maximum output power of 235 mW was obtained. Photo-darkening and photo-curing of the thulium-doped fiber amplifier were also studied and analyzed.

In chapter 2, all-fiber single-transverse-mode laser oscillators operating at 785 nm were demonstrated by splicing a 0.1 mol% Tm^{3+} -doped fluoride fiber with a core diameter of 4 μm and a numerical aperture of 0.07 to a pair of silica fiber Bragg gratings. About 500 mW of continuous-wave single transverse mode laser output at 784.5 nm with a 3-dB spectral bandwidth of 0.2 nm was obtained by upconversion pumping a 3-m-long gain fiber at 1125 nm. Our experiments show that the ground-state absorption of Tm^{3+} at 785 nm is the origin of low efficiency in previous reports. The efficiency of this all-fiber laser can be improved by using a gain fiber with optimized overlap between the laser, the pump and the fiber core, and employing new pumping schemes that deplete the ground state sufficiently.

In chapter 3, thulium doped fiber laser operating in CW regime with several watts output power in 2 μm region was demonstrated. 793 nm high power diode pump was used to pump the gain fiber and the slope efficiency of 35% was obtained. Ring cavity design and linear cavity design of thulium doped fiber Q-switched laser operating in 2 μm region were also demonstrated.

In chapter 4, Dy^{3+} doped glass as a promising paramagnetic glass operating in mid IR region for magneto optical applications was studied. Due to their large effective magnetic moment, Dy^{3+} -doped materials have attracted much interest for magneto-optical applications. Highly Dy^{3+} -doped glasses with concentrations from 40 wt.% to 75 wt.% were fabricated and their magneto-optical properties were investigated. A Verdet constant of -7.94 rad/T/m (-455 deg/T/m) at 1950 nm was measured with the 75 wt.% Dy^{3+} -doped glass. This is the highest reported Verdet constant around 2 μm for a paramagnetic glass. Our experimental results show that highly Dy^{3+} -doped glasses are promising isotropic magneto-optical materials for applications in the 2 μm wavelength region.

In chapter 5, magneto optical properties of chalcogenide glasses operating in 2 μm wavelength region were studied. A Verdet constant of 870 deg/T/m at 1950 nm with the figure of merit of more than 500 deg/T, which is the highest value reported in glass materials at this wavelength, was measured for tellurium-arsenic-selenium glass ($\text{Te}_{20}\text{As}_{30}\text{Se}_{50}$). Compared to other chalcogenide glasses, such as $\text{Ge}_{10}\text{Se}_{90}$ and $\text{Ge}_{25}\text{As}_{15}\text{S}_{60}$, $\text{Te}_{20}\text{As}_{30}\text{Se}_{50}$ glass exhibits higher Verdet constants, broader mid-infrared transparency window, and longer infrared absorption edge, making it a very promising material to fabricate magneto-optical devices for mid-infrared applications.

Chapter 1 Blue Laser Fiber Amplifier

1.1 Introduction

A broad application of blue coherent light demands substantial research and study on building stable and robust blue laser. For instance, due to low absorption of ocean water in 450 - 490 nm; a low-cost, rugged, and high energy blue laser source must be developed for widespread and rapid airborne bathymetric LIDAR[1], or since the wavelength of blue light is shorter compared to green and red, it is highly demanded for high density optical data storage [2], and high resolution imaging[3]. Blue laser can also be used for pollution monitoring [4], and medical diagnostic for detecting cancerous and precancerous cells[5]. Moreover, blue laser is a very promising light source for the underwater communication system[6].

There are different type of lasers that can emit blue light. Among gas lasers, argon ion (Ar^+) laser and helium-cadmium (He-Cd) laser can emit blue light[7]. They can emit blue light at different wavelengths such as 488, 458, 477, 497, and 442 nm. The ground state of Ar^+ is obtained by changing electron state configuration from $3p^6$ to $3p^5$. To obtain blue laser, Ar^+ will be excited to $4p$ and the lasing occurs on of $4p \rightarrow 4s$ transition. Since both the $4s$ and $4p$ levels actually consist of many sub-levels, the Ar^+ laser is found to oscillate on many lines, the most intense being in the green (514.5 nm) and in the blue (488 nm) [7]. He-Cd laser is also able to operate at 442 nm [8]. Dye lasers can also operate in blue region. They utilize an active medium including a solution of an organic dye in a liquid solvent such as methyl alcohol, ethyl alcohol, glycerol, or water[7]. For example, coumarin 2 can oscillate around 450 nm. Semiconductor laser is one of the most important class of lasers for different applications. The first demonstration of Gallium- nitride (GaN) based laser diode emitting around 400 nm was done by Nakamura's group[9] Gallium-

nitride based blue emitting diode lasers can operate in a wide range of blue region from 400 to 480 nm[10]. But the beam quality is always degraded and the power scaling is usually limited by the thermal issues of semiconductor. Frequency doubling can also be used to generate coherent blue light. Nd:YAG operating at 946 nm can generate light at 473 nm by use of nonlinear crystal with high second harmonic generation capability [11], Nd:YVO₄ emission at 914 can be utilized to generate 457 nm [12], High-power optically pumped VECSELs can also be used to generate blue light by intra-cavity frequency doubling method[13]. But harmonic generation lasers are very sensitive to the environment and lack of agile wavelength tunability. Mode locked Ti:sapphire lasers can be also be used as the pump in frequency doubling to generate a tunable coherent light from 375-435 nm[14]. However, power scaling of this type of laser is limited by the thermal-optical problems and crystallographic properties of Ti:Sapphire. In addition, Ti:Sapphire laser requires careful alignment and frequent maintenance.

Among different methods to generate blue light, fiber lasers are very promising. Fiber lasers have advantages including power scalability, low thermal effect, high beam quality, compactness, and free from alignment, etc. Praseodymium ion (Pr³⁺) and thulium (Tm³⁺) are the two rare earth ions that can be doped into fiber and generate blue light[15,16]. Pr³⁺ is usually used for longer blue wavelength like 490 nm, while Tm³⁺ usually has better emission efficiency around 480 nm.

Due to low phonon energy of ZrF₄-BaF₂-LaF₃-AlF₃-NaF (ZBLAN) glass, thulium doped ZBLAN has several radiative transitions, which are non-radiative in Tm³⁺-doped silica glass [17]. For instance, Tm³⁺-ZBLAN can emit light at 2.3 μm (³H₄ → ³H₅) in the mid-infrared [18], at 800 nm (¹G₄ → ³H₅) in the near-infrared [19], and at 480 nm in the visible (¹G₄ → ³H₆) [20]. Among these emissions from Tm³⁺-ZBLAN, as discussed above blue light is of great interest. Because of many different advantages of fiber lasers as mentioned above, several research groups have studied blue

Tm³⁺-ZBLAN fiber lasers in 1990s. The blue upconversion emission in Tm³⁺-ZBLAN was first reported by *Allain et al.* in 1990 [21]. They showed upconversion fiber laser, lasing at 450 nm and 480 nm at the temperature of 77 K. Two years later, *Grubb et al.* demonstrated an upconversion blue laser with Tm³⁺-ZBLAN fiber at room temperature for the first time [22]. 2 m 1000 ppm Tm³⁺-ZBLAN fiber with output coupler reflectivity of 90% was used and an output power of 57 mW at 480 nm was achieved by using a Nd³⁺:YAG pump at 1120 nm. They observed a 46 mW threshold pump power, slope efficiency of 18% against coupled pump power and slope efficiency of 32% with respect to the absorbed pump power. They also observed the lasing wavelength varies between 478 nm to 481 nm depending on the output coupling. In 1995, *Sanders et al.* were able to increase the output power of Tm³⁺-ZBLAN fiber laser to 106 mW with 890 mW incident pump power, using two tunable laser diodes at the pump wavelength of 1130 nm with 2.5 m 1000 ppm Tm³⁺-ZBLAN fiber and output mirror with 80% reflectivity at the lasing wavelength [23]. In 1997, another group in Germany tried to increase the efficiency and power level of Tm³⁺-ZBLAN fiber laser by co-doping with Yb³⁺. The doping level of Tm³⁺ and Yb³⁺ were 1500 ppm and 5000 ppm respectively. The pump wavelength was chosen to be 1064 nm to excite Yb³⁺ then utilize energy transfer phenomena between Yb³⁺ and Tm³⁺ [24]. They used 1064 nm Nd³⁺:YAG laser as the pump source, due to its power scalability compare to the available laser diodes, and higher absorption at 1064 nm compare to 1122 nm Nd³⁺:YAG laser for Yb³⁺. But the achieved maximum power was 100 mW with about 6.6% slope efficiency. The output coupler transmission at 482 nm was 30% and it was highly reflective for the pump wavelength. At the same year, *Paschotta et al.* were able to achieve 230 mW at 481 nm with 1600 mW incident pump power, pumping by Nd³⁺:YAG laser operating at 1123 nm, using 2.2 m 1000 ppm Tm³⁺-ZBLAN fiber with 50% reflectivity of output coupler at 481 nm and high transmission for pump wavelength[25].

All of the previous experiments used mirrors to define the feedback cavity which requires a significant redesign to improve the mechanical stability and transition from a lab environment. They also used multimode gain fibers for blue laser with the cutoff wavelength of more than 800 nm. So, a robust and mechanically more reliable blue coherent light source with a high beam quality is highly needed. In addition to a single spatial mode, single longitudinal mode blue lasers are in great demand for optical metrology, interferometry, high-order harmonic generation, quantum cryptography, high resolution spectroscopy, and under-sea communication. In this research we report the first demonstration of an all-fiber blue laser amplifier with single frequency and single transverse mode output.

1.2 Spectroscopy of thulium doped ZBLAN for blue emission

Spectroscopy studies how matter interacts with electromagnetic waves. The origin of spectroscopy goes to many years ago when visible light was dispersed by a prism. These days, spectroscopy became a fundamental tool to investigate physical and electronic structure of matter at atomic scale. So, the spectroscopy of rare earth ions has become the backbone of different fields from material design to astronomy. The difference in performances of photonic devices such as slope efficiency of a laser, two photon absorption, refractive index, gain of amplifier, lasing wavelength, saturation intensity, pump wavelength is rooted in the spectroscopic properties of the materials.

Since the first demonstration ruby crystal laser emission[26], many different ceramics, crystals, and glasses have been fabricated as the hosts for rare-earth ions to generate coherent emissions at different wavelengths. Whereas crystals have a very narrow bandwidth laser transition, glasses have broad laser transitions. Broad laser transitions are quite vital for wavelength tuning and

ultrashort pulses generation. The other advantage of glasses compared to the crystals is a high wavelength tolerance for the pump sources. Most importantly, single-mode optical fibers, as the most flexible and compact gain media for high-efficiency and excellent beam-quality laser generation, are mostly drawn from glasses. There is different type of glasses that can be drawn into fiber to be utilized as a gain medium or just a waveguide from ultraviolet (UV) to mid-infrared. Silicate, phosphate, fluoride, and chalcogenide are the most common glasses for fiber optics applications.

Silica fiber which is made from silicate glass has been massively used for optical fiber communication. These fibers are hosts for rare-earth ions with usually low loss, high tenability, and strong strength. The high solubility of rare earth ions in phosphate glass enables this glass to be drawn for high gain fibers. Watt level single longitudinal mode output can be delivered with high-gain per unit fiber length (~ 5 dB/cm) and short length that can support single longitudinal mode[27]. chalcogenide glasses have low phonon energy and good mid-infrared transparency. So, they are good candidates for applications in mid-infrared regions where silicate and phosphate fibers are very lossy compared to chalcogenide fibers. Chalcogenide fibers are usually used for nonlinear optics application due to their high nonlinearity[28,29]. The available rare earth doping levels in chalcogenide glasses are low (~ 0.1 mol%) which leads to relatively low efficiency and output power for laser application[30,31]. Fluoride glasses are very good candidates for fiber lasers in visible and mid-infrared regions where again silicate and phosphate fibers are not able to operate as efficient as fluoride fibers. fluoride fibers have higher doping levels and lower background loss compare to chalcogenide fibers. They also have higher stability and strength. In terms of power scalability, fluoride fiber lasers with more than tens of watt level output power have been reported[32,33]. Fig. 1.1 shows the transmission spectra of SiO_2 ,

ZBLAN, and three different chalcogenide glasses[34]. The transmission window of ZBLAN is almost twice of silica glasses and for chalcogenide is beyond 10 μm .

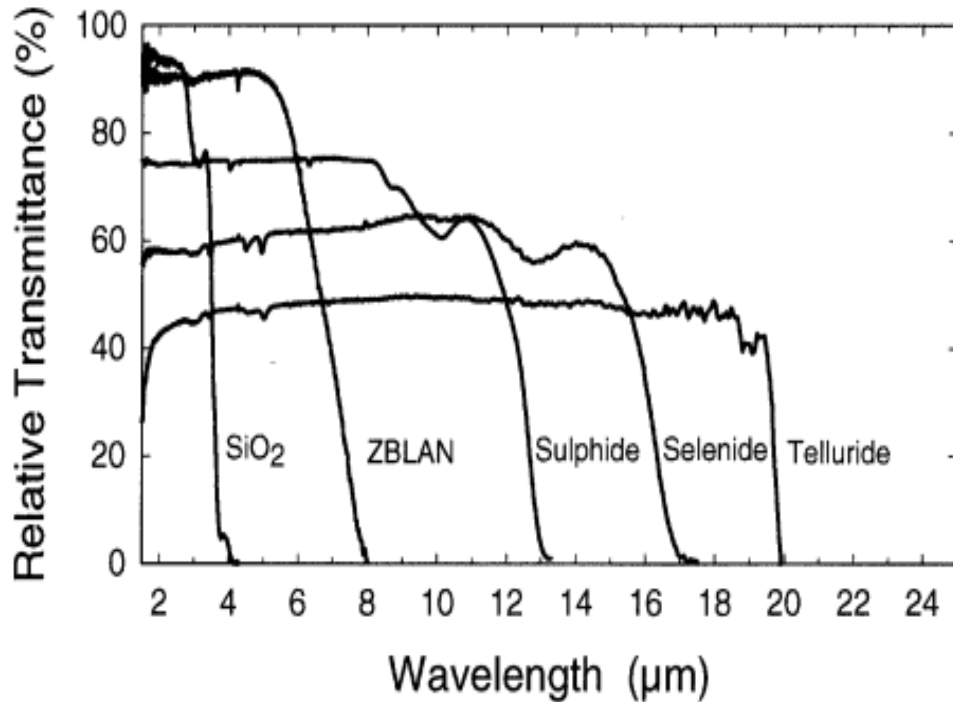


Fig. 1.1: Infrared transmission spectra for SiO₂, ZBLAN, and three different chalcogenide glasses[34].

In this section we will discuss and investigate the ZBLAN glass properties and spectroscopic properties of thulium doped glass with a focus on thulium doped ZBLAN glass.

1.2.1 ZBLAN glass

Fluoride glasses are non-oxide optical glasses composed of fluorides of various metals such as ZrF₄, HfF₄, InF₃, PbF₂, BaF₂, LaF₃, AlF₃, NaF. In 1975 the first report of fluoride glasses was published by Poulain *et al.*[35]. ZrF₄-BaF₂-NaF was the glass system observed and NdF₃ was doped to the glass matrix to obtain the mixture of ZrF₄-BaF₂-NaF-NdF₃. ZBLAN glasses with

the molar composition of 53% ZrF₄, 20% BaF₂, 4% LaF₃, 3% AlF₃, and 20% NaF is one of the most stable glass for optical fiber applications. It should be note that the ratio of composition might be changed due to the needed properties for the glass. The first group reported a stable ZBLAN glass was in 1981[36]. More component in fluoride glass makes the glass more stable. Table 1.1 shows the transition temperature of different fluoride glasses along with the difference between crystallization temperature and transition temperature[37]. ZBLAN and ZBLAL are the most stable glasses among fluorozirconate glasses with more components and bigger T_x-T_g .

Table 1.1: Fluorozirconate compositions[37]

Composition	Acronym	T _g (C)	T _x -T _g (C)
ZrF ₄ -BaF ₂	ZB	295	32
ZrF ₄ -BaF ₂ -LaF ₃	ZBL	399	46
ZrF ₄ -BaF ₂ -AlF ₃	ZBA	311	45
ZrF ₄ -BaF ₂ -AlF ₃ -NaF	ZBAN	260	65
ZrF ₄ -BaF ₂ -LaF ₃ -AlF ₃	ZBLA	302	57
ZrF ₄ -BaF ₂ -LaF ₃ -AlF ₃ -LiF	ZBLAL	250	107
ZrF ₄ -BaF ₂ -LaF ₃ -AlF ₃ -NaF	ZBLAN	265	93

ZBLAN glasses can be prepared by three process, ammonium bi-fluoride, anhydrous fluoride and the sol gel[38]. Ammonium bi-fluoride process uses oxide and fluoride as the starting materials along with ammonium bi-fluoride which plays the role of fluorinating agent in platinum, gold or glassy carbon crucibles. During the fluorinating step oxides are converted to fluoride. Oxides are converted to fluoride during the fluorinating step. After this step the fluorides are melted, refined and casted. For casting, the metallic mold needs to be preheated at a temperature slightly below

the glass transition temperature. The molten glass is poured in metallic mold pre-heated at a temperature close but below glass transition temperature. For ZBLAN glass melting, the furnace needs to be placed in a glovebox where both moisture and oxygen concentrations are very low. The thermal cycle for ammonium bi-fluoride process is shown in Fig. 1.2[38].

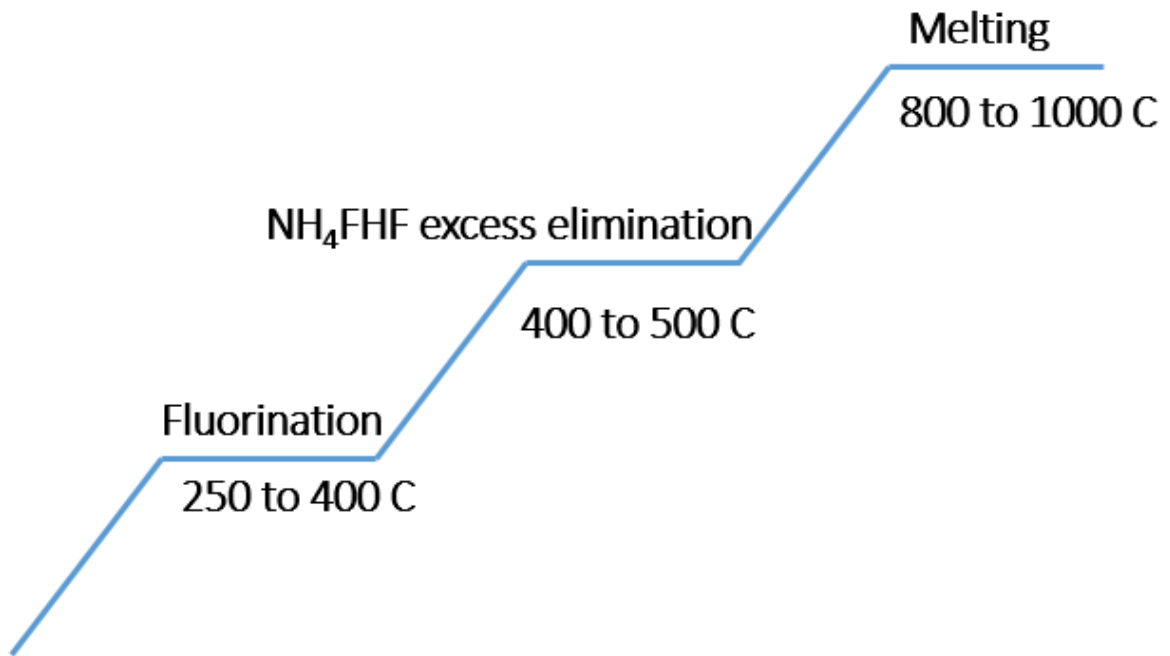


Fig. 1.2: thermal cycle for ammonium bi-fluoride process[38].

In anhydrous fluoride, all the starting materials must be highly pure fluoride. Highly pure fluorides are weighed according glass compositions and mixed uniformly then heated at temperature ranging from 250 to 400 °C for 1 to 2 hours. Next step is to increase the temperature to the melting point ranging from 800 to 1000 °C for 1 to 2 hours. Again, like pervious process the mixing and melting process need to be done in controlled atmosphere in a glove box with the lowest concentration of H₂O. Since, sol gel method is a difficult process and requires more

complicated and expensive fluorinating setup, is not very common for fabricating ZBLAN glass. More information about this process can be found in a work done by M. Saad[38].

ZBLAN glass has weaker bonding compared to silica glass which is due to electronic structure of fluoride ion. The fluorine atomic structure is shown in Fig. 1.3. Fluorine has a very strong tendency to attract an electron with electronegativity of 3.98. With pairing one electron fluorine can complete its p shell. Consequently, bonding energy of fluoride is not as strong as SiO_2 , which causes longer infrared absorption edge. On the other hand the stability and hardness of ZBLAN is not as good as silica[17].

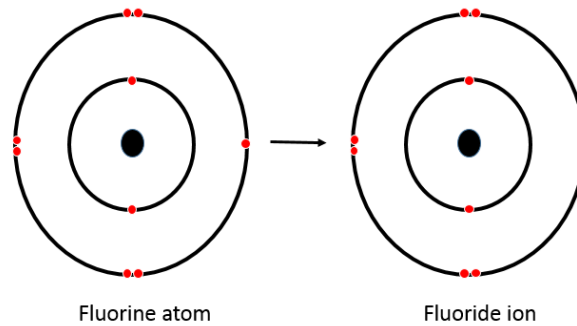


Fig. 1.3: Electronic structure of fluorine atom and fluoride ion.

The thermal conductivity and thermal diffusivity of silica glasses are significantly larger than ZBLAN[37]. Small thermal diffusivity leads to small cooling rate which is in the case ZBLAN. ZBLAN has lower cooling rate compared to silica[39]. Slow cooling rate usually leaves more time for atomic rearrangement which can introduce some crystallites into the sample. Although, the cooling rate of ZBLAN is slow, homogenous nucleation rate is very low[37]. X. Zhu *et al.* compared the basic properties of ZBLAN and silica[17]

Table 1.2: Comparison of basic properties between silica and ZBLAN glasses[17].

Glass Property	Silica	ZBLAN
Transmission range (μm)	0.16-4	0.22-8
Maximum phonon energy(cm^{-1})	1100	600
Transition temperature (C)	1175	260
Specific heat (J/(g.K))	0.179	0.151
Thermal conductivity (W/(m.K))	1.38	0.628
Expansion coefficient ($10^{-6}/\text{K}$)	0.55	17.2
Density (g/cm^3)	2.20	4.33
Knoop hardness (kg/mm^2)	600	225
Fracture toughness ($\text{MPam}^{1/2}$)	0.72	0.32
Poisson's ratio	0.17	0.17
Young's modulus (Gpa)	70	58.3
Shear's modulus (Gpa)	31.2	20.5
Bulk's modulus (Gpa)	36.7	47.7
Refractive index (@ 589 nm)	1.458	1.499
Abbe number	68	76
Zero material dispersion wavelength (μm)	1.3	1.6
Nonlinear index (10^{-13} esu)	1	0.85
Thermo optics coefficient ($10^{-6}/\text{K}$)	11.9	-14.75

In fiber optics, especially optical fiber communication, background loss is a big concern for long optical fibers. So the optical glasses should have a low background loss. Background loss is usually result of intrinsic scattering, multiphonon absorption, electronic transition, and impurities. The dominant intrinsic scattering is Rayleigh scattering, but Raman and Brillouin scattering are also important. For short wavelengths, electronic transition and Rayleigh scattering have the main impact in attenuation of light propagation, while in long wavelength multiphonon absorption plays the main role. Impurities can increase the optical loss in short and long wavelengths,

depending on the type of impurity. In order to shift the infrared edge to longer wavelength which multiphonon absorption is the main effect, using materials with lower bonding energy and higher reduced mass is effective. And since ZBLAN has low bonding energy as discussed above and it is a Heavy metal fluoride glass, it can shift the infrared edge and have lower attenuation in mid-IR.

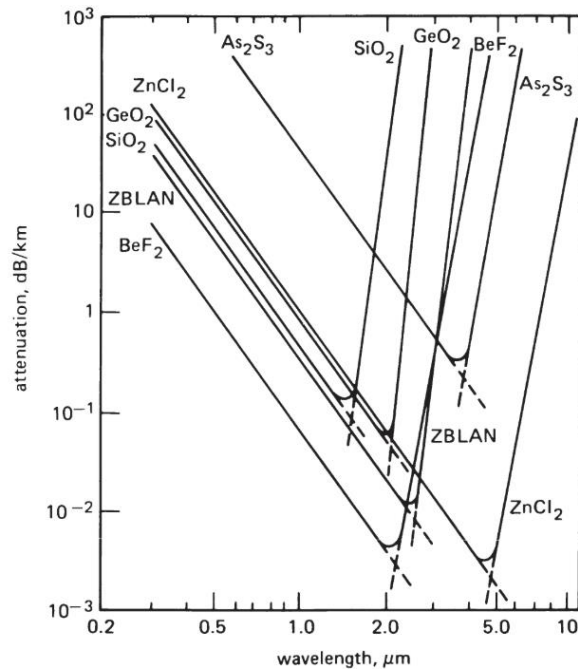


Fig. 1.4: Intrinsic loss for a range of materials[37]

The minimum intrinsic loss of different materials including silica and ZBLAN is shown in Fig. 1.4[37]. The minimum loss for SiO_2 was calculated to be 0.14 dB/km around 1.6 μm and for ZBLAN glass was 0.02 dB/km around 2.5 μm [37]. Although the theoretical loss for ZBLAN glass is significantly less than 1 dB/km, the minimum demonstrated loss is around 1 dB/km in 30 m fiber length with 20 μm core diameter and 120 μm cladding diameter as shown in Fig. 1.5[40]. The commercial loss for silica fiber is around 0.2 dB/km around 1.5 μm , and the available ZBLAN fibers suffer from transmission loss of more than 10 dB/km. The reason that

loss is high at ZBLAN fibers is due to the extrinsic scattering. Controlling purity in ZBLAN glass fabrication is very hard, which causes extrinsic scattering. These impurities are usually transition metals such as Fe, Cu, Ni,; rare earths such as Nd, Tb, Er; OH, H₂O; and other species like CO, CO₂.

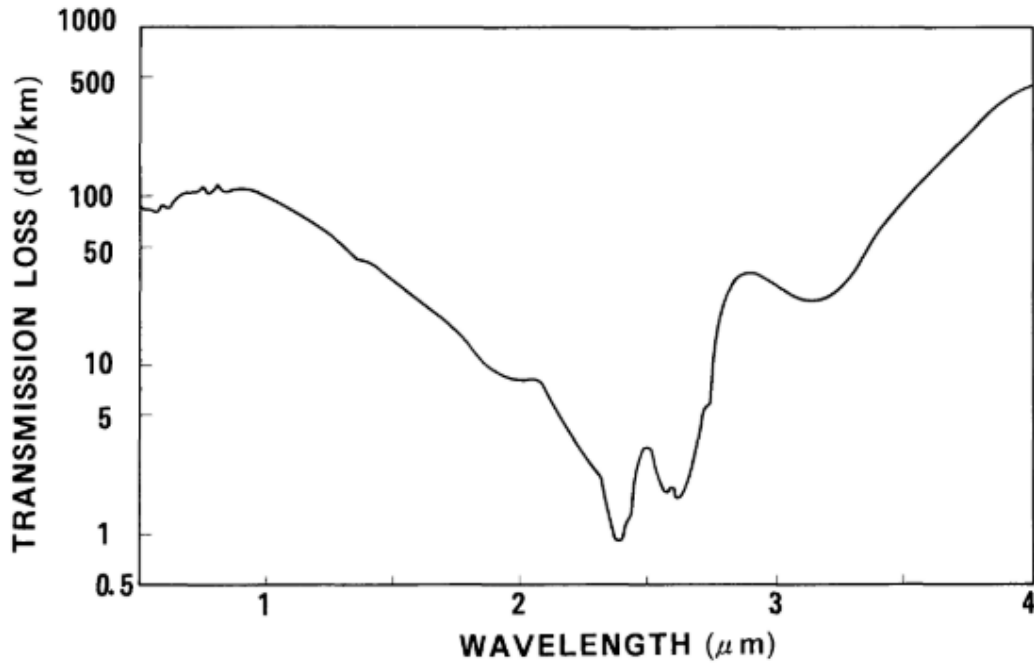


Fig. 1.5: Transmission loss spectrum of a ZBLAN fiber[40].

The refractive index of ZBLAN glass is in the range of 1.47-1.54 at the sodium D wavelength, which is in the same range as silica glasses[37]. In order to increase the refractive index of ZBLAN glass, heavy polarizable fluoride such as, PbF₂, BiF₃ can be used, and NaF, AlF₃ can reduce the refractive index of the ZBLAN glass. Fig. 1.6 shows the refractive index of different ZBLAN glasses versus wavelength[37].

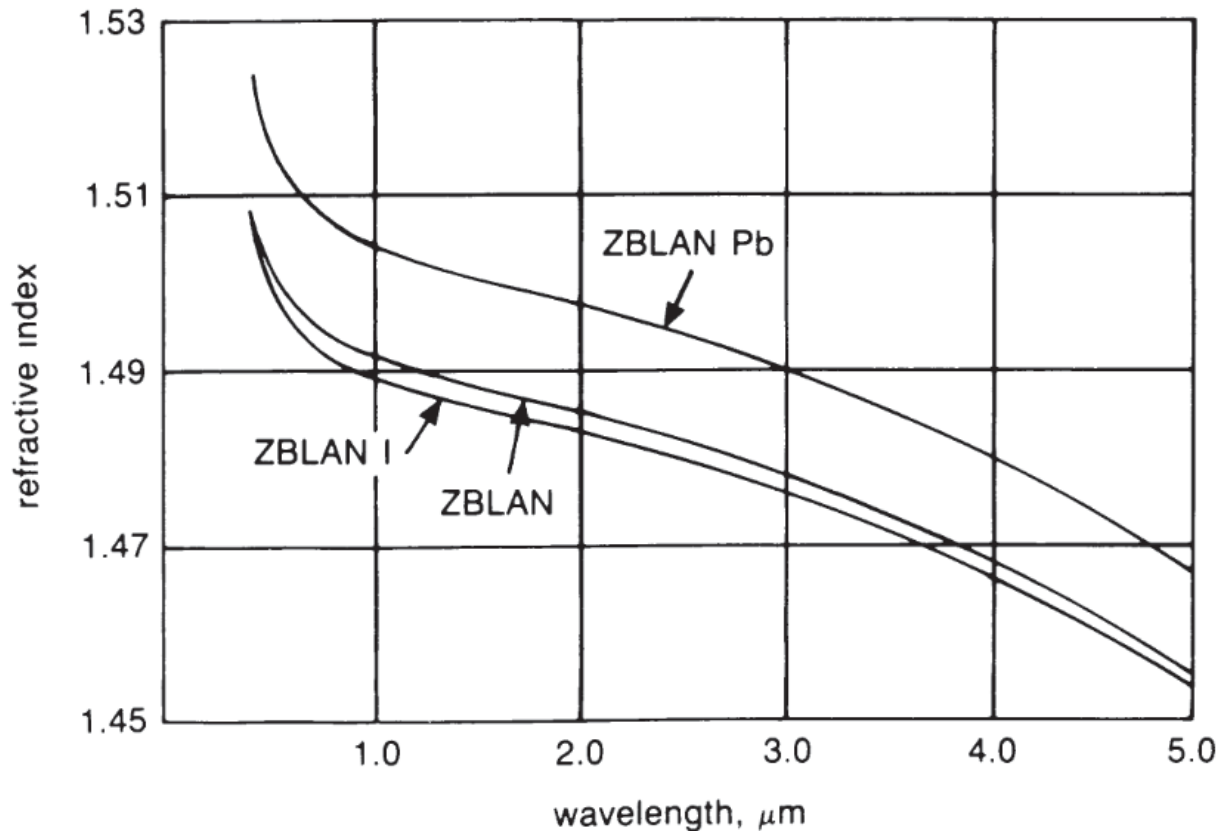


Fig. 1.6: Refractive index vs wavelength of ZBLAN glasses[37].

The material dispersion of different fluoride glass is illustrated in Fig. 1.7[41]. The zero dispersion wavelength of ZBLAN glass is around 1700 nm which is higher than silica glasses with zero dispersion wavelength of 1300 nm.

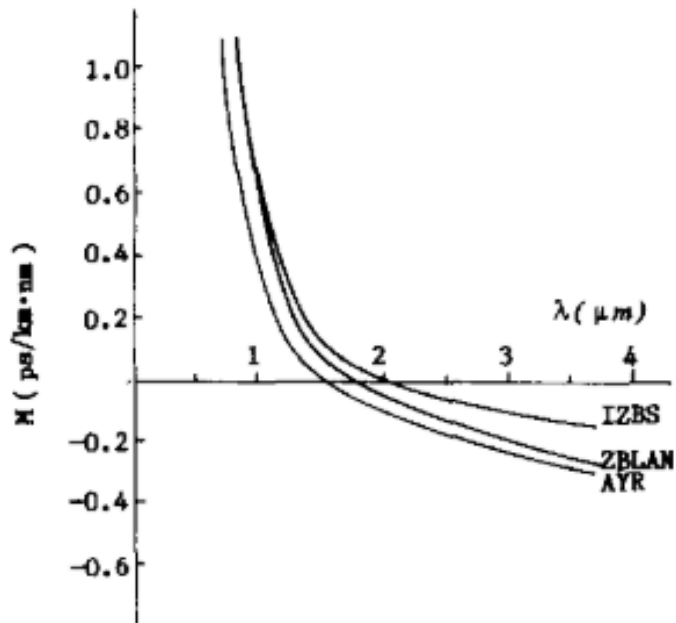


Fig. 1.7: Materials dispersion of different fluoride glasses[41].

The minimum dispersion wavelength of different materials are listed in Table 1.3. It should be noted that to find the real zero dispersion wavelength in fiber the waveguide dispersion wavelength needs to be taken into the account.

Table 1.3: Minimum dispersion wavelength of different materials.

Material	λ_0 (nm)
SiO ₂	1270
GeO ₂	1690
BeF ₂	1030
Zr ₂ BaF ₁₀	1630
ZnCl ₂	3260
GeS ₂	4100

Raman spectroscopy of pure ZBLAN sample is shown Fig. 1.8[42]. The sample is heated from room temperature to 357 °C. As it can be seen the maximum phonon energy is about 600 cm^{-1} . As the temperature increases some signature of crystallization starts to appear.

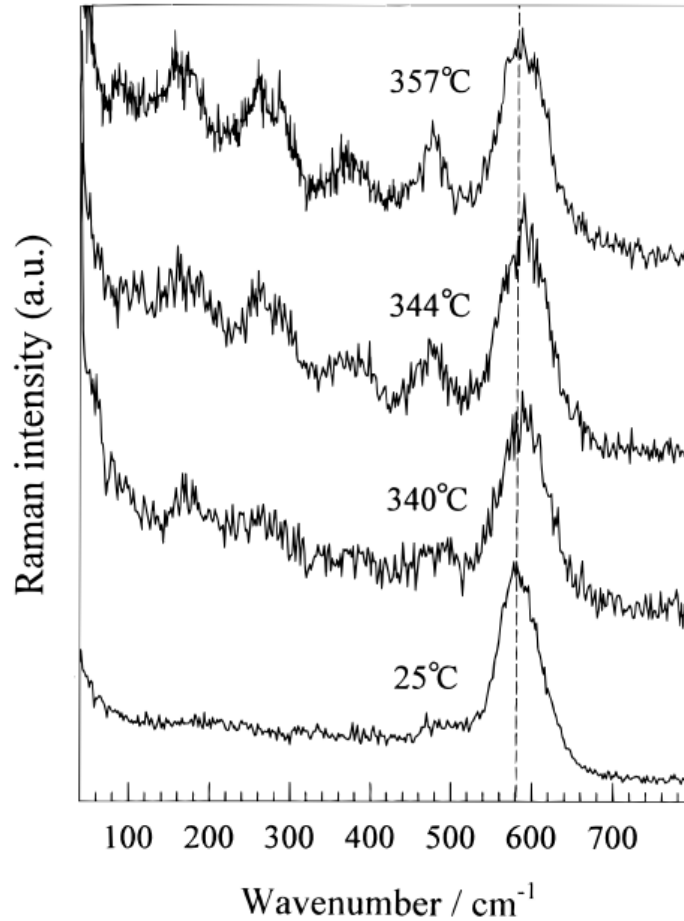


Fig. 1.8: Raman spectroscopy of ZBLAN sample at different temperature[42].

Due to long transmission window and low phonon energy, ZBLAN fiber can host different rare earth elements to with emission from UV to 3.9 μm [43,44]. Table 1.4 is summarized the possible emission lasing wavelength and pump wavelength for different rare earth doped ZBLAN fiber.

Table 1.4: Summary of laser wavelength and pump wavelength of rare earth doped ZBLAN fiber laser.

Rare earth	Laser wavelength (μm)	Pump wavelength (nm)	Rare earth	Laser wavelength (μm)	Pump wavelength (μm)
Er	1.55	980	Er	402	638
	1.7	791		470	638
	2.7	975		544	970
	3.45	640			
Tm	1.48	1064	Tm	248	1064
	1.94	792		455	645+1064
	2.3	790		481	1123
Ho	2	806	Ho	784	1120
	2.86	1100		808	1120
	3.22	532			
	3.9	885			
Dy	2.9	1100	Pr/Yb	491	840
				520	860
Pr	1.3	1064	Pr/Yb	605	840
Yb	1	911		615	860
Nd	1.05	514	Pr/Yb	635	850+823
	1.34	800		Ho	550
			Nd	381	590
				412	590

1.2.2 Blue emission of thulium doped ZBLAN

Thulium with the symbol Tm is a chemical element in lanthanides group. Its atomic number is 69 and it the second least abundant element among lanthanides. Like other lanthanides the most common oxidation state is +3. Tm metal is paramagnetic above 60 K, antiferromagnetic between 60 K to 22 K, and ferromagnetic below 22 K[45].

Tm³⁺ is an attractive and versatile rare earth ion which can act as an optical activator. It can emit light in UV, blue, and IR.

The partial energy diagram of Tm³⁺ is shown in Fig. 1.9. Tian *et al.* observed emission at 293, 351, 366 nm using 485 nm argon laser as the pump laser[46]. These emissions are corresponded to ¹I₆ → ³H₆, ¹I₆ → ³F₄, and ¹D₂ → ³H₆ respectively. They also observed enhanced UV at 293 nm and 351 nm when two pump wavelengths of 458 nm and 585 nm were used simultaneously. In order to excite the ion to ¹I₆, two upconversions by 458 nm wavelength are required. The reason that having simultaneously two pump wavelengths of 458 nm and 585 nm can have an enhanced emission, is because when ion is excited to ¹G₄ by 458 nm, then 585 nm can directly excite the ion from ¹G₄ to ¹I₆.

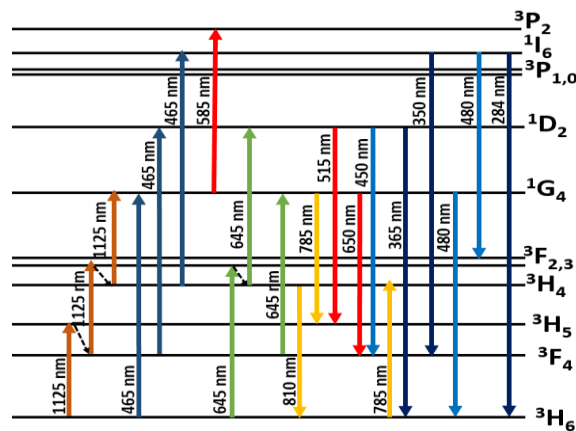


Fig. 1.9: Tm³⁺ partial energy diagram

Yang *et al.* studied the upconversion spectroscopy of Tm^{3+} ZBLAN in UV region[47]. They pumped a 2 mol% Tm^{3+} ZBLAN from 455 nm to 475 nm. They observed three emission at 292 nm, 350 nm, and 363 nm corresponding to $^1\text{I}_6 \rightarrow ^3\text{H}_6$, $^1\text{I}_6 \rightarrow ^3\text{F}_4$, and $^1\text{D}_2 \rightarrow ^3\text{H}_6$ transition respectively. Since they were able to tune their pump wavelength, they found the most efficient pump wavelength to be at 464 nm for both emission at 350 nm and 363 nm as shown in Fig. 1.10[47].

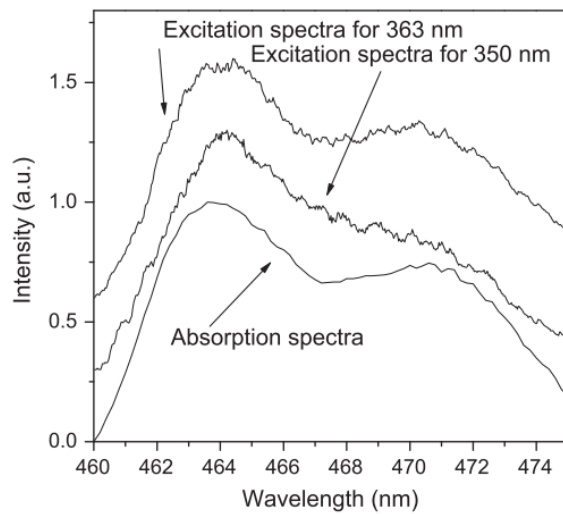


Fig. 1.10: Excitation spectra for 350 nm and 363 nm. The $^1\text{G}_4$ absorption spectra is also shown[47].

They also examined the fluorescence of 292 nm, 350 nm, and 363 nm as a function of pump power as shown in Fig. 1.11[47]. The slope of all three emissions as a function of pump power is around 2 which shows that the emission from $^1\text{I}_6$ and $^1\text{D}_2$ were induced by two photon process.

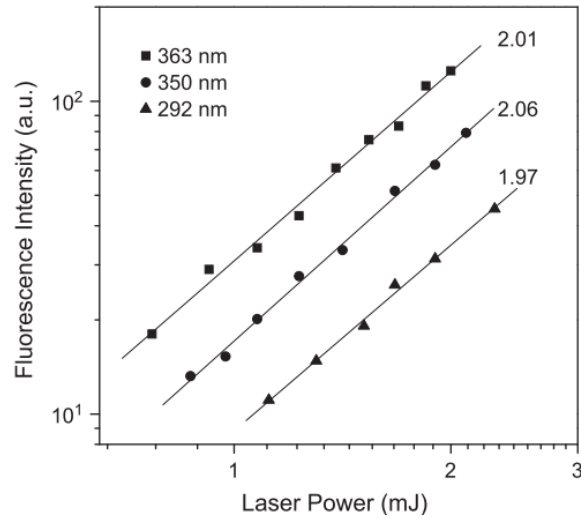


Fig. 1.11: The intensity dependence of 292, 350, 363 nm fluorescence[47].

There are two processes, excited state absorption (ESA) and energy transfer upconversion (ETU), that can generate upconversion. Different factors such as doping concentration, excitation wavelength, host materials, etc. can have influence on the efficiency of ESA and ETU. In order to distinguish between ESA and ETU the decay curve of the excited state can be studied. The decay curve of ESA has similar behavior as direct excitation decay curve, while if the ETU is involved, a short rise time can be seen in the decay curve followed by decaying. The decay lifetime of ETU is usually longer than direct excitation. Yang *et al.* found that the excitation of 1I_6 is due to ESA upconversion, while the excitation of 1D_2 can be defined by ETU upconversion[47]. In general, UV emission around 360-350 nm can be obtained by two photon process or three photon process. The ion can be excited to 1G_4 from ground state by 465 nm pump wavelength then it can drop to 3F_4 and then get excited to 1D_2 which can emit 365 nm in UV region. Or by pumping the glass by pump wavelength of 645 nm the ion can get excited to $^3F_{2,3}$ then it goes under a nonradiated decay to 3H_4 , and then it absorbs another 645 nm photon to go to 1D_2 . With three photon absorption the

ground state can be excited to 1I_6 which can emit deep UV around 290 nm. It also can emit 350 nm to 3F_4 , or 450 nm to $^3F_{2,3}$.

In 2008 El-Agmy demonstrated an upconversion laser at 284 nm using Tm^{3+} ZBLAN fiber[44]. The highest laser output power was 42 μW at 284 nm using Nd:YAG laser operating at 1064 nm. The slope efficiency was about 9%. In this work about 9 m 1 mol% double clad Tm^{3+} ZBLAN fiber was used. The output coupler had 96% reflection at the lasing wavelength. The ground state was excited to 3H_5 , then with nonradiative decay it drops to 3F_4 . Then with excited state absorption it goes to the energy level of 3F_2 and as the consequence of nonradiated decay it decays to 3H_4 . With absorbing another 1064 nm pump photon it gets excited to 1G_4 . Although the author believed the 1G_4 to 1I_6 is due to the cross relaxation, it is clearly due to the cooperative up conversion as shown in Fig. 1.12. The red arrows are the cooperative up conversion.

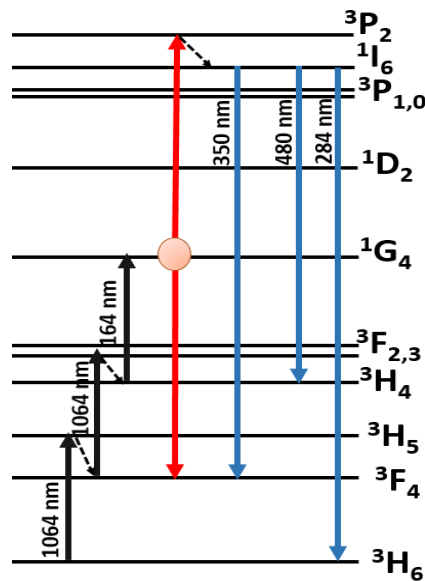


Fig. 1.12: Partial energy diagram of Tm^{3+} showing the cooperative up conversion (red lines).

In order to measure the ground state absorption cross section, Cary 5000 was used to measure the transmission of the Tm^{3+} ZBLAN glass. The absorption coefficient can be calculated from transmission, length of the glass, and refractive index (Which is not very significant here). By knowing the absorption coefficient, length of the glass, and ion concentration ground state absorption cross section can be found. Fig. 1.13 shows the ground state absorption cross section of Tm^{3+} ZBLAN glass. The absorption around 350 nm is corresponded to $^1\text{D}_2$, and the one around 480 belongs to $^1\text{G}_4$ energy level. 650 nm light can excite the ground state to $^3\text{F}_2$ and $^3\text{F}_3$ states. The peak absorption wavelength for $^3\text{H}_4$ was measured to be at 791 nm, and for $^3\text{H}_5$ at 1210 nm.

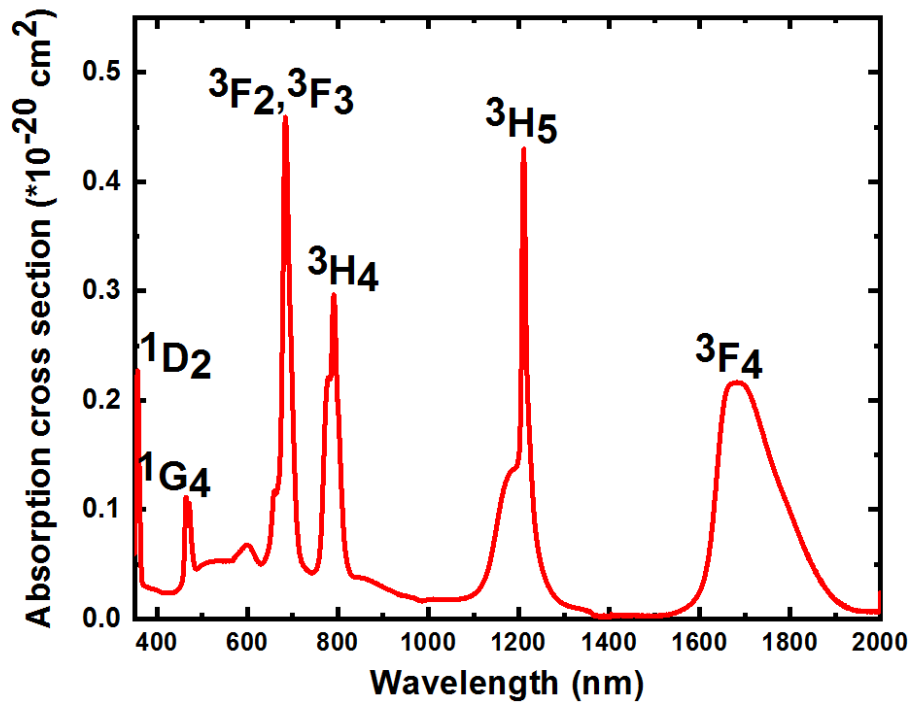


Fig. 1.13: Absorption cross section of Tm^{3+} ZBLAN glass.

The emission spectrum of Tm^{3+} ZBLAN glass can be measured by the setup shown in Fig. 1.14. To prepare the glass sample, three sides of the glass sample were polished to make sure the light scattering is minimized. Then the glass was mounted and pumped by a laser. The beam should

aim the sample close to the edge of the sample. The emission light from Tm^{3+} ZBLAN glass was collected by a lens then the collimated light traveled through a chopper which modulate the light and then the second lens focused the light into the monochromator. The detector can detect the light and send a signal to the lock in amplifier which was synchronized by the same frequency as chopper was working. Chopper driver must be connected to the lock in amplifier to make sure that just modulated light is going to be detected. The spectrum is displayed on the monitor of the computer.

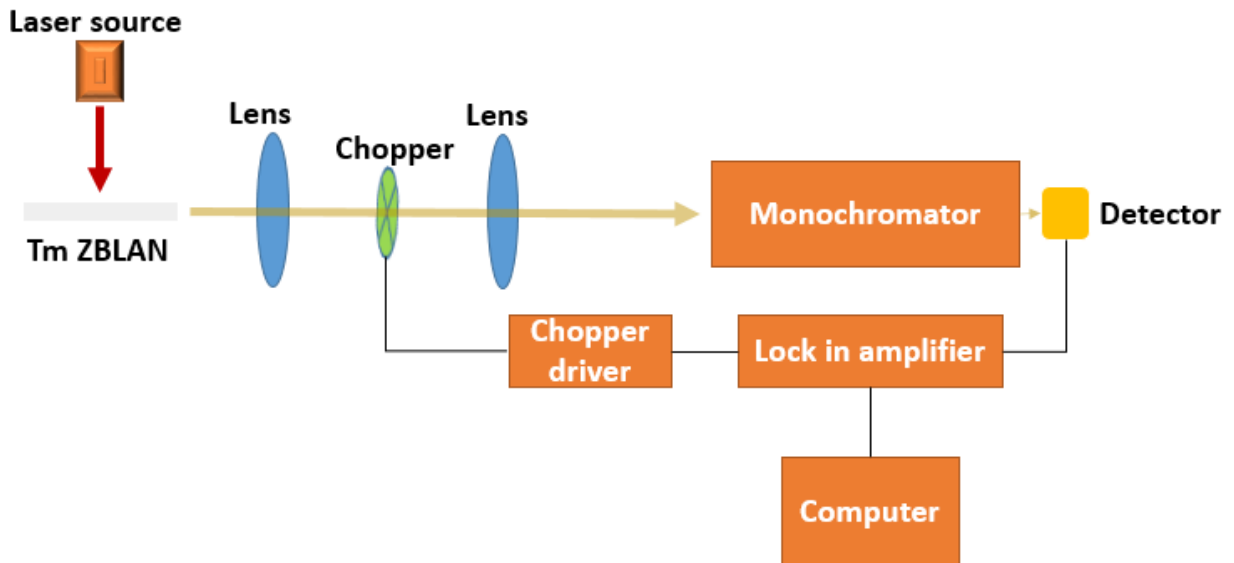


Fig. 1.14: Bulk Tm^{3+} ZBLAN glass emission setup.

The fluorescence of Tm^{3+} ZBLAN glass from $^1\text{G}_4$ energy level was measured as shown in Fig. 1.15. The emissions at 480 nm and 650 nm corresponds to the transitions from state $^1\text{G}_4$ to $^3\text{H}_6$ and $^3\text{F}_4$, respectively. The emission peak near 800 nm, however, is the combination of two

transitions: ${}^1G_4 \rightarrow {}^3H_5$ and ${}^3H_4 \rightarrow {}^3H_6$. Both transitions influence the operation of the 480 nm amplifier.

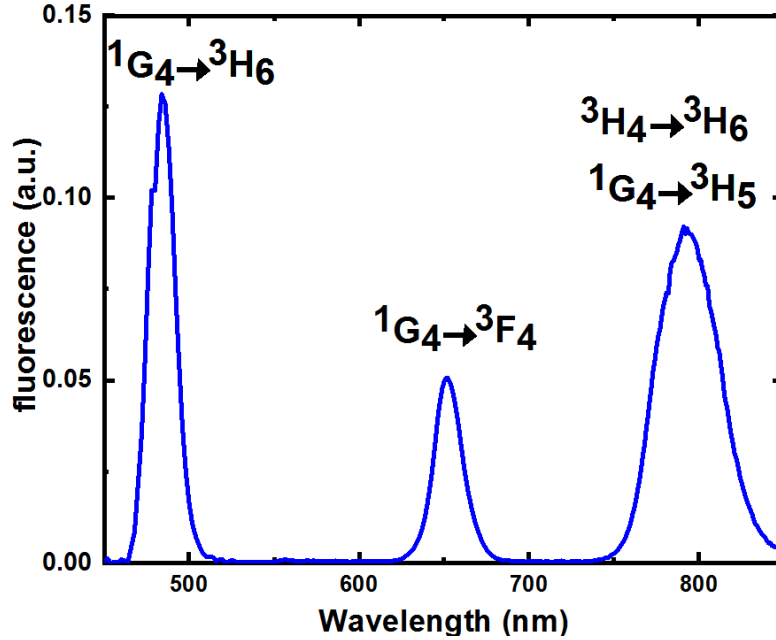


Fig. 1.15: Measured fluorescence of Tm^{3+} ZBLAN glass from 1G_4 energy level.

The branching ratio of different optical transitions of Tm^{3+} ZBLAN glass was calculated in the frame work of Judd–Ofelt theory by Doualan *et al.*[48]. Branching ratio is the probability of a radiative transition from a fixed excited state. As it can be seen the branching ratio of three transitions ${}^1G_4 \rightarrow {}^3H_6$, ${}^1G_4 \rightarrow {}^3F_4$, and ${}^1G_4 \rightarrow {}^3H_5$ are 0.378, 0.077, and 0.384, respectively.

The radiative lifetime of different excited state of Tm^{3+} ZBLAN with different thulium concentrations have been measured by different groups[48,49]. The life time of 1I_6 state of 2 mol% Tm^{3+} ZBLAN was measured to be 84.2 μs , 1D_2 life time was obtained to be 140 μs , and for 1G_4 295 μs [47].

Table 1.5: The branching ratio of different optical transitions of Tm^{3+} ZBLAN glass.

Optical transition	λ (μm)	β
${}^3\text{F}_4 \rightarrow {}^3\text{H}_6$	1.724	1
${}^3\text{H}_4 \rightarrow {}^3\text{H}_6$	0.787	0.88
${}^3\text{H}_4 \rightarrow {}^3\text{F}_4$	1.45	0.095
${}^3\text{H}_4 \rightarrow {}^3\text{H}_5$	2.3	0.025
${}^1\text{G}_4 \rightarrow {}^3\text{H}_6$	0.463	0.378
${}^1\text{G}_4 \rightarrow {}^3\text{F}_4$	0.633	0.077
${}^1\text{G}_4 \rightarrow {}^3\text{H}_5$	0.756	0.384
${}^1\text{G}_4 \rightarrow {}^3\text{H}_4$	1.125	0.116
${}^1\text{G}_4 \rightarrow {}^3\text{F}_{2,3}$	1.4	0.044

Another group found the life time of ${}^1\text{I}_6$, ${}^1\text{D}_2$, ${}^1\text{G}_4$ at 2.5 mol% to be 48 μs , 23 μs , and 54 μs respectively[50]. They also found as concentration is decreased the lifetime significantly increases. For instance, for 0.15 mol% the life time of ${}^1\text{I}_6$, ${}^1\text{D}_2$, ${}^1\text{G}_4$ were found to be 80 μs , 55 μs , and 630 μs respectively. This indicates that energy transfer process is very important in Tm^{3+} ZBLAN. The lifetime of ${}^3\text{F}_4$, and ${}^3\text{H}_4$ levels play a crucial role when the ${}^1\text{G}_4$ level is going to be populated by three photon absorption. Doualan *et al.* calculated the lifetime of ${}^3\text{F}_4$, and ${}^3\text{H}_4$ to be 8.49 ms, and 1.396 ms respectively[48]. They used 3 at.% Tm^{3+} ZBLAN for this experiment. The lifetime of ${}^1\text{G}_4$ was also predicated to be 0.764 ms. The measured lifetime of ${}^3\text{F}_4$ found to be 7.93 ms in a good agreement with the calculated one. But for ${}^3\text{H}_4$ the measured lifetime (45 μs) was much below the predicted lifetime. The decay curve was not able to be fitted by a single

exponential decay curve and multiple fitting terms needed to be used. The result suggests that the presence of cross relaxation for 3H_4 is strong.

Walsh *et al.* used Judd–Ofelt theory to calculate the line strengths, radiative transition probabilities, and branching ratio of different states in Tm^{3+} ZBLAN[49]. Then they deduced the lifetime of 1I_6 , 1D_2 , 1G_4 , 3F_2 , 3H_4 , 3H_5 , and 3F_4 from the summation of radiative transition probabilities to be 0.11, 0.073, 0.908, 1.234, 1.519, 6.863, 11.223 ms respectively. Fig. 1.16 shows the lifetime of each state of Tm^{3+} ZBLAN and Tm^{3+} silica versus the energy level of the state respect to the ground state. In most cases as the energy level decreases the lifetime increases. But the lifetime of 1I_6 is longer than 1D_2 . As it can be seen the lifetime of thulium ion in ZBLAN glass is significantly longer than that of silica glass. For example, 1G_4 lifetime in ZBLAN glass is 0.908 ms and in silica is 0.428 ms. The lifetime of 3F_4 in ZBLAN glass is about four times longer than in silica.

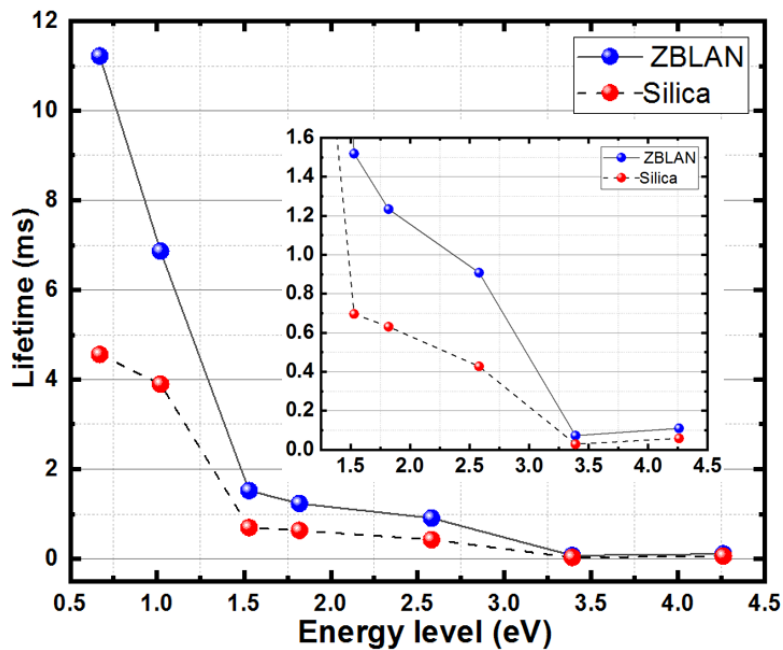


Fig. 1.16: Lifetimes of different states of Tm^{3+} in ZBLAN and silica glasses.

Comparing the lifetime of energy levels of thulium doped silica and ZBLAN clearly shows that ZBLAN is much better glass matrix for upconversion process. Table 1.6 shows the difference in lifetimes of 3F_4 , and 3H_4 manifolds for thulium doped silica and Tm^{3+} ZBLAN measured by Walsh *et al.*[49]. For example, for 3F_4 the lifetimes in ZBLAN is longer than silica with two orders of the magnitude.

Table 1.6: Measured lifetimes of 3F_4 , and 3H_4 manifolds for thulium doped silica and ZBLAN[49].

Material	Wt. %	Tm density ($*10^{20} \text{ cm}^{-3}$)	$^3F_4 \tau$ (ms)	$^3H_4 \tau$ (ms)
Tm: silica	1.44	4.12	0.42	0.02
Tm: ZBLAN	0.32	0.36	11.2	1.51
Tm: ZBLAN	2.88	3.23	13.7	0.33

The life time measured for 3F_4 with 0.32 wt.% Tm^{3+} ZBLAN is 11.2 ms which is in a good agreement with the one predicted by Judd–Ofelt theory as shown in Fig. 1.16. The reason that 2.88 wt.% Tm^{3+} ZBLAN has longer lifetime at 3F_4 compared to 0.32 wt.% Tm^{3+} ZBLAN, is due to radiative trapping. Having longer lifetime for $Tm \ ^3F_4$ and $Ho \ ^5I_7$ as the concentration increases which is known due to radiative trapping. The lifetime of $Tm \ ^3F_4$ in silica calculated by Judd–Ofelt theory was much longer the measured one. It can be due to nonradiative quenching. Nonradiative quenching can be affected by high phonon energy as it is for silica glass which is about 1100 cm^{-1} .

1.3 Single frequency blue laser fiber amplifier

The energy level diagram of Tm^{3+} related to blue emission is shown in Fig. 1.17. Blue laser emission at 480 nm band can be obtained by directly exciting the ground state $^3\text{H}_6$ to $^1\text{G}_4$ by 465 nm pumping.

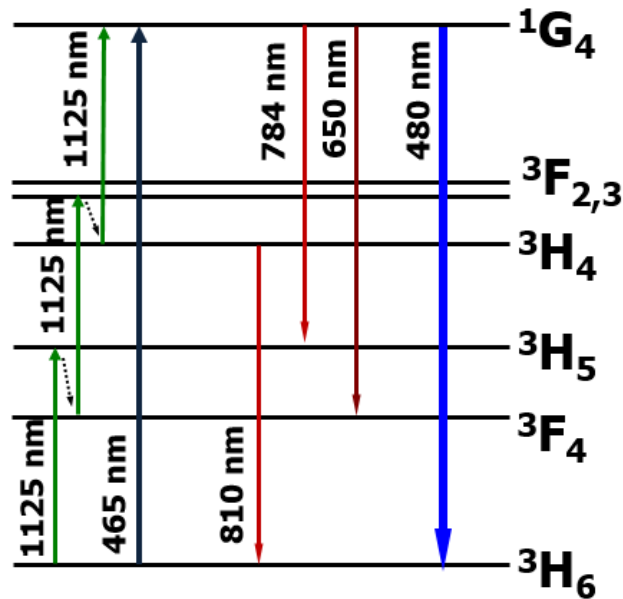


Fig. 1.17: Partial energy diagram of Tm^{3+} related to the blue light emission.

Since there is no available high power single-mode laser source at 465 nm, it is not an effective pump source. The power spectra of amplified stimulated emission of Tm^{3+} ZBLAN fiber pumped by 465 nm laser source is shown in Fig. 1.18. Different pump power was used to show the difference in the spectrum. The length of fiber was about 6.5 m and the thulium concentration was 0.1 mol%. As it is mentioned above the pump power wasn't high and also since the setup was a free space setup, there was some loss during the coupling of the pump light into the fiber. As it can be seen the emission around 650 nm is high compared to 480 nm and 784 nm. This is

due to the fact that 784 emission gets absorbed by 3H_4 level as shown in Fig. 1.13. The ground state absorption for 784 nm is significantly higher than 650 nm emission. Emission with 40 mW pump power is significantly stronger than the emission with 21 mW pump power. However, that much difference was not observed as the pump power increased to 61 mW and then to 72 mW.

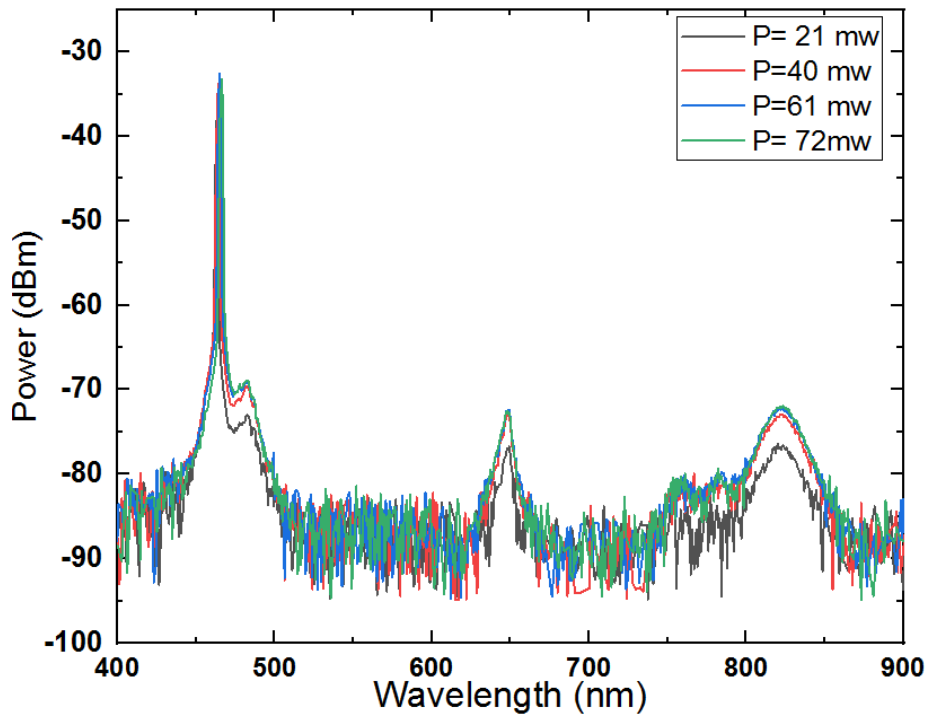


Fig. 1.18: Power spectra of amplified stimulated emission of Tm^{3+} ZBLAN fiber pumped by 465 nm laser diode at different pump power.

Since the 465 nm laser diode output was limited to about hundred mW, another option which is upconversion pumping near IR. Due to the long lifetimes of some metastable energy levels between 3H_6 to 1G_4 , ions can be excited to the upper laser level 1G_4 by absorbing three pump photons. Different wavelengths of upconversion pumping from 1064 nm to 1210 nm have been reported, capable of exciting ground state 3H_6 to 1G_4 [17]. Although the peak absorption cross

section from ground level to 3H_5 ($^3H_6 \rightarrow ^3H_5$) is around 1200 nm, 1125 nm was used to populate the 1G_4 level because the three absorption transitions $^3H_6 \rightarrow ^3H_5$, $^3F_4 \rightarrow ^3F_3$, and $^3H_4 \rightarrow ^1G_4$ have a better effective absorption at this wavelength [51].

In order to build a robust high power fiber laser at 1125 nm, ytterbium (Yb) doped silica fiber was used to build the laser. The absorption and emission spectrum of Yb: Silica is shown in Fig. 1.19 [52]. The peak absorption in Yb: Silica is around 980 nm but the emission at 1125 nm is not strong. Although the emission at 1125 nm is not strong, there is no absorption at this wavelength either.

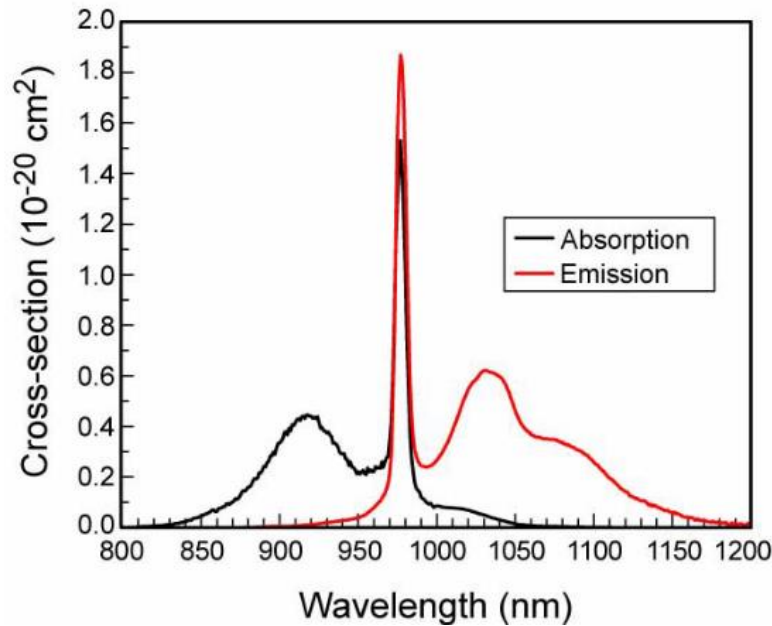


Fig. 1.19: Absorption and emission cross section of Yb: Silica[52].

The partial energy diagram of Yb is shown in Fig. 1.20. With in band pumping between $^3F_{7/2}$ to $^3F_{5/2}$ the excited state can emit at 1125 nm to ground state. The laser dynamic of Yb at this wavelength operates like a two level system.

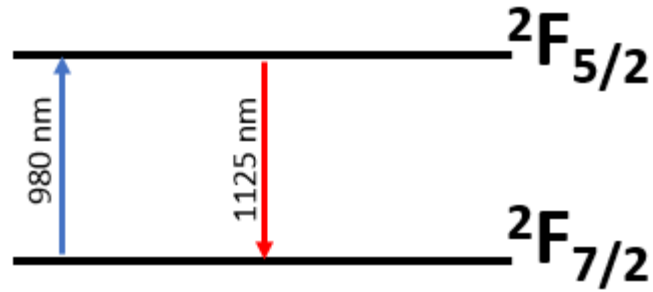


Fig. 1.20: Partial energy diagram of Yb related to lasing at 1125 nm.

The schematic setup of 1125 nm fiber laser is shown in Fig. 1.21. Two pump diodes operating at 980 nm were used as the pump source then a combiner was used to combine the pump lights and pump the gain fiber. High reflective fiber grating (HR FBG) with high reflection at 1125 nm and partially reflective fiber grating (PR FBG) were used to build the cavity. The gain fiber and common port of the combiner were double clad while the signal port of the combiner was HI1060 fiber. Both FBGs were written on HI1060 fiber so, the residual pump must be dumped before HR FBG.

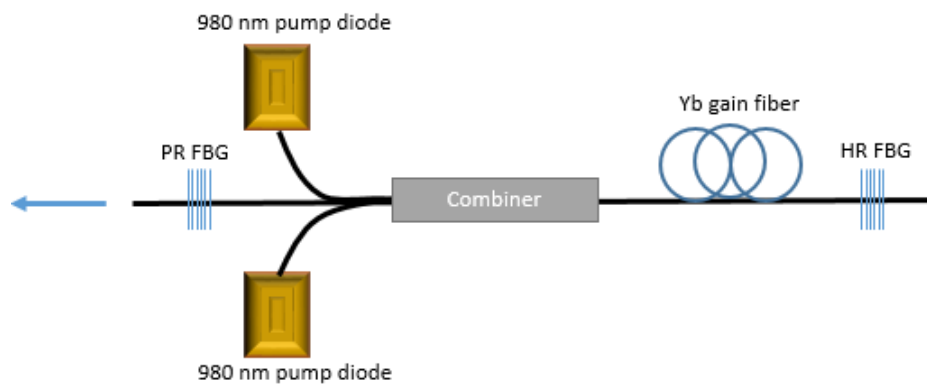


Fig. 1.21: The schematic setup of all fiber laser operating at 1125 nm.

The laser power versus the two 980 diodes pump power was measured by a Newport power detector. The output power with respect to the lunched pump is shown in Fig. 1.22. The maximum laser power of 9.4 W was obtained with 33 pump power. The slope efficiency was about 28% and the threshold pump power was about 0.9 W.

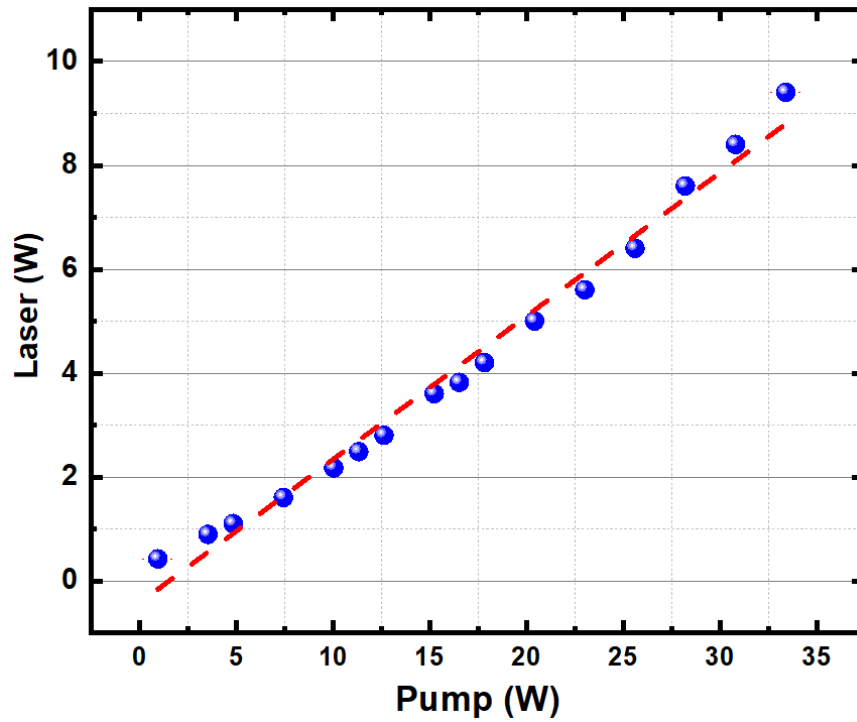


Fig. 1.22: Output laser with respect to lunched pump power.

The optical spectrum of the all fiber laser operating at 1125 nm was measured by an optical spectrum analyzer as shown in Fig. 1.23. The laser was very stable.

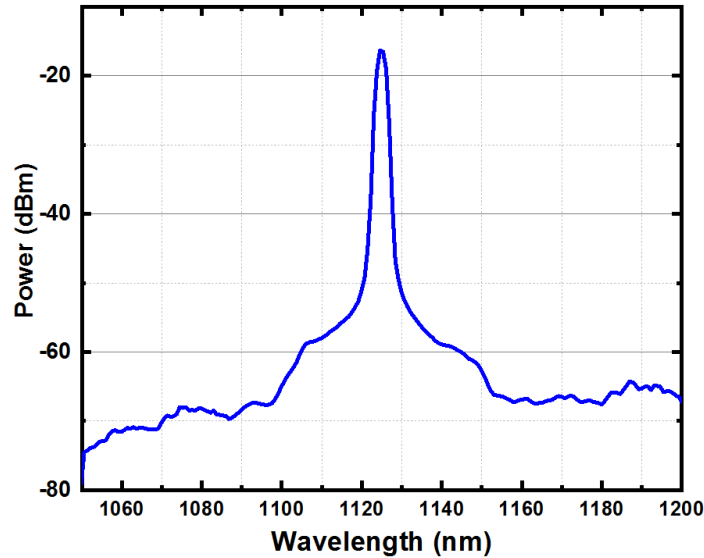


Fig. 1.23: The optical spectrum of fiber laser operating at 1125 nm.

The seed signal in this experiment was a single frequency laser diode fiber coupled which was provided by Toptica. A GaN diode laser was used with broad linewidth and then a Littrow external cavity was utilized to select a single frequency laser output with narrow linewidth. The schematic setup of external cavity laser diode with Littrow configuration fiber coupled is shown in Fig. 1.24. The GaN diode is the laser diode which emits the blue light then an aspheric lens is used to collimate the light. The collimated light hits the blazed grating in which the first order diffraction coupled back directly to the diode and zeroth order is the laser output. A mirror was used to redirect the collimated beam which passes through an isolator. An Isolator was used to prevent light coming back from fiber to the cavity and causes fluctuation. Finally, the blue light was coupled to a PM460 HP fiber.

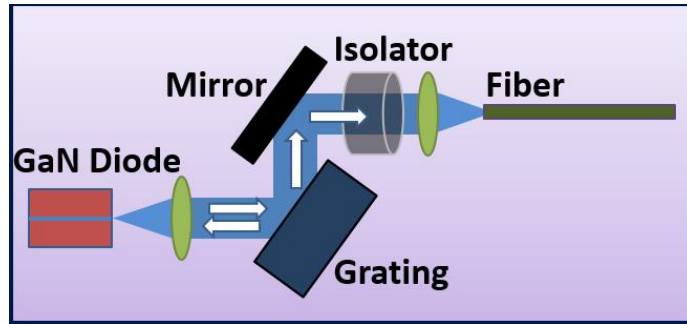


Fig. 1.24: The schematic setup of external cavity laser diode Littrow configuration fiber coupled.

The wavelength of the output light depends on the angle of incident beam with respect to the grating. By changing the angle, the output wavelength can be tuned. In order to meet Littrow configuration requirement for lasing at a single frequency the angle of incident beam with respect to the grating and the angle of first order diffraction which directs back to the diode must be same as the blaze angle.

Fig. 1.25 shows the output spectrum of GaN laser diode without Littrow configuration (blue) and with Littrow configuration (red). As it can be seen from the diagram the peak of the spectrum is shifted in Littrow configuration.

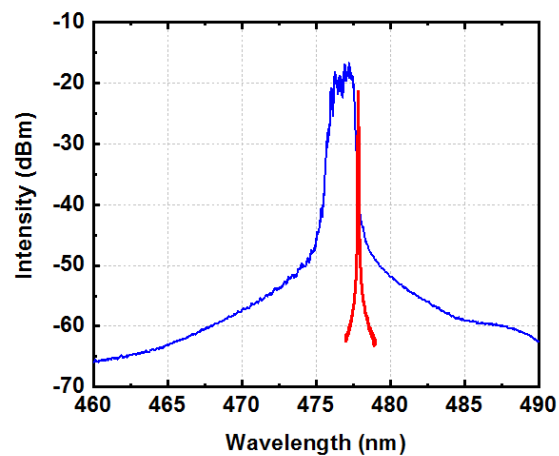


Fig. 1.25: The output spectrum of GaN laser diode (blue), and external cavity Littrow configuration (red).

The optical spectrum of external cavity Littrow configuration which was built by Toptica at different applied currents is shown in Fig. 1.26. The output increases by increasing current from 90 mA to 93.1 mA, but after that it significantly decreases as it can be seen at $I= 94.1$ mA. This decrease is mainly due to the thermal issue of semiconductor laser. The wavelength can be tuned finely with changing the applied current.

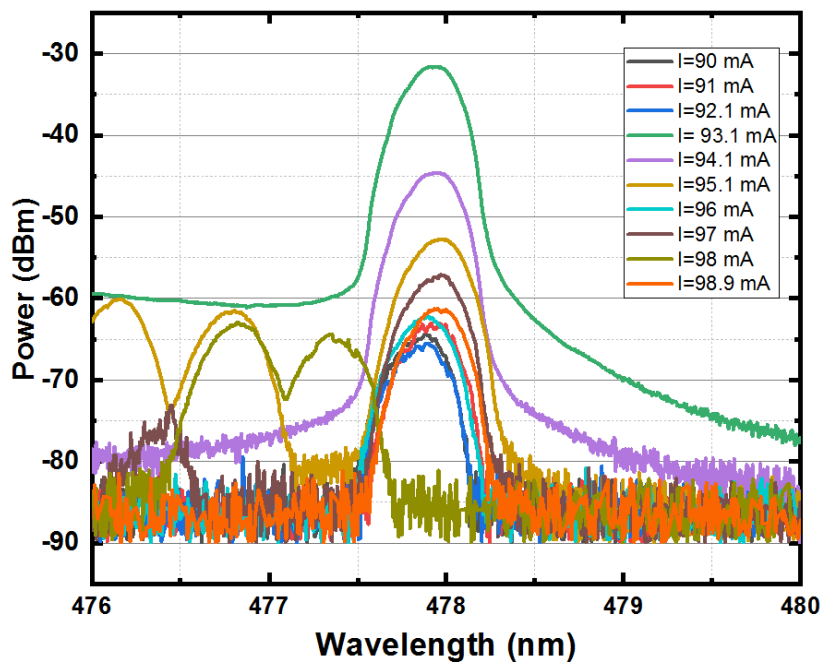


Fig. 1.26: Optical spectra of the Toptica laser at different applied currents.

In this experiment, we built a single frequency blue laser fiber amplifier pumped by 1125 nm Yb: Silica. There are three radiative transitions from energy level 1G_4 to lower energy levels with strong emission at 480nm, 650nm and 800nm as shown in Fig. 1.15. The branching ratios of the three transitions are 0.378, 0.077, and 0.384, respectively. The branching ratios of the 480 nm emission and the 800 nm emission are very close to each other.

It should be noted that $^1G_4 \rightarrow ^3H_5$ and $^3H_4 \rightarrow ^3H_6$ transitions can have influence on the laser amplifier operating at 480 nm. With increasing pump power, the population of the ground state decreases which can lead to higher population inversion for $^1G_4 \rightarrow ^3H_6$ (480 nm band), and $^3H_4 \rightarrow ^3H_6$ (800 nm band). But since, populating 3H_4 is easier than populating 1G_4 due to the number of photon absorption, then $^3H_4 \rightarrow ^3H_6$ emission can have a negative impact on the laser performance at 480 nm. It should be also mentioned that, due to emptiness of 3H_5 energy level as shown in the inset of Fig. 1.9 **Error! Reference source not found.**, population inversion for the 785 nm transition is achieved much easier compare to 480 nm emission which again can negatively affect the laser operation at 480 nm.

In order to obtain single transverse mode output, a Tm^{3+} -doped ZBLAN fiber with a core diameter of 4 μm and a numerical aperture of 0.07, corresponding to V-number and cutoff wavelength of 2.095 and 365 nm respectively, was designed and fabricated. The microscope image of the end facet of the fiber is shown in Fig. 1.27 (a).

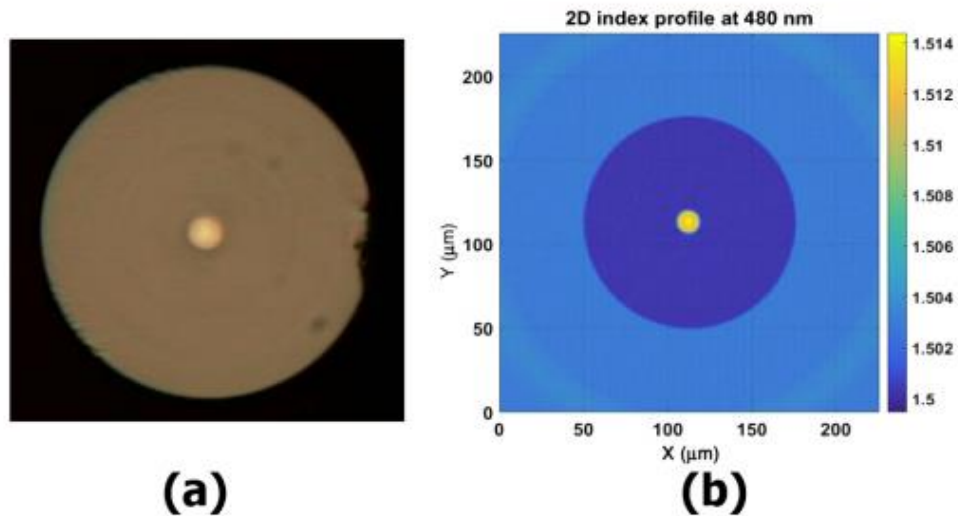


Fig. 1.27: (a) Microscope image of an end face and (b) 2D refractive index profile of the single-mode Tm^{3+} -doped ZBLAN fiber.

Fig. 1.27 (b) shows the 2D diagram of refractive index profile of the fiber measured with an interferometric fiber analyzer (Interfiber Analysis, IFA-100). This fiber has a 12- μm inner cladding doped with 100 ppm neodymium (Nd^{3+}) which intentionally suppresses 800 nm emission due to Nd^{3+} absorption in this wavelength region. The outer cladding of this fiber is 125 μm compatible with standard silica fiber enabling easy fusion splicing and the construction of all-fiber amplifiers. The fiber core is doped with 1000 ppm Tm^{3+} and the absorption of this fiber of 1125 nm light launched into the fiber core was measured by a cutback experiment to be about 1.56 dB/m as shown in Fig. 1.28.

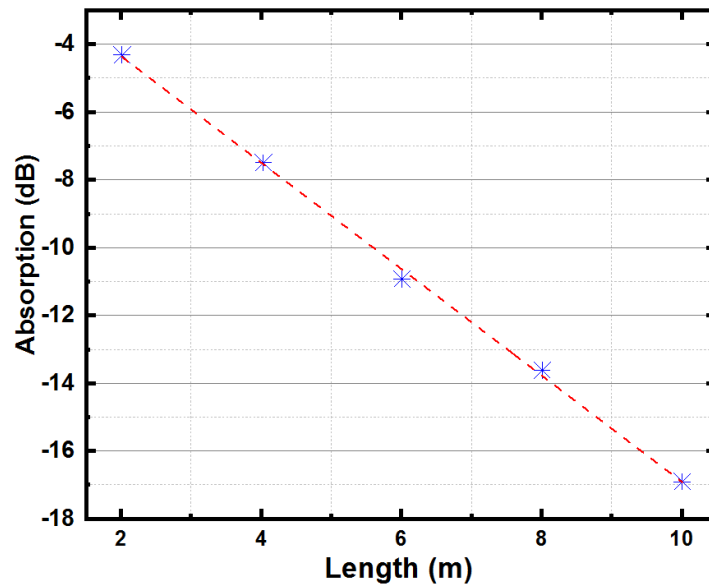


Fig. 1.28: Cutback experiment, using 10 m Tm^{3+} ZBLAN fiber.

The schematic of the all-fiber blue laser amplifier is shown in Fig. 1.29. A single frequency external cavity GaN diode laser at 478 nm coupled to a polarization maintaining (PM) single-mode silica fiber (PM 460HP) was used as the seed laser. An ytterbium (Yb^{3+}) doped silica fiber

laser operating at 1125 nm was used as the pump source. A PM wavelength division multiplexor (WDM) made of PM 460HP (signal port) and PM980 fiber (pump and common port) was used to combine the seed signal laser and the pump laser together. The signal coupling efficiency is about 80% and the pump coupling efficiency is about 92%. The polarization extinction ratio (PER) of the signal laser changes from an initial value of 25 dB to 18 dB after the PM WDM indicating that most signal laser is coupled to the fundamental mode of the PM980 fiber although this fiber has a cutoff wavelength of 705 nm and is multimode for the blue light.

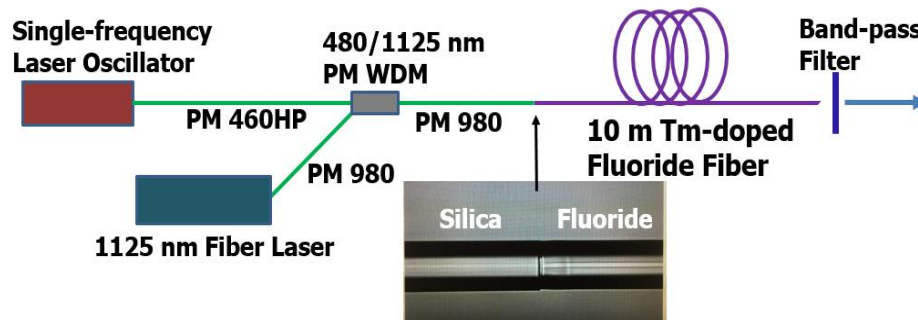


Fig. 1.29: Experimental setup of the all-fiber blue laser amplifier. Inset: the picture of the splice joint between the silica fiber and the fluoride fiber.

It should be noted that the common port fiber of the PM-WDM was fixed on the optical table to reduce power fluctuations and decrease of the fundamental mode caused by small bending and other environmental effects. 10-m of Tm^{3+} -ZBLAN fiber was spliced to the common port PM980 fiber. The image of the splice joint between the PM980 silica fiber and the Tm^{3+} -doped ZBLAN fiber is shown in the inset of Fig. 1.29. The typical loss of the splice between a ZBLAN fiber and a silica fiber is less than 0.3 dB. 10-m ZBLAN fiber was chosen based on the cutback experiment because it produced the maximum output power. The output end of the ZBLAN fiber

was angle cleaved to reduce backward reflections. A band-pass filter at 480 nm was used to remove the residual pump at 1125 nm.

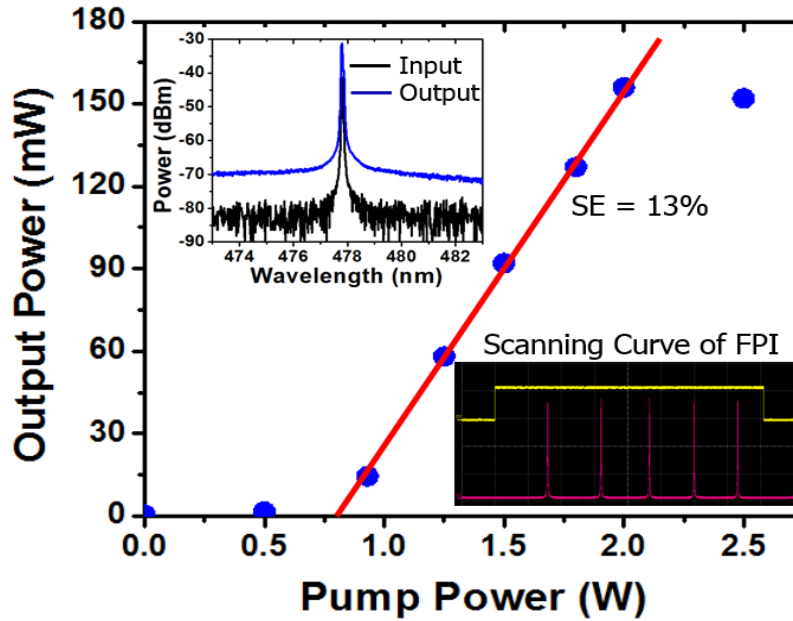


Fig. 1.30: Measured output power of the 478 nm fiber amplifier as a function of the launched pump power. Upper left inset: Optical spectra of the input and output of the fiber amplifier. Lower right inset: Single-frequency operation of the GaN diode laser confirmed with a scanning Fabry-Perot Interferometer.

In the experiment, single-frequency operation of the GaN diode laser was confirmed by a scanning Fabry-Perot interferometer (FPI) as shown in the lower right inset of Fig. 1.30. The blue signal laser power after the PM-WDM was approximately 15 mW. The optical spectra of the fiber amplifier with and without pump were measured with an optical spectrum analyzer (Ando, AQ6351A) and is shown in the upper left inset of Fig. 1.30. The output power of the fiber amplifier as a function of the pump power was measured by a power meter (Thorlabs, PM100D) and is shown in Fig. 1.30. The pump threshold of the fiber amplifier is about 750 mW. The blue laser output increases with pump power and saturates when the pump power exceeds 2 W. A maximum output power of 155 mW, corresponding to a net gain of 10 dB was obtained.

The slope efficiency of this fiber amplifier is about 13%, which is smaller than those of previous experiments because of smaller overlaps of pump and signal lasers and the lower fiber NA when compared to multimode fibers used in previous reports. The lower efficiency is the result of the tradeoffs employed to achieve single transverse mode output beam using a low core NA fiber.

The beam quality of the fiber amplifier output was measured with a beam profiler (DataRay Inc., Beam Map2). The 2D beam profile is shown in Fig. 1.31(a). The cross-section of the beam profile and its Gaussian fit are shown in Fig. 1.31(b). There are two small side peaks in the measurement due to excited cladding modes. It should be noted that the beam profile was not stable and the measured beam quality was about $M^2 \sim 1.5$ at low pump powers because of interference between the cladding modes and the fundamental core mode supported by the long coherence length of the single-frequency signal laser with a typical linewidth < 1 MHz. The beam quality improved with increasing pump power. A beam quality M^2 of 1.06 was measured at the maximum output power. The PER of the output laser was measured to be approximately 11 dB even though the Tm³⁺-ZBLAN fiber is not designed to maintain the polarization of the signal laser.

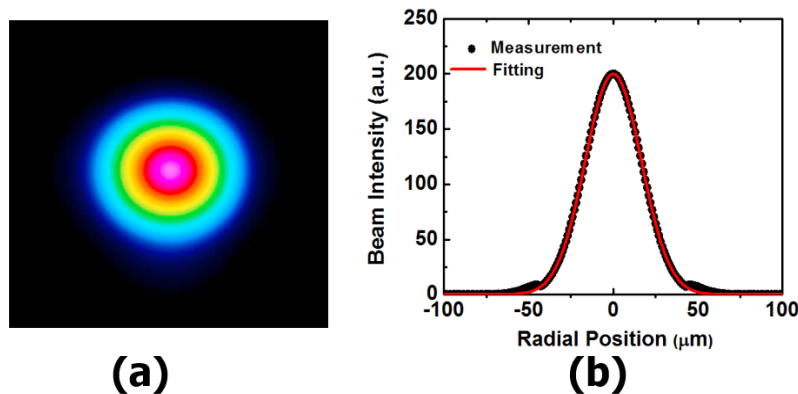


Fig. 1.31: (a) 2D profile of the fiber amplifier output beam; (b) Cross-section of the output beam profile and its Gaussian fit.

As mentioned above, the 12- μm inner cladding of the Tm^{3+} -doped ZBLAN fiber was doped with 100 ppm Nd^{3+} in order to suppress the competitive 800 nm laser. Nd^{3+} has significant absorption near 800 nm due to transitions from $^4\text{I}_{9/2}$ to ($^2\text{H}_{9/2}$, $^4\text{F}_{5/2}$) as shown by the black curve in Fig. 1.32. Absorption of 800 nm emission from Tm^{3+} occurs because of partial mode overlap between the core mode field and the Nd^{3+} doped cladding. However, the output power of this Tm^{3+} -ZBLAN fiber amplifier still saturated at a pump power of 2 W and decreased with further increasing pump power due to the onset of the laser at 783 nm as shown in Fig. 1.32. When the pump power is 2 W, there is ASE at 800 nm and Tm^{3+} long wavelength lasing is effectively suppressed by the Nd^{3+} absorption in the inner cladding. When the pump power is 2.5 W, the 783 nm laser starts and the 478 nm signal power decreases as shown by the blue curve.

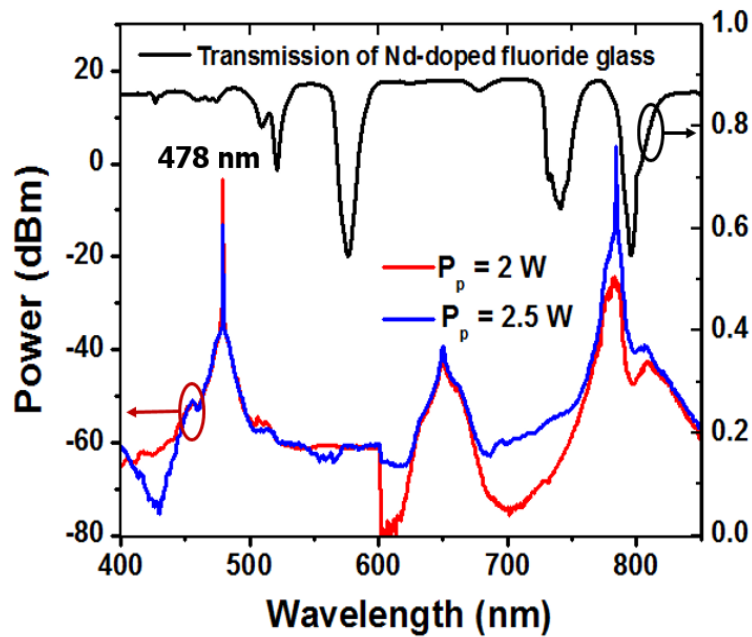


Fig. 1.32: Optical spectra of the fiber amplifier when the pump power is 2 W (red curve) and 2.5 W (blue curve), respectively. The black curve: Transmission of a 1-cm thick Tm^{3+} -doped ZBLAN glass.

Further suppressing the 783 nm laser may be obtained with an optimized Nd^{3+} doping level but we should notice that Nd^{3+} also has some absorption at 478 nm, which reduces the efficiency of the fiber amplifier correspondingly. Proper fiber design that can produce high loss at 783 nm while negligible loss at the wavelength of the blue laser could offer an attractive option of further suppress the competitive lasing.

Any bend in an optical fiber can cause a loss as shown in Fig. 1.33. The loss due to bending depends on the fiber parameters such as refractive index difference of core-cladding, the core radius, and the wavelength of operation. For a single mode fiber, the bending loss is highly dependent on the ratio of mode field diameter at the operating wavelength and core size of the fiber. In order to reduce the effect of bending loss, a fiber with large numerical aperture (NA) can be designed.

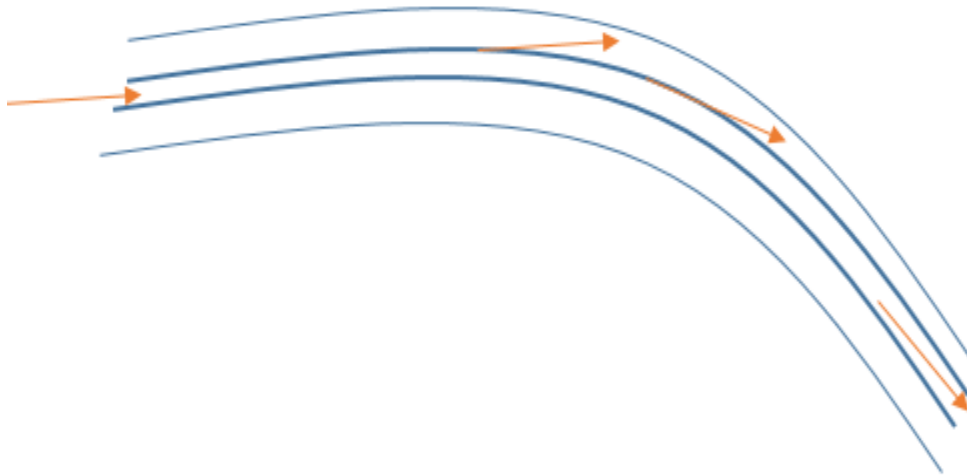


Fig. 1.33: Loss due to fiber bending.

The bending loss increases in longer wavelengths. Consequently, one method to remove long wavelength emission in a fiber is to apply some bending loss. Fig. 1.34 shows the loss of bended fiber spectrum at different bending diameter. A white light source was used to test the

bending loss spectrum and the transmitted light was detected by an optical spectrum analyzer. In order to calculate the loss, the light transmission without bending was measured as the input power for each wavelength. For bending diameter of 75 mm the edge of loss is around 850 nm. If the fiber is bended for 50 mm diameter then the edge of loss starts at about 800 nm and for 25 mm is about 750 nm. This result shows that bending can be an option to remove the longer wavelength emission.

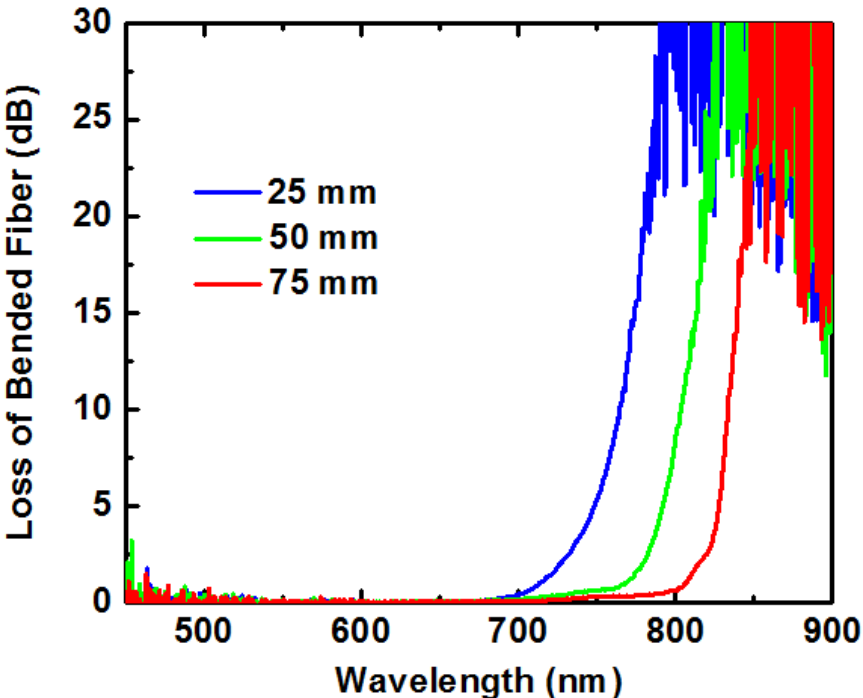


Fig. 1.34: Loss of bended fiber for different bending diameter as a function of wavelength.

Fig. 1.35 (a) shows the experimental setup to study the effect of coiling on the output power of blue fiber laser amplifier. In this setup still single frequency blue laser diode was used as the seed laser and then it was pumped by 1125 nm fiber laser. The single frequency blue laser diode was

coupled to a PM460 HP. Then the PM460 HP fiber was spliced to the signal port of a WDM which was the same fiber. The signal fiber was PM460 HP and common port was PM780 HP, and the port that was spliced to 1125 nm fiber laser was also PM780 HP. Tm^{3+} ZBLAN was used as the gain fiber and then it was spliced to a PM460 HP which is single mode at 480 nm. This experiment was done with no input pump and no coiling, pumping at 0.3 W with coiling and without coiling.

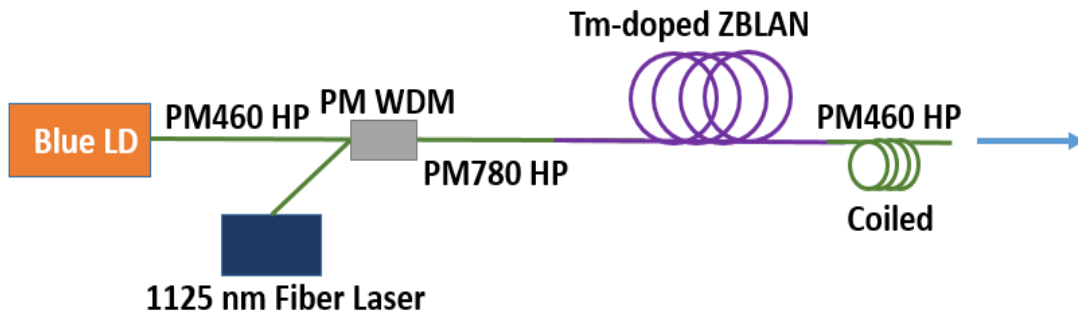


Fig. 1.35: (a) Experimental setup to study the effect of coiling;

The optical spectrum of signal output power is shown in Fig. 1.36. When there is no input pump power and just signal is in the gain fiber, the output power is about -31 dBm. It should be noted that the signal can be absorbed by gain fiber Tm^{3+} ZBLAN and excite the ions to $^1\text{G}_4$ energy level. The emission around 650 nm and 800 nm is due to the absorption of the signal and then remission. Two transitions of $^1\text{G}_4 \rightarrow ^3\text{H}_5$ and $^3\text{H}_4 \rightarrow ^3\text{H}_6$ have a broad bandwidth of 100 nm from 760 nm to 860 nm. But the tail of the emission goes beyond 900 nm. When the gain fiber is pumped with 0.3 W the output signal increases to about -26 dBm but 650 nm and 800 nm emission band are still strong. After coiling the PM460 HP fiber the emission beyond signal

emission is completely removed, but the output signal power also significantly dropped. The signal output after coiling is about -54 dBm. It should be noted that after pumping the broad peak around 780 nm which was observed in no pumping is removed. The reason behind that is due to fact that the signal power acts like an in band pumping and it excites the ions to 1G_4 and then the emission from $^1G_4 \rightarrow ^3H_5$ which is around 785 nm is stronger. But this emission can be trapped by the ground state absorption and excites Tm^{3+} to 3H_4 which can emit light around 810 nm.

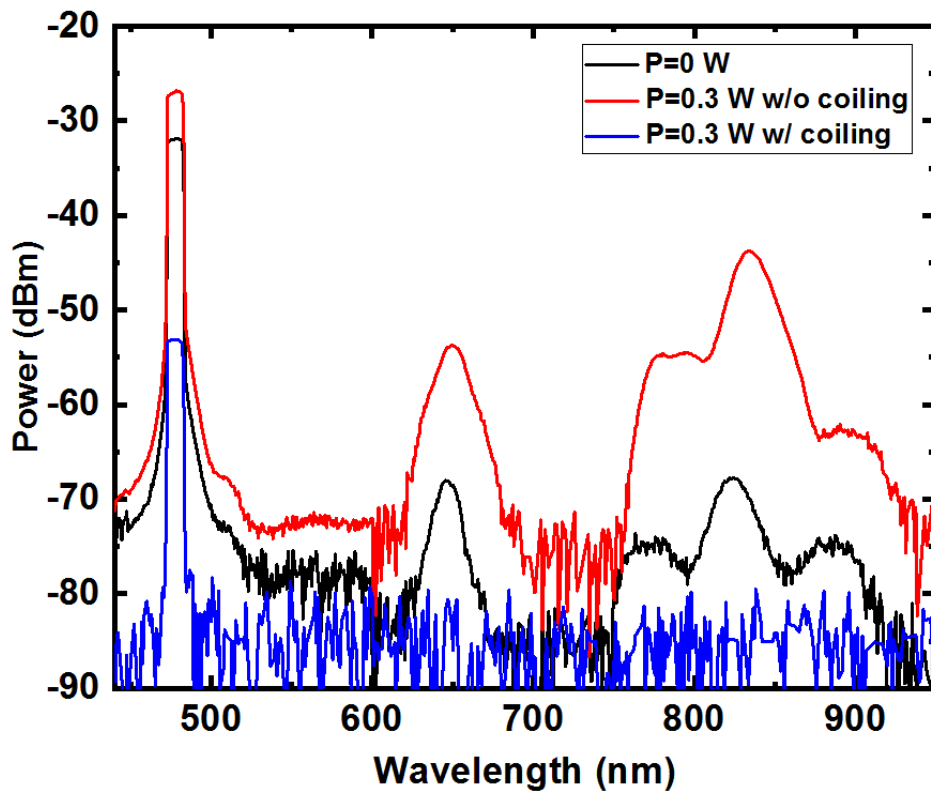
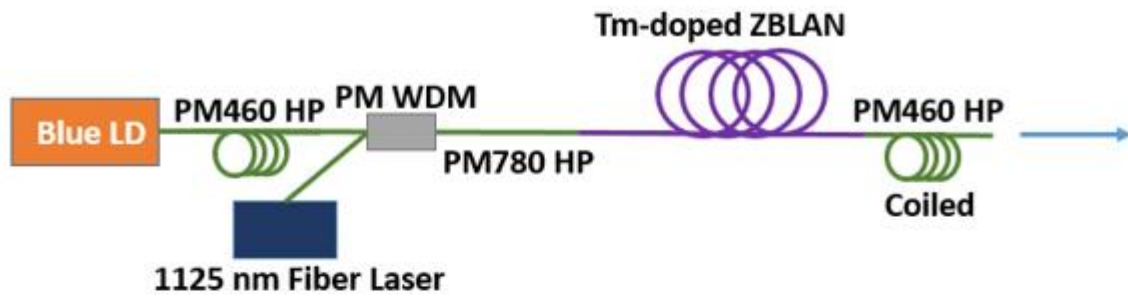


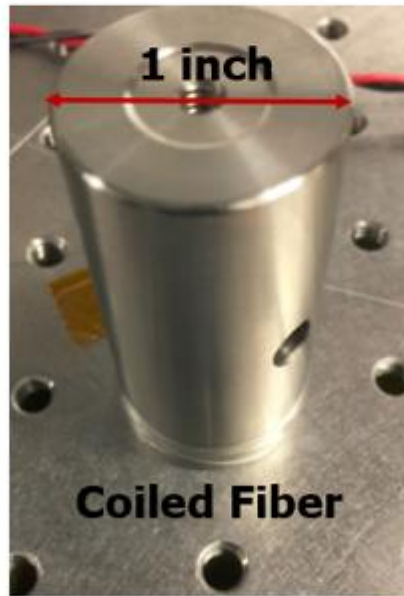
Fig. 1.36: Optical spectrum of signal output when there is no pumping, 0.3 W pumping without coiling, and 0.3 W pumping with coiling.

We also did another experiment and this experiment we coiled the input PM460 HP fiber too as shown in Fig. 1.37 (a). An optical post was used to coil the fiber as shown in Fig. 1.37 (b). In

this experiment the diameter of the coiling was about 1 inch and about 5 round the PM460 HP fibers were wrapped around the post. The effectiveness of the coiling is better than the previous experiment since the loss of blue light wasn't very significant. The reason that both sides are coiled is because to make sure if there is a reflected light back is not going to have effect on the experiment.



(a)



(b)

Fig. 1.37: (a) Experimental setup to study the effect of coiling which input fiber and output fiber are coiled; (b) optical post was used to coil the fiber.

Fig. 1.38 illustrates the optical spectra of fiber laser amplifier when the pump power was 1.2 W with bending and without bending, and also when the pump power was 1.5 W with bending and without bending. After bending the emission around 800 nm is completely removed in both cases, but emission at 650 nm emission is still there.

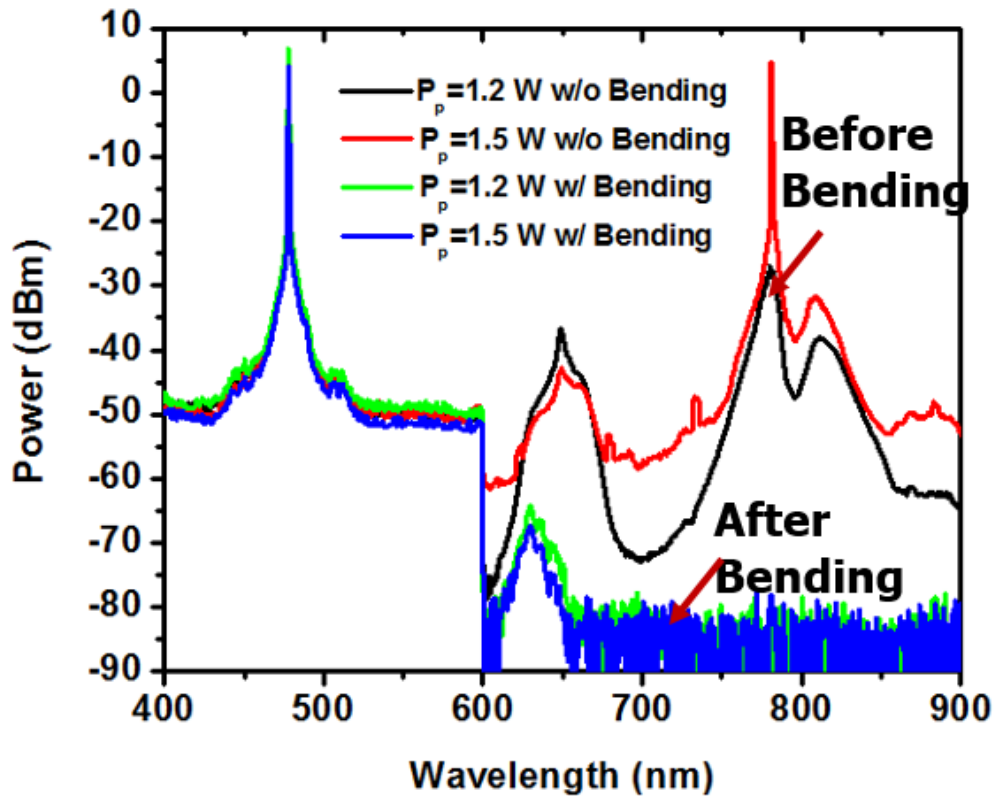


Fig. 1.38: Optical spectra of fiber amplifiers with pump power at 1.2 W and 1.5 W with bending and without bending..

This result indicates that designing a proper waveguide to remove 800 nm emission band can be an effective method to increase the blue laser emission. The optical spectrum of fiber amplifier at different pump power based on the schematic setup of Fig. 1.35 is shown in Fig. 1.39. As the pump power increases the signal output increases too, but the emission of 800 nm band appears at the pump power of 0.66 W. From the pump power of 0.96 W to 1.5 W, the signal emission

increased by 2 dB, while the 800 nm emission band raised by 7.7 dB. Since the emission around 800 nm causes by ${}^1G_4 \rightarrow {}^3H_5$ and ${}^3H_4 \rightarrow {}^3H_6$ and the longer edge of the emission goes above 820 nm, it seems the contribution from ${}^3H_4 \rightarrow {}^3H_6$ which has the dominant contribution in longer edge of the emission is suppressed.

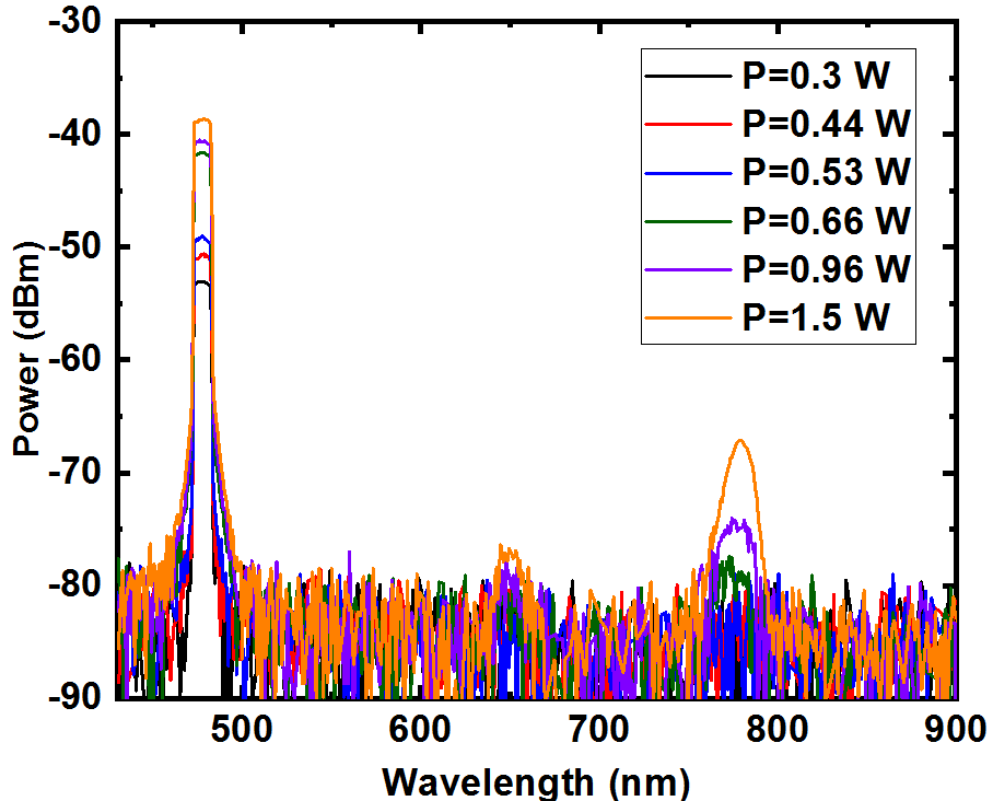


Fig. 1.39: The optical spectrum of fiber amplifier at different pump power when the output power is coiled.

Another obstacle to achieving long-term and stable high power single mode blue laser output is the degradation of the Tm^{3+} -doped ZBLAN fiber caused by the photodarkening effect. Photodarkening describes a significant increase of background loss at visible wavelengths due to the creation of color centers in the ZBLAN glass matrix of ZBLAN glass under illumination with a strong blue laser [53,54]. The photodarkening effect in Tm^{3+} -doped ZBLAN is particularly

strong because Tm^{3+} has a large range of energy levels including levels with energies higher than 1G_4 that are capable of absorbing and emitting UV light.

In this experiment, a 15 m fiber was used before was cut to a 5 m fiber and 10 m fiber. The 5 meter fiber was cured and pumped as you can see in Fig. 1.40. The almost fresh fiber could reach to a maximum of 103 mW.

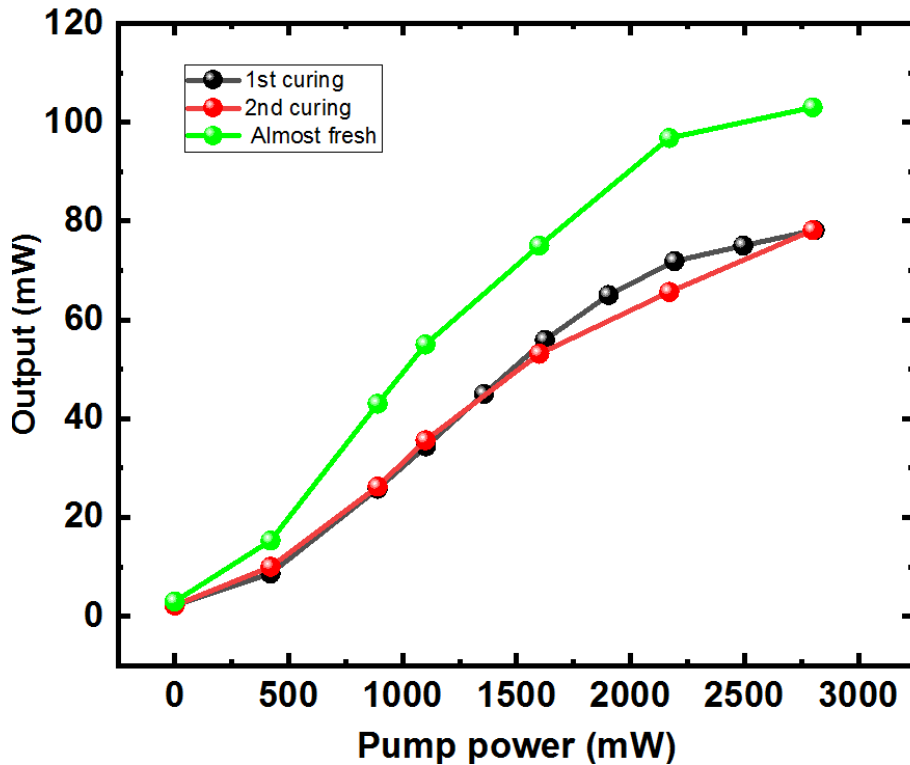


Fig. 1.40: Output optical power as a function of pump power for a fresh fiber, 1st curing, and 2nd curing test.

When the output power got saturated, the pump power was turned off and the fiber was under curing by blue signal for about 200 minutes. The signal power increased from 1.1 mW to 1.4 mW. Then the blue signal was amplified, and the maximum obtained output power was about 78 mW. After pumping the fiber, the pump again was turned off and just blue signal was used to

cure the fiber again. As it is shown in Fig. 1.41, the signal power increased from 0.4 mW to 1.5 mW after leaving the fiber under blue signal curing for about 25 hours. It indicates that signal power increased by 5.7 dB. Then the gain fiber was pumped again, and the same maximum of 75 mW was obtained again. Which means it could obtain the same output power with the second curing process as it was obtained by the first curing process.

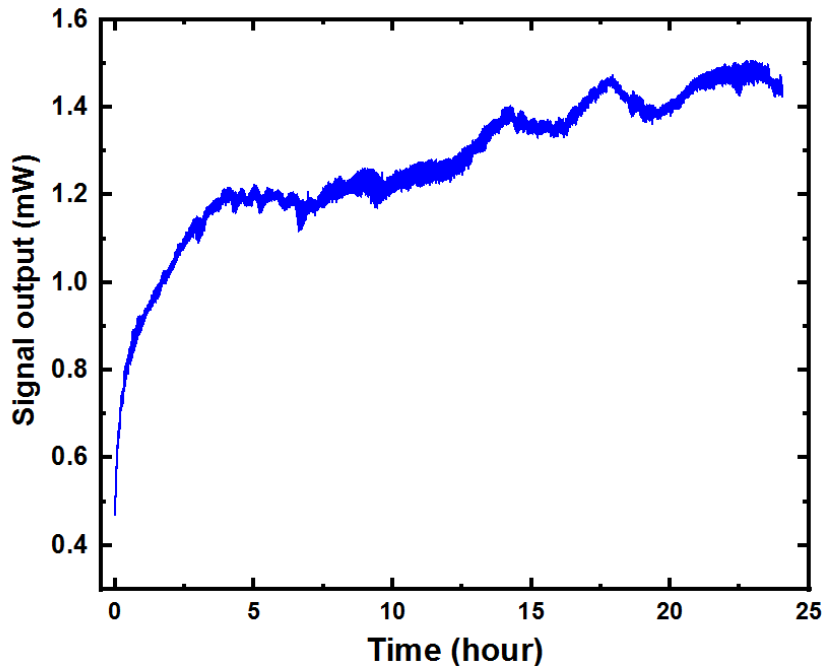


Fig. 1.41: The dynamic process of curing fiber by blue signal power as a function of time for the second time.

In general, it was found that blue laser signal transmitted through the Tm^{3+} -doped ZBLAN fiber amplifier significantly decreased (from a few mW to tens of μW) after running at the maximum output power and then leaving unpumped for one day. However, the photodarkened Tm^{3+} -doped ZBLAN fiber can be photo-cured by launching the blue laser into the fiber core and pumping it at a low pump power for a few hours as it was mentioned above. The maximum output power of the photo-cured fiber amplifier could be 75% of the initial maximum output power. It was also

found that photodarkening and photo-curing of the Tm^{3+} -doped ZBLAN fiber were repeatable to some extent.

In another experiment, the photodarkening effect in the Tm^{3+} -doped ZBLAN fiber was found to be not uniform through the length of the fiber. The transmission spectra of the first 1-m segment at the beginning and the last 1-m segment at the end of the photodarkened amplifier fiber, and a 1-m of fresh fiber (never pumped) were measured using a white light source and an OSA and are shown in Fig. 1.42. Contrary to our initial expectation, the first 1-m segment of the amplifier fiber, where the blue laser power is low, was severely photodarkened while the last 1-m segment of the amplifier fiber, where the blue laser power is much higher, experienced little photodarkening, indicating that the photodarkening is not solely induced by the blue laser and may be a function of the population at the upper laser level $^1\text{G}_4$. It was also observed that photodarkening occurs only after the parasitic 800 nm laser begins. Several previous papers have tried to help in the understanding of photodarkening[53,54]. But none of them can be used to explain the phenomena observed in our fiber amplifier experiment. Therefore, further investigation and new interpretations of photodarkening in Tm^{3+} -doped ZBLAN fiber are essential for further developments of high power fiber amplifier for blue lasers.

In conclusion for this section, an all-fiber amplifier for single-frequency blue laser was demonstrated for the first time. More than 150 mW continuous-wave, single frequency and single-transverse-mode 478 nm laser output was obtained with an 1125 nm pump laser at a power of 2 W. The output power was saturated and began to decrease for the pump powers exceeded 2 W due to the onset of the 800 nm lasing. It was observed that the effect of photodarkening is not uniform across the amplifier fiber and further investigations of photodarkening in Tm -doped ZBLAN fiber amplifier is essential. Further power scaling of the Tm^{3+} -ZBLAN fiber amplifier

can be achieved by sufficiently suppressing the 800 nm laser with optimized Nd^{3+} concentration in the inner cladding and a proper fiber design with tailored guide at different wavelengths.

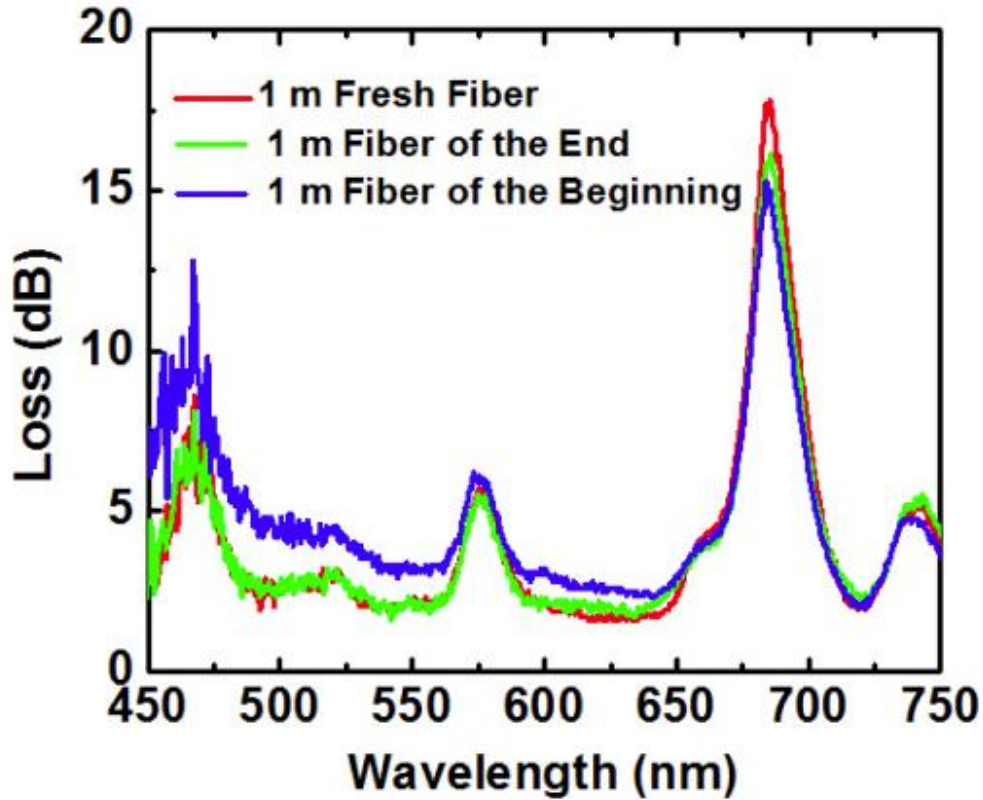


Fig. 1.42: Measured loss of 1 meter fresh (unpumped) fiber, 1 meter segment of the end and 1 meter segment of the beginning of the photodarkened amplifier fiber.

1.4 Blue laser fiber amplifier for under water optical communication

Under water communication system (UWCS) has been drawing a lot of attention due to its extensive applications which span from scientific, and commercial to military purposes. Currently, UWCSs are based on an acoustic wave, radio frequency (RF) wave, and optical wave.

Under water optical communication system (UWOCS) which uses optical wave has low cost, low latency, high data rate and bandwidth compared to the other two systems. The maximum transmission in ocean water was found to be in the blue-green region with a peak near 480 nm which can shift depending on the dissolved substances in the water [55]. Blue light emitting diodes (LED) have been used in UWOCS to increase the transmission range and data rate [56,57]. However, LEDs suffer from insufficient modulation bandwidth and large divergence angle [58]. Therefore, several works showed that blue laser diode with high modulation bandwidth and low divergence angle can be a promising source for UWOCS [59–61]. But still these systems need to improve their transmission range. One way to enhance the transmission range is to increase the signal power, which can be achieved by a compact and environmentally stable laser source with high power, and excellent beam quality.

Since fiber lasers usually have advantages including power scalability, low thermal effect, compactness, and low cost of maintenance, several groups have conducted research on thulium (Tm^{3+}) doped fluoride blue fiber lasers [21,24,25]. However, all of the Tm^{3+} -ZBLAN fibers used in these experiments are multimode with the cutoff wavelengths > 800 nm and thus the output laser beams were not robust single transverse mode at all. Most importantly, since these upconversion lasers were constructed with several meter Tm^{3+} -ZBLAN fiber in linear cavity, their output was not single longitudinal mode either. Moreover, because bulky mirrors were used in these lasers to form the cavity and free-space optics were used to couple the pump power into the gain fiber, these fiber lasers needed careful alignment and were not stable and reliable for in-field applications. In this work we proposed using Tm^{3+} -ZBLAN fiber amplifier to amplify laser diode output. Fiber laser amplifier is a promising approach to obtain a compact, reliable, high power, and a single mode blue coherent light for UWOCS applications. Recently, a Tm^{3+} -

ZBLAN fiber amplifier was used to amplify a single frequency blue laser diode [20]. The maximum obtained output power was 155 mW. The limited output power was due to low seed laser power, photodarkening, and inset of 800 nm emission. In this experiment a single mode all fiber amplifier, amplifying a laser diode operating at 478 nm was demonstrated. The maximum output power was about 240 mW. The pump threshold was about half of previous experiment and the input signal was higher than previous work which is due to a better design of wavelength division multiplexor (WDM), enabling a higher efficient light coupling into the gain fiber, and utilizing higher laser diode output signal power.

In blue laser fiber amplifiers, a blue diode laser can be used as a seed laser. Coupling light from a diode laser to a single mode fiber needs a good mode matching. A general expression for coupling efficiency between a laser diode with an elliptical Gaussian mode and a single mode fiber with circular Gaussian mode can be written as:

$$T = \frac{4\omega_{fiber}^2\omega_x\omega_y}{(\omega_x^2 + \omega_{fiber}^2)(\omega_y^2 + \omega_{fiber}^2)} \quad (1)$$

Where T , ω_{fiber} , ω_x , ω_y , are coupling efficiency, mode field radius of fiber, beam waist of x axis and y axis of elliptical beam at the fiber plane respectively.

Fig. 1.43 shows the schematic design for converting an elliptical output beam of a laser diode with an elliptical beam shape to a circular beam. In this method an aspheric lens collimates the light on fast axis and slow axis then a laser beam expander is used to expand the beam. Laser beam expanders increase the diameter of a collimated input beam to a larger collimated output beam. The two common beam expanders are Keplerian telescope, and Galilean telescope. Since

in Keplerian telescope, the beam is focused between objective lens and eyepiece, is usually used when spatial filtering is needed. In this experiment, Galilean telescope was used as the beam expander to expand the beam with lower NA which in this case is on x direction as NA_y, NA_x are 0.2 and 0.05 respectively. In order to have the minimum effect on y direction, the toroidal lenses were used to build the Galilean telescope oriented on x direction. Since $NA_y/NA_x=4$, the beam expander (Galilean telescope) should have magnification power (MP) of 4 which leads to $f_2/f_1=4$.

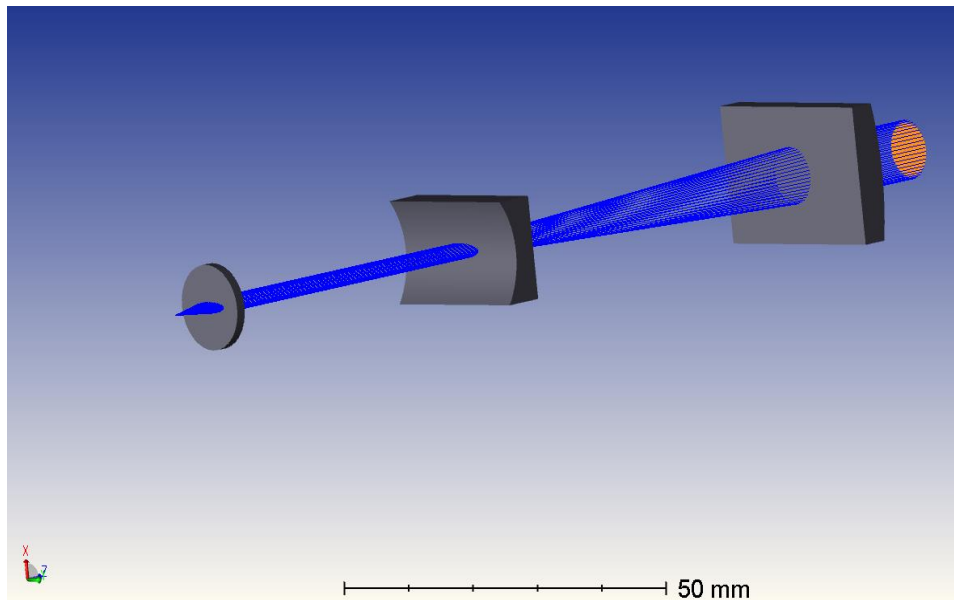


Fig. 1.43: Schematic design for creating a circular beam from an elliptical laser diode beam.

The cross section of schematic design of the setup for coupling an elliptical beam to PM 460HP fiber is shown Fig. 1.44. The beam expander was used on x direction to match the beam diameter of x direction to y direction. As it can be seen beam is getting expanded while it is traveling in Galilean telescope. The spot size evolution of the beam is also shown in Fig. 1.44. Beam is elliptical at lens #2 and then after lens #3 it is almost circular. After coupling into the fiber, Zemax

fiber coupling was used to calculate the coupling efficiency. The coupling efficiency was found to be 84%.

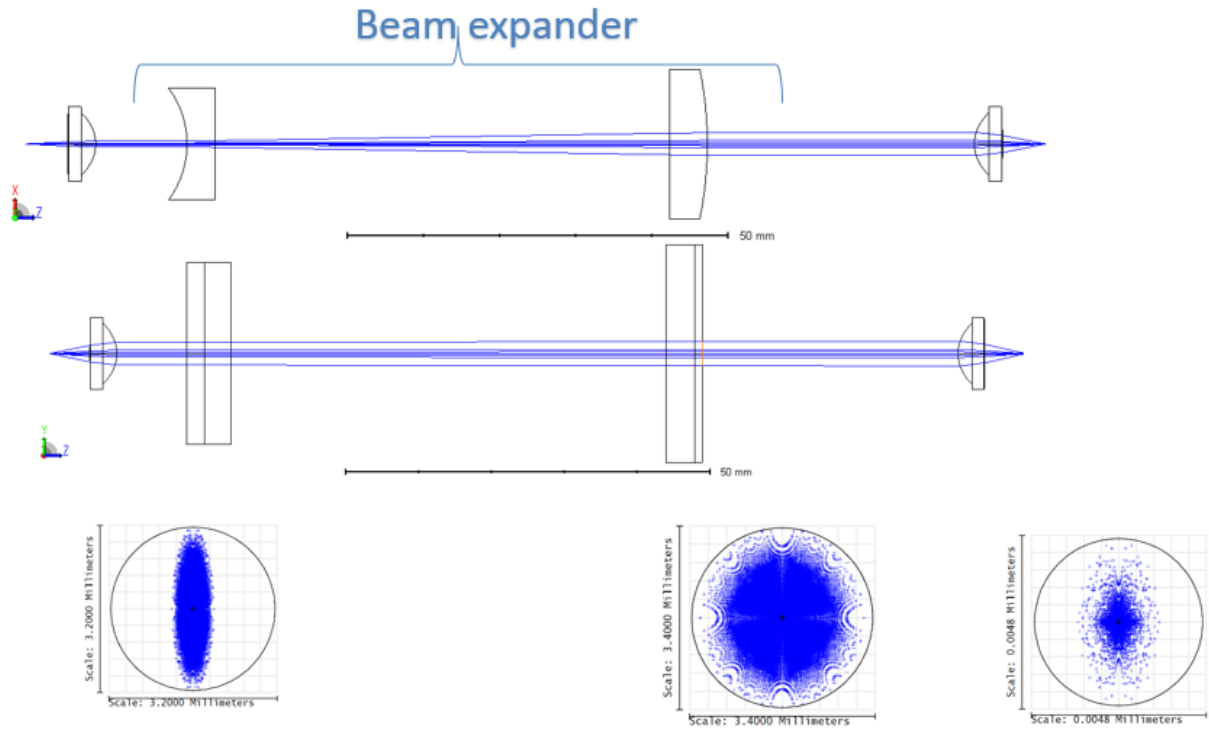


Fig. 1.44: The cross section of schematic design of the setup for coupling an elliptical beam to PM 460HP fiber and spot size evolution after lens #2, lens #3, and at the fiber.

The amplified spontaneous emission spectrum of Tm^{3+} -ZBLAN fiber is shown in Fig. 1.45. Tm^{3+} -ZBLAN fiber was pumped by 1125 nm pump. The emission peaks at 450 nm and 650 nm are due to $^1\text{G}_4 \rightarrow ^3\text{H}_6$ and $^1\text{G}_4 \rightarrow ^3\text{F}_4$ respectively. The peaks at 750 nm and 825 nm are due to the combination two transitions: $^1\text{G}_4 \rightarrow ^3\text{H}_5$ and $^3\text{H}_4 \rightarrow ^3\text{H}_6$.

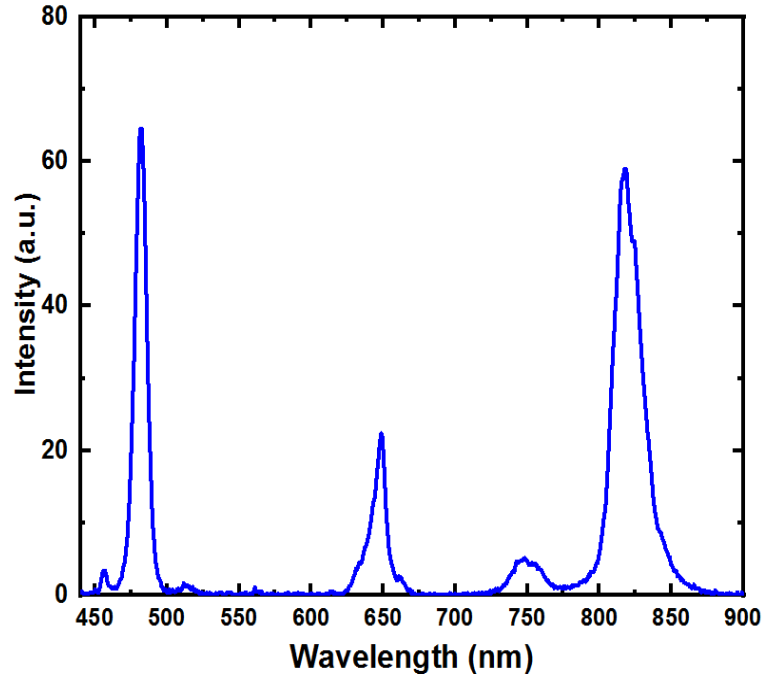


Fig. 1.45: The amplified spontaneous emission of Tm^{3+} - ZBLAN fiber. Inset: Amplified spontaneous emission at different pump powers.

It should be noted with pumping harder the ground state gets depopulated and the two emission peaks at 750 nm and 825 nm merged to one peak. It should be noted that $^1\text{G}_4 \rightarrow ^3\text{H}_5$ and $^3\text{H}_4 \rightarrow ^3\text{H}_6$ transitions can have influence on the laser amplifier operating at 480 nm. As discussed in the previous section, with increasing pump power the emission around 800 nm gets stronger and broader compare to 480 nm emission, which is due to the fact that in order to emit 480 nm the ions need to be excited to $^1\text{G}_4$ with three photons upconversion, while emitting at 800 nm beside $^1\text{G}_4 \rightarrow ^3\text{H}_5$, it can happen with $^3\text{H}_4 \rightarrow ^3\text{H}_6$ which needs just two photons upconversion. Also, due to emptiness of $^3\text{H}_5$ energy level, population inversion for the 785 nm transition is achieved much easier compare to 480 nm emission.

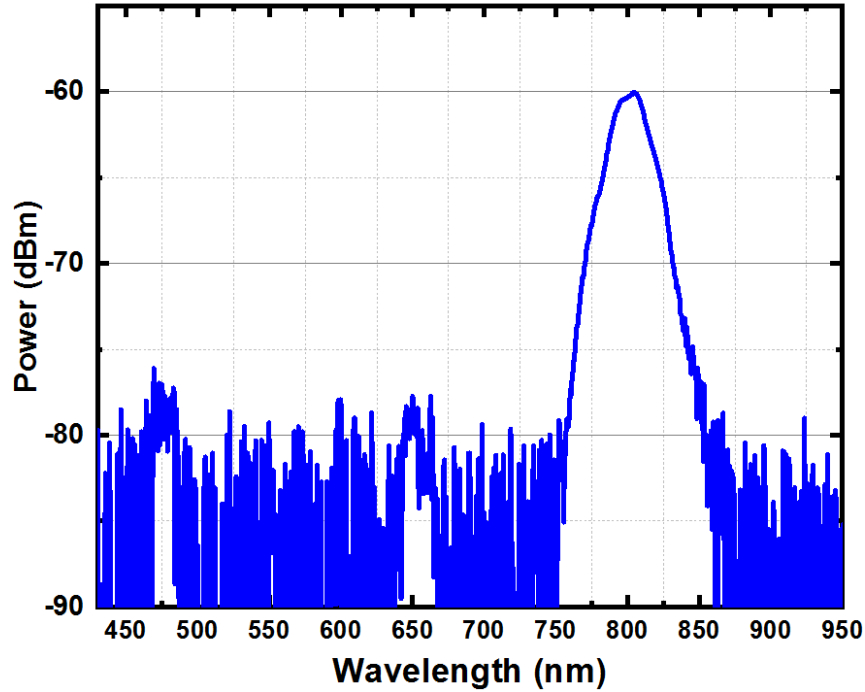


Fig. 1.46: Amplified spontaneous emission of Tm^{3+} ZBLAN fiber pumped by 1210 nm laser diode.

As discussed earlier, the reason that the wavelength of pump laser wasn't 1210 nm which has the highest peak absorption for ground state is due to the fact that it doesn't have high absorption in excited state. As shown in Fig. 1.46 the Tm^{3+} ZBLAN fiber was pumped by 1210 nm laser diode and the amplified spontaneous emission is significant around 810 nm which is due to ${}^3\text{H}_4 \rightarrow {}^3\text{H}_6$. And emission around 480 and 650 nm are not significant.

The schematic of the single mode fiber blue laser amplifier setup is shown in Fig. 1.47. A Nichia blue laser diode operating at 478nm was used as the seed laser and coupled to single-mode silica fiber PM 460HP with NA of 0.12, ModeField Diameter (MFD) of $3.3 \mu\text{m}$, and cutoff wavelength of 410 nm. An ytterbium (Yb^{3+}) doped silica fiber laser operating at 1125 nm was used as the pump source. A PM wavelength division multiplexor (WDM) made of PM 460HP (signal port)

and PM780 HP fiber (pump and common port) was used to combine the seed signal laser and the pump laser together. In order to keep a single spatial mode the common port needs to be short and straight. The signal coupling efficiency is less than 80% and the pump coupling efficiency is about 90%. It should be noted that the common port fiber of the PM-WDM needs to be kept straight on the optical table to reduce power fluctuations and decrease of the fundamental mode caused by small bending and other environmental effects. 7.5-m of Tm^{3+} -ZBLAN fiber was spliced to the common port PM780 HP fiber. The typical loss of the splice between a ZBLAN fiber and a silica fiber is less than 0.3 dB. The output end of the ZBLAN fiber was angle cleaved to reduce backward reflections. A band-pass filter at 480 nm was used to remove the residual pump at 1125 nm.

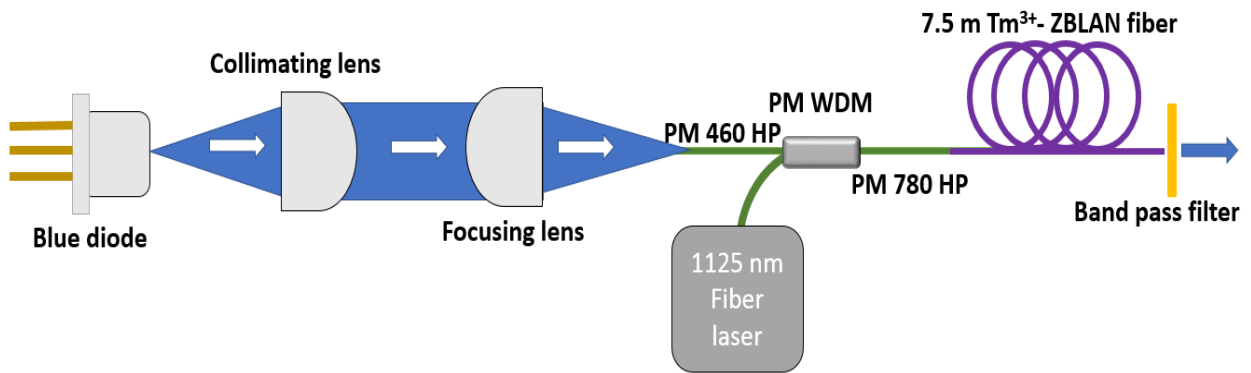


Fig. 1.47: Experimental setup for single mode fiber blue laser amplifier.

The beam quality of Tm^{3+} -ZBLAN fiber at 478 nm was measured using a beam profiler (DataRay Inc., Beam Map2) in a separate experiment using blue laser. The 2D beam profile is shown in Fig. 1.48 (a), and Cross section of the beam profile and its Gaussian fit are shown in Fig. 1.48 (b). The measured M^2 was 1.28 and the cross section of the measured beam was fitted to a Gaussian fit with 98% accuracy.

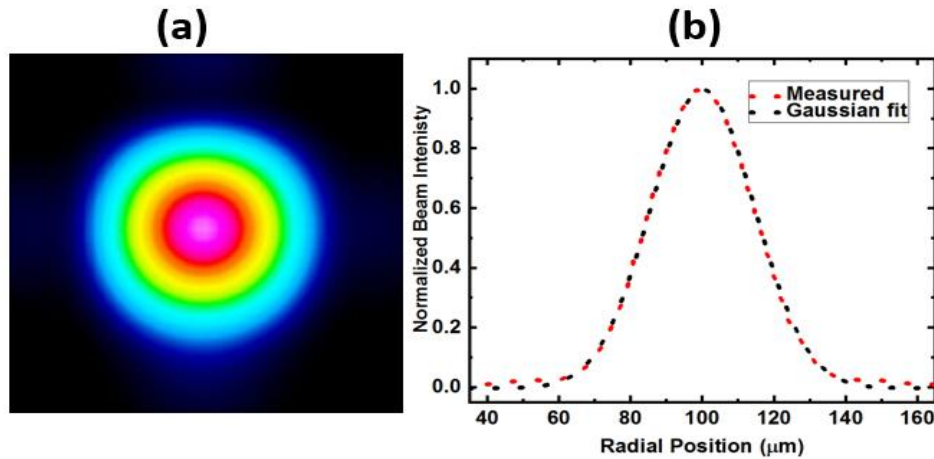


Fig. 1.48: a) 2D profile of the fiber output beam at 478 nm; (b) Cross section of the output beam profile and its Gaussian fit.

The coupling efficiency from diode to PM460 HP was about 50%. It could have a better efficiency if the rotational asymmetric emission of diode gets corrected by the coupling system. The output power of the fiber amplifier as a function of the pump power was measured by a power meter (Thorlabs, PM100D) as shown in Fig. 1.49. **Error! Reference source not found.** The blue laser output increases with pump power and then drops when the pump power exceeds 3 W. A maximum output power of 235 mW, corresponding to a net gain of about 9.2 dB and the slope efficiency of 9% were obtained. The optical spectrum of the diode laser is shown in the upper left inset of Fig. 1.49. Having a higher initial signal power, and a better coupling efficiency between PM780 HP fiber and gain fiber compared to the coupling efficiency between PM980 HP fiber and gain fiber as shown in lower right inset of Fig. 1.49 resulted in the decrease of the pump threshold of the fiber amplifier by half to about 500 mW compare to pervious experiment. On the other hand, using PM780 HP led to a lower coupling efficiency of pump power in WDM which causes a lower slope efficiency.

As it was shown in the previous work [20], the reason that amplifier output achieved its highest power at 3 W pump power and then it decreases as the pump power increased, is due to the onset of strong emission at 800 nm band. So, a proper fiber design that can reduce emissions from $^1G_4 \rightarrow ^3H_5$ and $^3H_4 \rightarrow ^3H_6$, while maintaining high emission of $^1G_4 \rightarrow ^3H_6$ needs to be investigated. Since photodarkening is a limiting factor in amplifying blue light[20], and pumping by near IR has a major role in photodarkening, a two stage amplifier can be used to increase signal output while the pump power at each stage is relatively low.

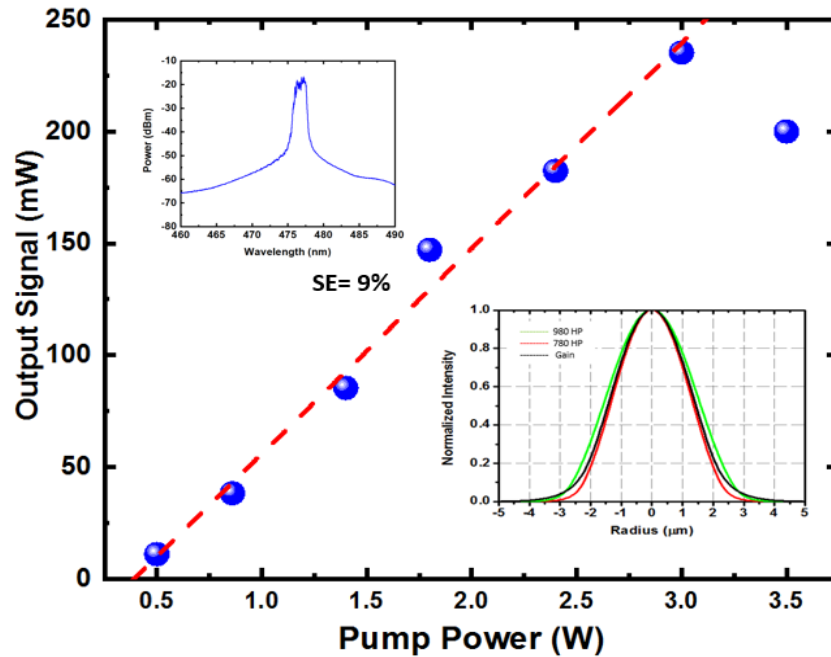


Fig. 1.49: Output power with respect to the launched pump power for 7.5 m Tm³⁺-ZBLAN. Upper left: The optical spectrum of laser diode. Lower right: Mode field diameter of 980 HP, 780 HP, and gain fibers.

In conclusion, A single-mode fiber amplifier operating at 478 nm was demonstrated for the concept of blue diode laser oscillator and fiber power amplifier for underwater optical communication system. About 240 mW continuous-wave output signal power was obtained at

478 nm, with 3 W pump laser operating at 1125 nm and then output power began to decrease due to the onset of the 800 nm emission. The net gain amplifier was found to be about 9.2 dB with 9% slope efficiency.

Chapter 2 Tm³⁺-Doped Fluoride Fiber Laser at 785 nm

2.1 Introduction

Laser sources in the 785 nm band have found a variety of applications including remote sensing, spectroscopy, medicine, and scientific research. Laser sources at 785 nm have been widely used by dermatologists to study the sunburn skin reaction [62], and have also been extensively used for Raman spectroscopy because the fluorescence of most organic molecules excited at this wavelength is very low and detectable Raman signal with a reasonable signal-to-noise ratio can be produced at a pump power that does not cause substantial photodamage in biological studies [63]. Most recently, a 785 nm laser was used to pump perovskite platelet crystals to achieve laser cooling with a temperature decrease by 23 K [64]. Laser emission in the 785 nm band can usually be obtained from diode lasers, Ti:sapphire laser, and through frequency-doubling of L-band lasers in the third telecommunication window. In 2014, Sumpf *et al.* reported a 215 mW distributed Bragg reflector diode laser at 785 nm [65], however, the output power of a single-mode diode laser is generally limited to hundreds of mW. Higher output power can be achieved with semiconductor laser amplifiers and laser beam combing techniques [66], but the beam quality is always degraded and power scaling is usually limited by thermal issues of in the semiconductor. Although a 5 W wavelength tunable Ti:sapphire laser was demonstrated in this wavelength band [67], further power scaling is limited by thermal-optical problems and the crystallographic properties of Ti:sapphire. In addition, Ti:sapphire lasers require careful alignment and frequent maintenance. So far, frequency doubling of fiber lasers in the L-band is the most successful approach for producing high power laser output at the 785 nm band. Over 40 W at 780 nm was obtained by the frequency doubling of the output of an Er³⁺ doped fiber

amplifier [68]. However, harmonic generation lasers are very sensitive to their environment and lack agile wavelength tunability. Because fiber lasers have the advantages of high power scalability, excellent beam quality, and outstanding heat dissipation capability, fiber lasers based on direct emission at 785 nm should be able to overcome the constraints of the laser sources mentioned above and produce high power lasers with outstanding features required for various applications. In this section, we report our investigation on the power scaling of Tm^{3+} -doped fluoride fiber laser at 785 nm.

2.2 Spectroscopy

Spectroscopy of ZBLAN glass and blue emission of Tm^{3+} -doped fluoride glass discussed in the previous chapters. This section is focused on the emission at 785 nm in Tm^{3+} ZBLAN glass.

As shown in Fig. 2.1, the transition ${}^1\text{G}_4 \rightarrow {}^3\text{H}_5$ of Tm^{3+} can produce emission in the 785 nm band. However, this transition is usually diminished in high phonon energy glasses such as silica and phosphate due to multi-phonon non-radiative decay. Efficient emission from the ${}^1\text{G}_4 \rightarrow {}^3\text{H}_5$ transition of Tm^{3+} can be obtained in ZBLAN ($\text{ZrF}_4\text{-BaF}_2\text{-LaF}_3\text{-AlF}_3\text{-NaF}$), which is the most stable heavy metal fluoride glass and has a phonon energy as low as 500 cm^{-1} . ZBLAN is an excellent host for rare-earth ions and has been extensively used for efficient and compact ultraviolet, visible, and infrared fiber lasers [17]. In addition to the emission in the 785 nm band, Tm^{3+} doped ZBLAN has a broad range of emission wavelengths from $2.3\ \mu\text{m}$ (${}^3\text{H}_4 \rightarrow {}^3\text{H}_5$) to 284 nm (${}^1\text{I}_6 \rightarrow {}^3\text{H}_6$) and a variety of Tm^{3+} -doped ZBLAN fiber lasers have been reported [17,69–72]. Due to the great demand for blue laser sources, Tm^{3+} -doped ZBLAN fiber lasers in the blue have been extensively studied [20,53,73].

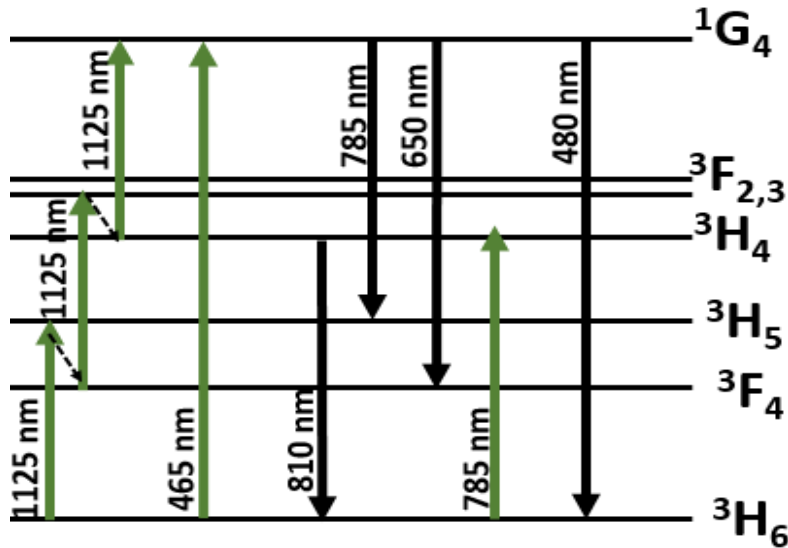


Fig. 2.1: Partial energy level diagram of Tm³⁺ and the transitions related to the laser emission at 785 nm.

Since the 785 nm laser transition is $^1G_4 \rightarrow ^3H_5$ the lifetime of both these energy levels are crucial. Walsh *et al.* used Judd–Ofelt theory to calculate the radiative lifetime of Tm³⁺:ZBLAN and Tm³⁺: Silica [74]. The lifetime of 1G_4 was calculated to be 0.9 ms, and 0.43 ms for Tm³⁺:ZBLAN and Tm³⁺: Silica respectively. Since the lower energy level of the 785 nm transition is 3H_5 having a short lifetime is more desirable. Walsh *et al.* calculated the lifetime of 3H_5 to be 6.9 ms, and 3.9 ms for Tm³⁺:ZBLAN and Tm³⁺: Silica respectively.

The power dependence of the upconversion emissions on the pump power of 1125 nm was measured, as shown in Fig. 2.2. In the initial stage the efficiency slope for all three upconversion emissions from 1G_4 is almost same. They grow as the pump power increase, which is a general description of three-photon upconversion processes. As the pump power increases, the slope efficiency decreases. The 480 nm emission band gets saturated, while the 650 nm emission band starts decreasing as pump power increases. However, 780 nm emission band still increases monotonically.

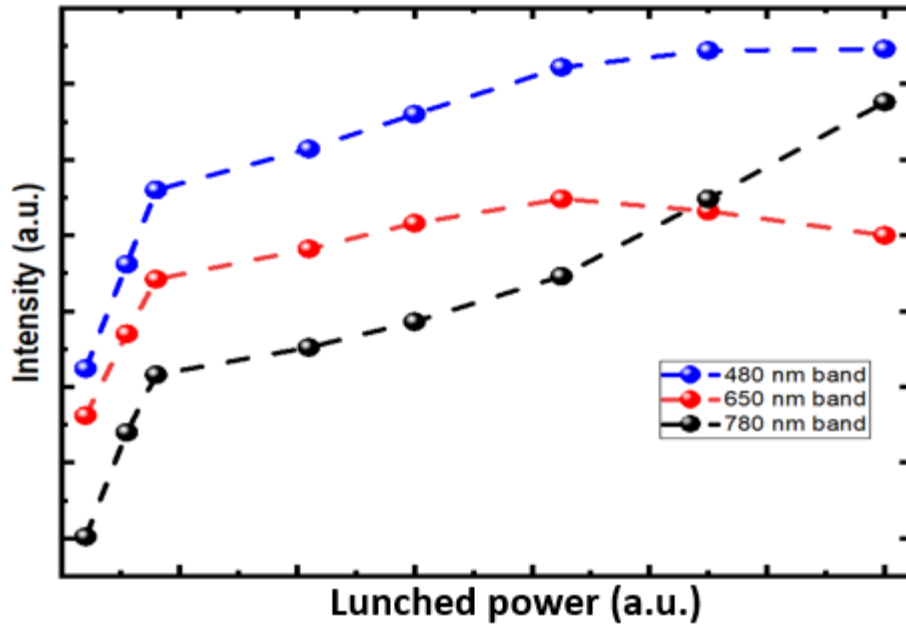


Fig. 2.2: Power dependence of upconversion emissions on pump power.

Compared to the substantial study of Tm^{3+} -doped ZBLAN fiber lasers at other wavelengths, investigation of the fiber lasers at 785 nm has lagged behind. In 2005, Qin *et al.* reported their study on the 784 nm amplified spontaneous emission of a Tm^{3+} -doped ZBLAN fiber [75]. Later, multi-wavelength laser emission was demonstrated with a 2 m 0.1 mol% Tm^{3+} -doped ZBLAN fiber. However, the output power of the fiber laser was only a few mW [76]. In 2007, dual-wavelength operation of a 0.2 mol% Tm^{3+} -doped ZBLAN fiber was investigated by Androz *et al* and about 30 mW of laser output at 785 nm was obtained [71].

It is worthwhile to note that all these previous experiments were demonstrated with multimode gain fibers and free space optics, which did not take advantage of the fiber laser geometry. In this chapter, we report the first demonstration of an all-fiber single transverse mode laser at 785 nm with, to the best of our knowledge, the highest output power (0.5 W) thus far reported.

2.3 Experiment, result and discussion

As shown in Fig. 2.1, Tm^{3+} ions can be excited to the upper laser level $^1\text{G}_4$ by either one photon pumping at 465 nm or upconversion multi-photon pumping at 1.1 μm . Directly pumping at 465 nm has the advantages of high conversion efficiency and no need of high pump density. However, high power single-mode diode lasers at 465 nm are still not available and the power levels of multimode diode lasers are not high enough to enable cladding pumping with high conversion efficiency due to the small absorption cross-section at 465 nm (about $1 \times 10^{-21} \text{ cm}^2$). Upconversion multi-photon pumping is currently still the most efficient method to excite to the $^1\text{G}_4$ level. In this experiment upconversion pumping at 1125 nm was used to populate the $^1\text{G}_4$ level because the three absorption transitions $^3\text{H}_6 \rightarrow ^3\text{H}_5$, $^3\text{F}_4 \rightarrow ^3\text{F}_3$, and $^3\text{H}_4 \rightarrow ^1\text{G}_4$ have their maximum effective absorption at this wavelength [51]. There are three major radiative transitions from $^1\text{G}_4$: $^1\text{G}_4 \rightarrow ^3\text{H}_5$, $^1\text{G}_4 \rightarrow ^3\text{F}_4$, and $^1\text{G}_4 \rightarrow ^3\text{H}_6$, emitting light at 785 nm, 650 nm and 480 nm, respectively, as shown by the fluorescence measured with a Tm^{3+} -doped ZBLAN glass in Fig. 2.3. It is noted that the measured fluorescence at 800 nm has contributions from two transitions $^1\text{G}_4 \rightarrow ^3\text{H}_5$ and $^3\text{H}_4 \rightarrow ^3\text{H}_6$. The branching ratios of the three transitions ($^1\text{G}_4$ to $^3\text{H}_6$, $^3\text{F}_4$ and $^3\text{H}_5$) are 0.378, 0.077, and 0.384, respectively [48].

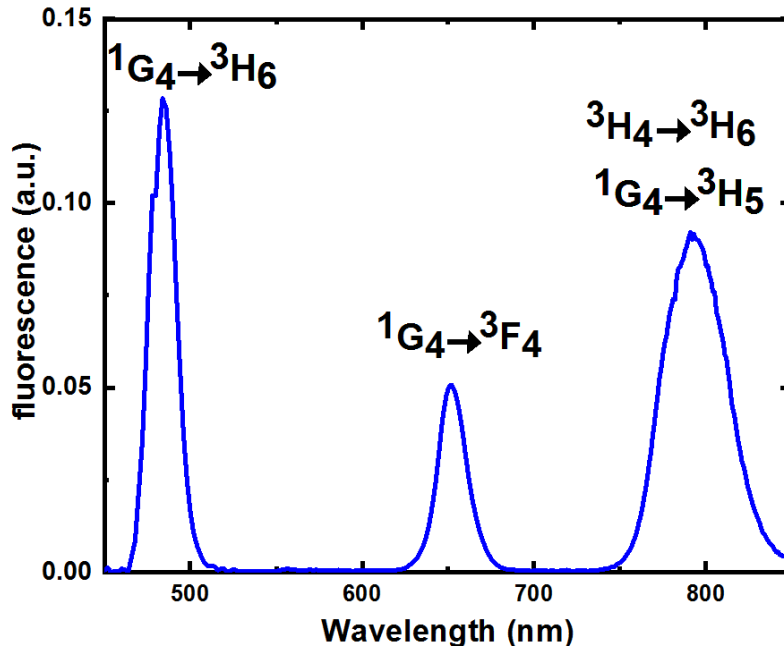


Fig. 2.3: Measured fluorescence of Tm^{3+} ZBLAN glass from $^1\text{G}_4$ energy level.

In our experiment, a Tm^{3+} -doped ZBLAN fiber with a core diameter of 4 μm and a numerical aperture (NA) of 0.07 was used as the gain fiber. The cladding diameter of this fiber is 125 μm , which is compatible with standard silica fibers enabling robust fusion splice for all-fiber laser development. The fiber core is doped with 0.1 mol% Tm^{3+} ions and the pump absorption of the fiber was measured to be 1.56 dB/m at 1125 nm by a cutback experiment.

The schematic of the all-fiber laser is shown in Fig. 2.4. An ytterbium (Yb^{3+}) doped silica fiber laser operating at 1125 nm was used as the pump source. Two fiber Bragg gratings (FBG) at 785 nm inscribed in the 780HP silica fiber cores were used to make the resonant cavity. A high reflection (HR) FBG with a peak reflectivity of 99.9% and a 3-dB bandwidth of 0.66 nm was used at the cavity mirror. A low reflection (LR) FBG with a peak reflectivity of 53.44% and a 3-dB bandwidth of 0.2 nm was used as the output coupler. The Tm^{3+} -doped ZBLAN fiber was

spliced to the two FBGs from both sides using a proprietary splicing technique [77]. An image of the splice joint between the silica fiber and the Tm^{3+} -doped ZBLAN fiber is shown in the inset of Fig. 2.4. The 1125 nm pump laser delivery fiber (HI1060) was spliced to the HR-FBG. The LR-FBG was spliced to the common port of a 785/1125 nm WDM made of 780HP fiber, which separates the residual 1125 nm pump laser and the 785 nm signal laser. The output power was measured with a power meter (Ophir StarBright), and the optical spectrum was measured with an optical spectrum analyzer (Ando, AQ6351A).

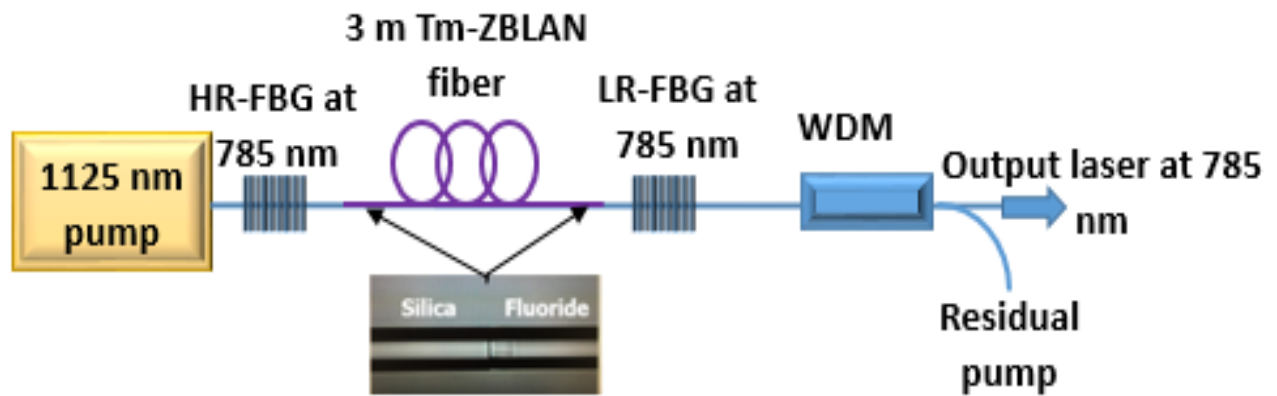


Fig. 2.4: Experimental setup of the all-fiber laser at 785 nm. Inset: microscopic image of the splice joint between the silica fiber and the ZBLAN fiber.

In our experiment, 3-m and 6-m Tm^{3+} -doped ZBLAN fibers were tested. The output power of the 3-m Tm^{3+} -ZBLAN fiber laser with respect to the launched pump power was first measured and is shown in Fig. 2.5. The pump threshold of this laser is about 1.2 W. The laser output increases linearly with increasing pump power, following typical laser performance for pump powers less than 4 W; in this regime the slope efficiency is about 2%. However, the slope efficiency of the laser increases dramatically as the pump power further increases. The slope

efficiency becomes 17.8% when the pump power exceeds 7 W. An output power of 0.485 W was obtained at 8.7 W pump power, which was the maximum pump power handling capability of our current ZBLAN fiber chains. The spliced ZBLAN fiber chain was found to burn at higher pump power because the cladding of the single-cladding ZBLAN fiber absorbs the uncoupled pump power.

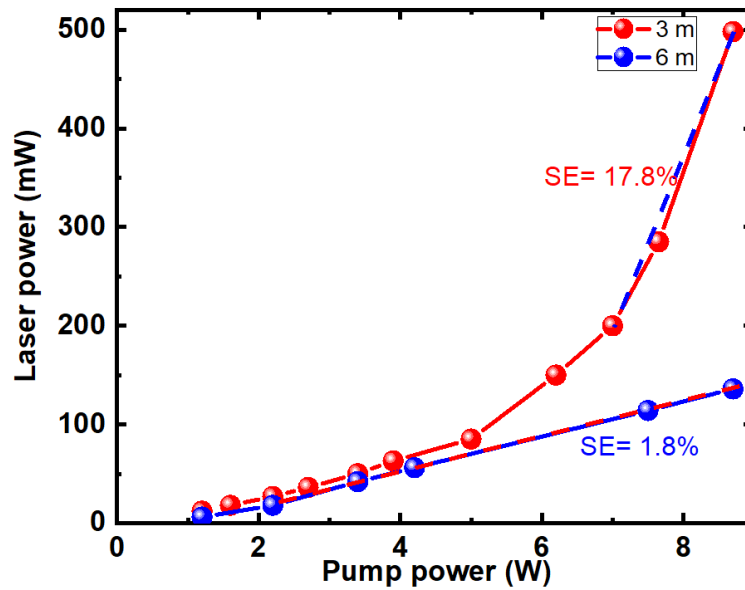


Fig. 2.5: Output power with respect to the launched pump power for the 3-m and 6-m Tm^{3+} ZBLAN fiber lasers.

The output power of the 6-m Tm^{3+} -ZBLAN fiber laser was also measured and is shown in Fig. 2.5. As opposed to the performance of the 3-m fiber laser, the output power of the 6-m fiber laser was a linear function of the pump power. The slope efficiency of the 6-m fiber laser is about 1.8% and the maximum output power of 136 mW was achieved for a pump power of 8.7 W.

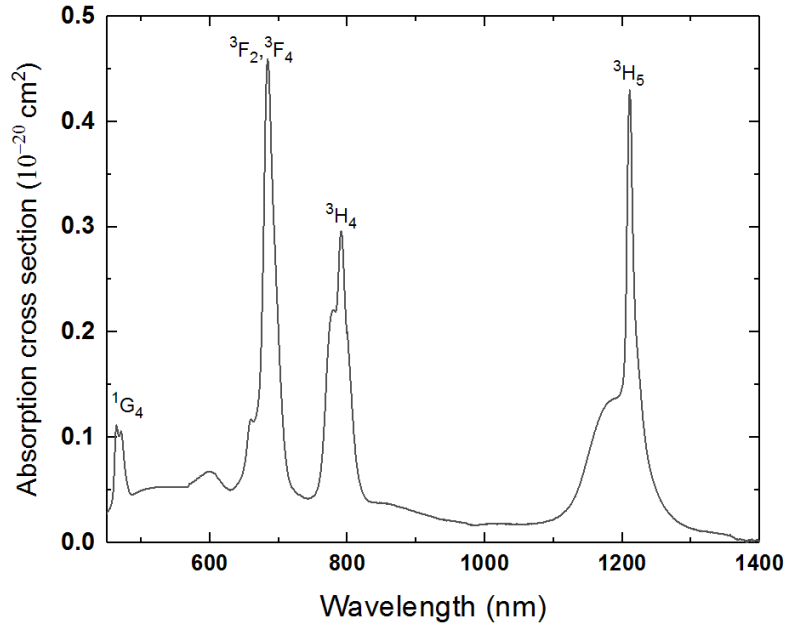


Fig. 2.6: The measured absorption cross-section of Tm^{3+} ZBLAN glass.

The difference in performance between the 3-m and 6-m fiber lasers is due to the strong absorption of Tm^{3+} at 785 nm and the small absorption at 1125 nm as shown in Fig. 2.6. Since the ground-state absorption ${}^3\text{H}_6 \rightarrow {}^3\text{H}_4$ is strong at 785 nm, the ions staying in the ground-state will absorb the generated 785 nm laser light and thus reduce the laser efficiency. In the 3-m fiber laser, the whole gain fiber segment is sufficiently pumped and the number of ions staying in the ground-state reduces significantly as the pump power reaches more than 5 W, such that good population inversion is achieved. As a result, fiber absorption at 785 nm reduces and the laser efficiency increases accordingly. In the 6-m fiber, however, the fraction of ions remaining in the ground-state is still significant at 8.7 W pump power and thus the nonlinear increase of the efficiency observed in the 3-m fiber laser is not observed in the 6-m one. The decrease in ground-state absorption at 785 nm with increasing pump power exhibits good agreement with the observation of Qin *et al.* [75]. They found that the ASE emission at 810 nm decreases with the

increasing pump power, which indicates that the number of ions in the ground state is reduced, while the emission intensity in the 785 nm band is growing. The spectrum of the all-fiber Tm^{3+} -ZBLAN laser was measured with the OSA and is shown in Fig. 2.7. The central wavelength is 784.5 nm and the 3-dB spectral bandwidth is 0.2 nm.

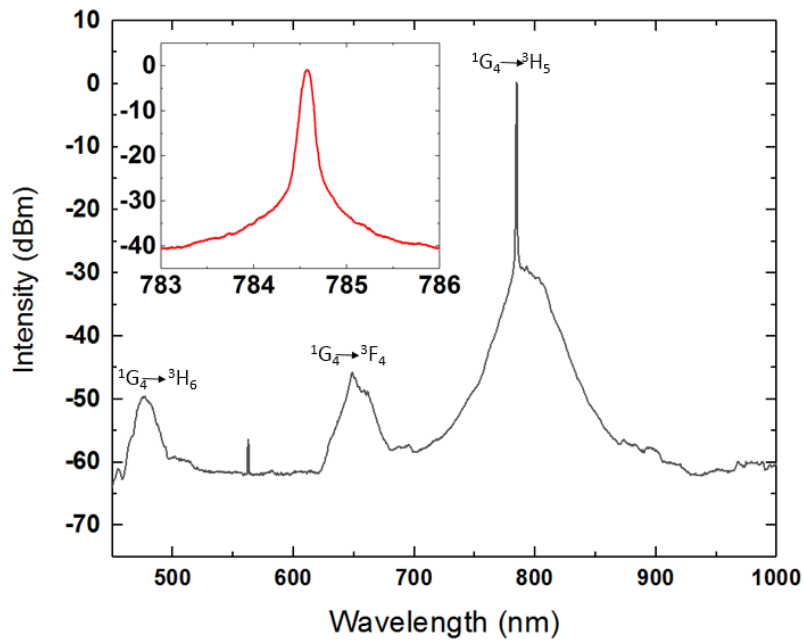


Fig. 2.7: Output optical spectrum of the all-fiber Tm^{3+} -doped ZBLAN laser measured in from 450 nm to 1000 nm. Inset shows the spectrum measured in the range from 783 nm to 786 nm with a resolution of 0.05 nm.

Androz *et al* observed self-pulsing Tm^{3+} -ZBLAN upconversion fiber laser in the region of 800 nm pumping with Yb laser operating at 1108 nm[71]. The self-pulsing of our system was tested by monitoring the output signal as a function of time shown Fig. 2.8. Two different time intervals of ms and μs were tested and their fluctuations were 0.16% and 0.7% respectively. No self-pulsing was observed in this setup.

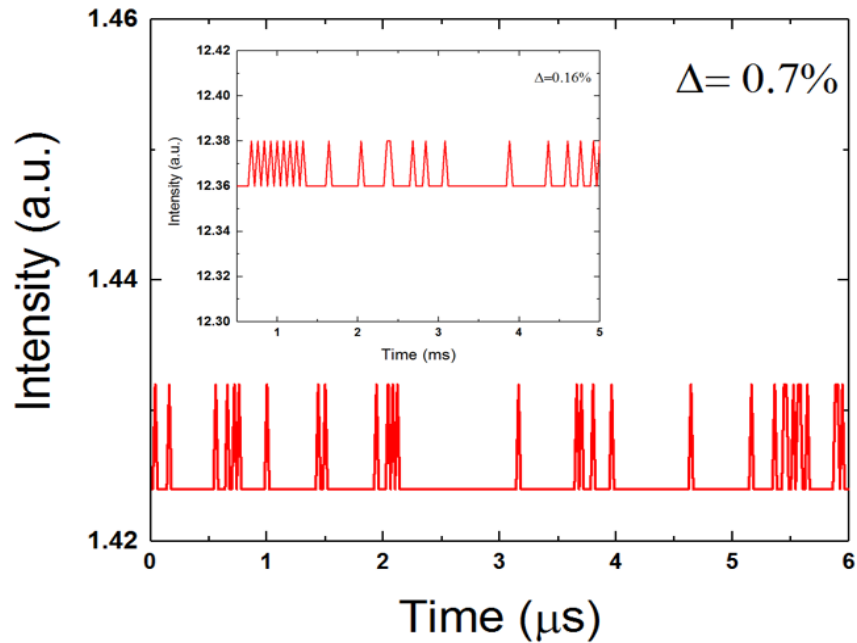


Fig. 2.8: Temporal evolution of signal power to test self-pulsing in μs interval. Inset: Temporal evolution of signal power to test self-pulsing in ms interval.

Our experimental results have shown that the efficiency of the Tm-doped ZBLAN fiber laser at 785 nm increases with the increasing pump power. It is expected that higher efficiency can be achieved at further increased pump powers. Nevertheless, the efficiency of the 785 nm fiber laser can be also increased by reducing the splice loss between ZBLAN fiber and silica fiber and improving overlapping of the fiber core with laser and pump. Direct pumping at 465 nm can also remarkably increase the efficiency. But there is no available high power single mode diode laser operating at 465 nm. Another technique that can increase the laser efficiency is to use dual pumping. The absorption cross section of the 1125 nm is very weak in the ground state, while this wavelength has a strong absorption in metastable energy level of 3F_4 and 3H_4 [51]. To reduce the population at the ground state and consequently increase the laser efficiency, a pump laser at the strong absorption peaks of Tm^{3+} can be used to depopulate the ground state and excite them

to 3F_4 energy level and the 1125 nm laser is used to carry on the upconversion. Therefore, dual-wavelength pumping may be a promising approach to achieve high efficiency fiber laser at 785 nm.

In conclusion, we have developed an all-single-mode fiber Tm^{3+} -doped ZBLAN laser operating at 785 nm and an output power of about 0.5 W was obtained at a pump power of 8.7 W. A maximum slope efficiency of 17.8 % was obtained with the 3-m fiber as the pump power exceeded 7 W. The efficiency of this all-fiber laser can be improved by reducing the splice loss, using a gain fiber with optimized overlap between the laser, the pump and the fiber core, and employing new pumping schemes to deplete the ground state sufficiently.

Chapter 3 Tm³⁺-Doped Silica Fiber Laser in 2 μm

3.1 Introduction

Over the past decade, fiber lasers have developed in all aspects of laser performance. Different types of applications have also been expanded for fiber lasers, from material welding, cutting, soldering, marking, cleaning, to medicine, research, and security. Fiber lasers have advantages such as excellent heat dissipation, single pass high gain, beam quality, freedom from alignment, compactness, and low maintenance, etc.

Fiber lasers are able to operate from deep UV to IR. Among different wavelengths that fiber lasers are able to operate, 2 μm region has drawn tremendous attention. 2 μm fiber lasers can be used for a vast variety of different applications. For instance due to smaller atmospheric scattering, atmospheric distortion and thermal blooming compare to 1 μm lasers, they are good candidates for light detection and ranging (LIDAR), direct energy laser weapon, sensing systems, and optical communication; 2 μm lasers are more efficient than 1 μm lasers for non-metal material processing applications such as direct cutting, welding, and drilling. Especially plastics are transparent in 1 μm region, while they have high absorption in 2 μm[78]; They have also attracted much attention for highly precise laser surgery for both soft and hard tissue owing to a strong water absorption peak near 2 μm as shown in Fig. 3.1 [79]; Due to water absorption in 2 μm region, lasers operating in this wavelength range are considered as eye safe lasers; 2 μm laser can be used as the pump sources for laser systems that emit at longer wavelengths in the mid-infrared or THz range[80,81]. Due to the high demands for high energy lasers at 2 μm, significant efforts have been made to develop 2 μm lasers in the last decade and most researches have been focused

on thulium (Tm^{3+}) laser due to strong absorption around 800 nm, where high-power laser diodes are available.

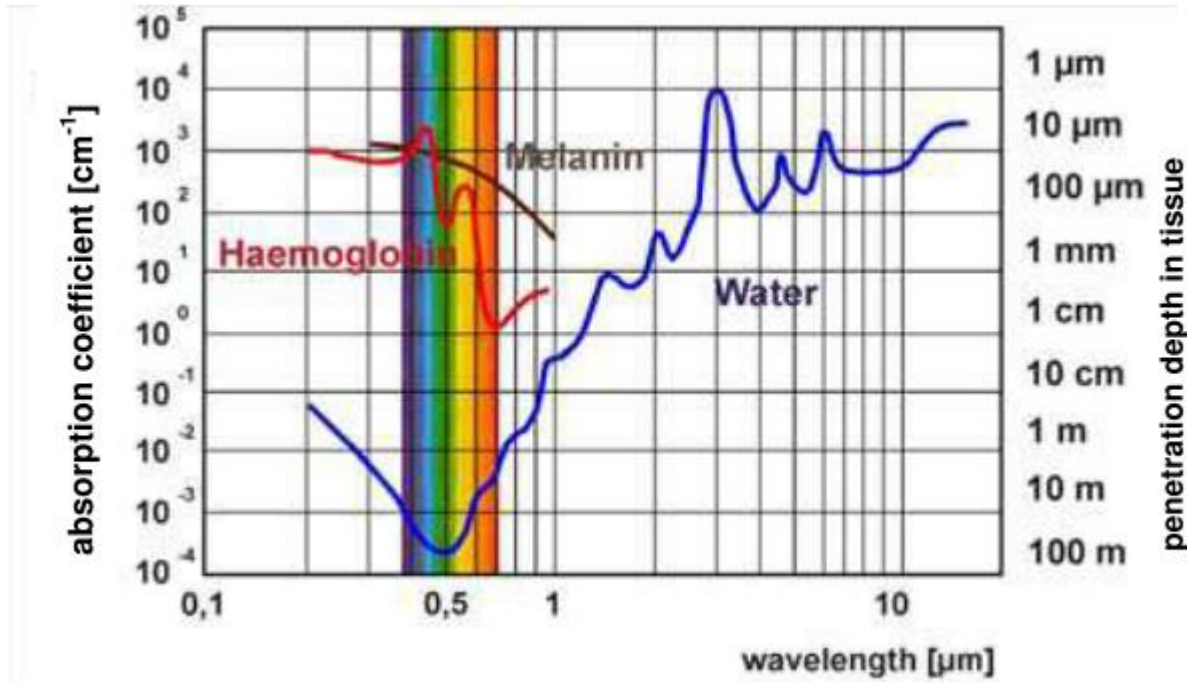


Fig. 3.1: Absorption and penetration depth in water and other biological tissue constituents for different wavelengths [79].

Thulium doped fiber laser (TDFL) can be in continuous wave (CW) in single frequency regime, single transverse mode; it can be pulsed laser with high peak power. Different groups have worked on developing single frequency laser using thulium doped fiber around 2 μm . For instance, a group in Denmark used a single frequency distributed feedback (DFB) thulium doped silica fiber laser at 1735 nm[82]. The laser cavity was about 5 cm, and Ti:sapphire laser was used to pump the gain. With the threshold pump of 59 mW the maximum output power was 1 mW. In 2005, 345 mW single frequency DFB master oscillator power amplifier (MOPA) was demonstrated at 1836 nm [83]. The maximum power was obtained from DFB was 5 mW and then it was amplified

to 345 mW with the pump wavelength at 1565 nm. A 2 cm distributed Bragg reflector (DBR) fiber laser was demonstrated with single-frequency output at 1950 nm and laser linewidth less than 3 kHz [84]. A single-mode Er-doped fiber laser at 1575 nm was used a core-pump source. A high-power single-frequency mode-hop-free fiber DBR laser was developed at 1943 nm with 580 mw signal output[85]. An in-band pump Er/Yb fiber laser at 1565 nm was used in this experiment. a high power all-fiber single frequency Tm-doped fiber amplifier using MOPA with the central wavelength of 1970 nm and maximum output power of 102 W was also developed [86]. The slope efficiency of this setup was about 50% with respect to the absorbed pump power.

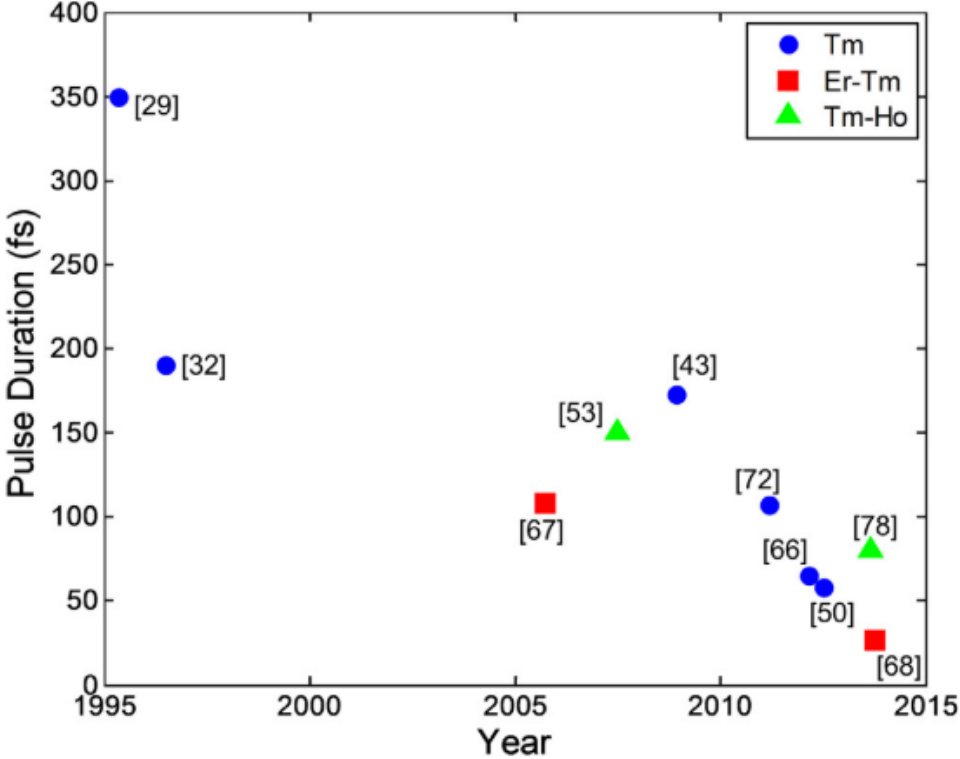


Fig. 3.2: Summary of shortest pulses durations observed over time in mode-locked Tm-doped fiber laser systems[87].

In addition to CW laser, pulsed lasers in 2 μm region using TDFL have been demonstrated. In 2009, all-fiber Q-switched single-frequency laser oscillator operating in the eye-safe region at 1950 nm was developed with pulse repetition rate between tens of hertz to hundreds of kilohertz[88]. Different groups have also demonstrated high power ns pulsed laser using thulium doped fiber laser in 2 μm region[89–91]. Different groups have also worked on thulium doped mode locked fiber in 2 μm region[92–96]. Fig. 3.2 summarizes shortest pulses durations observed over time in mode-locked Tm-doped fiber laser till 2014 [87].

In this chapter we will discuss the spectroscopy of thulium doped silica fiber with the focused on its emission in 2 μm region and then we will demonstrate several watts thulium doped fiber laser operating in CW regime and also we will show microsecond and nanosecond Q-switched fiber laser MOPA using thulium doped silica.

3.2 Spectroscopy of thulium doped silica for mid IR emission

Spectroscopy studies how matter interacts with electromagnetic waves. These days, spectroscopy became a fundamental tool to investigate physical and electronic structure of matter at atomic scale. So, the spectroscopy of rare earth ions has become the backbone of different fields from material design to astronomy. The difference in performances of photonic devices such as slope efficiency of a laser, two photon absorption, refractive index, gain of amplifier, lasing wavelength, saturation intensity, pump wavelength is rooted in the spectroscopic properties of the materials.

Silica glass has usually transmission range of 0.16 to 4 μm as shown in Table 3.1 [17]. Due to high transition temperature of 1175 $^{\circ}\text{C}$, silica glass is a very stable glass and resistant to chemical attack. The maximum phonon energy of silica glass is around 1100 cm^{-1} .

Table 3.1: Basic properties of silica glass[17].

Glass Property	Silica
Transmission range (μm)	0.16-4
Maximum phonon energy(cm^{-1})	1100
Transition temperature (C)	1175
Specific heat (J/(g.K))	0.179
Thermal conductivity (W/(m.K))	1.38
Expansion coefficient ($10^{-6}/\text{K}$)	0.55
Density (g/cm^3)	2.20
Knoop hardness (kg/mm^2)	600
Fracture toughness ($\text{MPam}^{1/2}$)	0.72
Poisson's ratio	0.17
Young's modulus (Gpa)	70
Shear's modulus (Gpa)	31.2
Bulk's modulus (Gpa)	36.7
Refractive index (@ 589 nm)	1.458
Abbe number	68
Zero material dispersion wavelength (μm)	1.3
Nonlinear index (10^{-13} esu)	1
Thermo optics coefficient ($10^{-6}/\text{K}$)	11.9

The energy level diagram of Tm^{3+} doped silica for 2 μm region emission is shown in Fig. 3.3.

The emission transition of ${}^3\text{F}_4 \rightarrow {}^3\text{H}_6$ can emit between 1700 to 2100 nm. In order to populate ${}^3\text{F}_4$

an in-band pumping can be used. The wavelength range for in-band pumping can be from 1500

to 1950 nm. A pumping source operating in 1200 nm region also can be used to excite the ions to 3H_5 and then due to nonradiative transition the 3F_4 level will be populated. Same process can be used by 790 nm pump source but two consecutive nonradiative emission would happen on from 3H_4 to 3H_5 and then to 3F_4 .

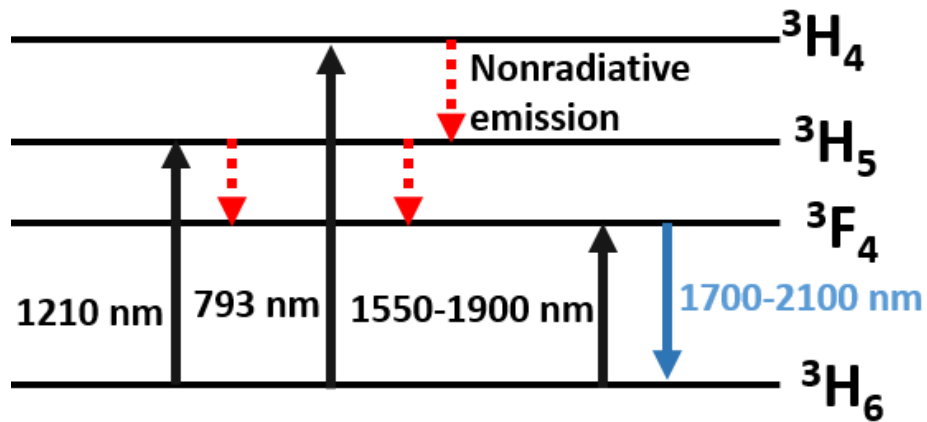


Fig. 3.3: Energy level diagram of Tm^{3+} doped silica for 2 μm region emission.

As it can be seen from Fig. 3.3, the 3F_4 manifold is the first excited state of Tm^{3+} which is 0.74 eV above the ground state. The $^3F_4 \rightarrow ^3H_6$ transition is usually wide emission band from 1.6 to 2.0 μm . The large linewidth of the emission usually means a strong coupling of the rare earth ion to matrix of the glass. The life time of 3F_4 manifold was found to be around 0.42 ms[49]. Which gives a radiative quantum efficiency of (RQE) of around 9%. RQE defined as the ratio of measured lifetime to calculated radiative lifetime by Judd–Ofelt theory. RQE of 3F_4 can be much higher and close to 100% for glasses with lower phonon energy such as ZBLAN. The smaller RQE usually leads to higher threshold pump power. the 3H_5 manifold is the second excited state of Tm^{3+} which is 0.95 eV above the ground state. Since the energy difference between 3H_5 and 3F_4 manifold is about 2250 cm^{-1} , the ions can easily decay from 3H_5 to 3F_4 manifold. As it can be

seen in Fig. 3.4 the peak absorption of ${}^3\text{H}_5$ is not that much higher than the peak absorption of ${}^3\text{F}_4$.

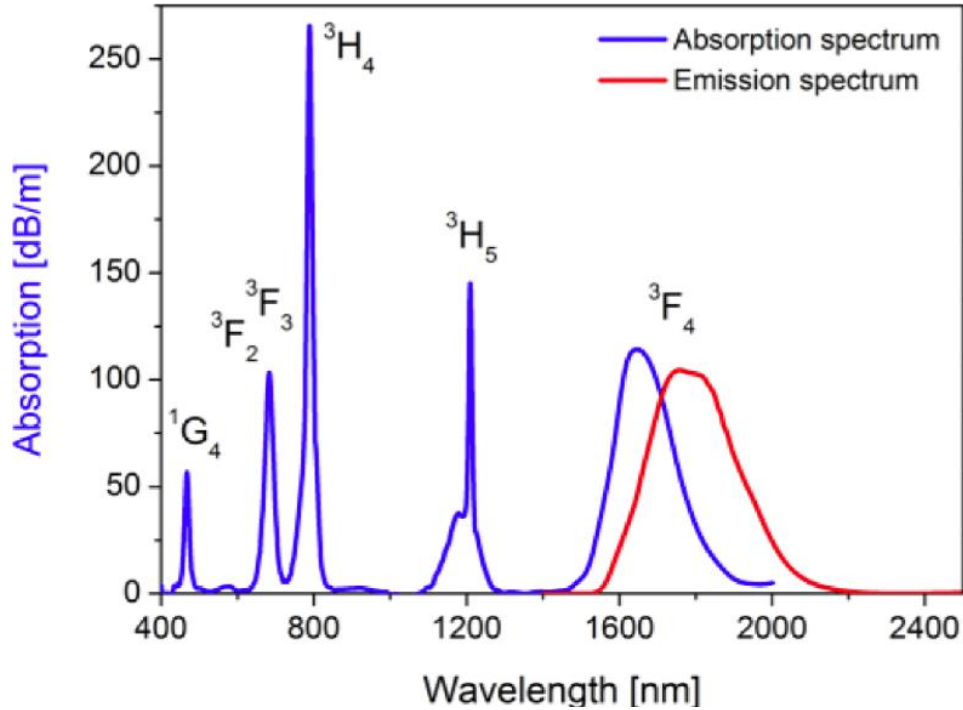


Fig. 3.4: The optical absorption and emission spectra of thulium doped silica fiber[97].

The third excited state of Tm^{3+} doped silica is ${}^3\text{H}_4$ which has the energy level of 1.55 eV with respect to the ground level. As it can be seen in Fig. 3.4, it has the highest absorption in Tm^{3+} doped silica. The lifetime of ${}^3\text{H}_4$ was found to be around 20 μs [49]. There are two advantages to pump the Tm^{3+} doped silica to ${}^3\text{H}_4$ to get ${}^3\text{F}_4 \rightarrow {}^3\text{H}_6$ emission, one is the availability of high pump power around 800 nm, second it can have quantum efficiency of greater than 100% [98], which is due to the cross relaxation as shown in Fig. 3.5. In this process the ion “a” is in some excited state, a part of its energy is transferred to some other ion which in here is ion ”b”, as it was originally in the electronic ground state, and both ions are finally in the upper laser level at ${}^3\text{F}_4$.

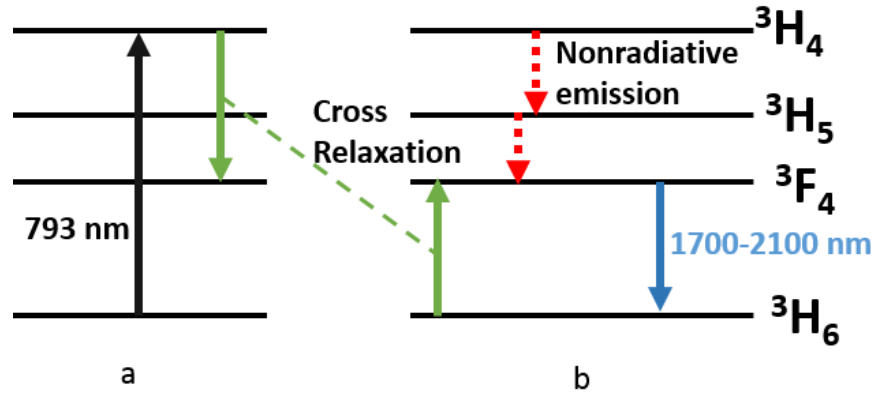


Fig. 3.5: The cross relaxation process between two thulium ions labeled as “a” and “b”.

So in general in order to excite the thulium ions in silica fiber to 3F_4 manifolds, in-band pumping from 1500 to 1950 nm can be used or using a pump source operating in 1200 nm region, and 790 nm pump source can be used to populate the 3F_4 manifolds.

3.3 Experimental results and discussion

Different Tm^{3+} doped silica fiber lasers have been developed in this experiment. Since high power fiber-coupled diode pump laser at 793 is available, two pump diodes at 793 was used as the pump source. Two pump diodes and combiner were installed on a cooling plate which was cooled by chiller using water. The combiner had two input for pump power which multi-mode fibers were used, and one input as signal port which SMF28 fiber was used. The common port was double clad with core diameter of 10 μm .

As shown in Fig. 3.6 Tm -doped fiber laser was built to operate at 1950 nm. 3.5 m Tm -doped silica fiber with a core diameter of 10 μm was used as the gain fiber. A pair of fiber Bragg gratings

(FBGs) were spliced to the gain fiber to form a laser cavity. About 7.5 W stable output at 1950 nm was obtained, but with increasing pump the HR FBG burnt.

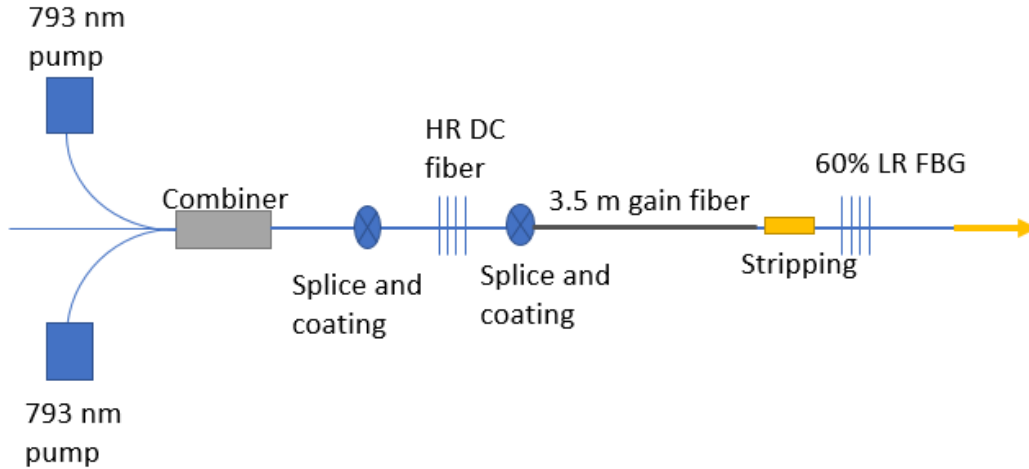


Fig. 3.6: A schematic of laser setup operating at 1950 nm.

Fig. 3.7 shows the output power of the laser as a function of pump power. The efficiency of laser is about 37% and the output was stable up to 25 W input pump power. The maximum obtained signal output was 7.5 W. When the pump increased further the high reflective fiber Bragg grating burnt. The pump threshold of the laser was about 3 W. The lower right inset of Fig. 3.7 shows the laser spectrum output which is around 1949.5 nm with about 0.1 nm full width half maximum (FWHM). In order to get higher signal output, the high reflective fiber Bragg grating needs to be coated in a better quality to reduce the leaking power from outer cladding. Putting a fan on the FBG can also help.

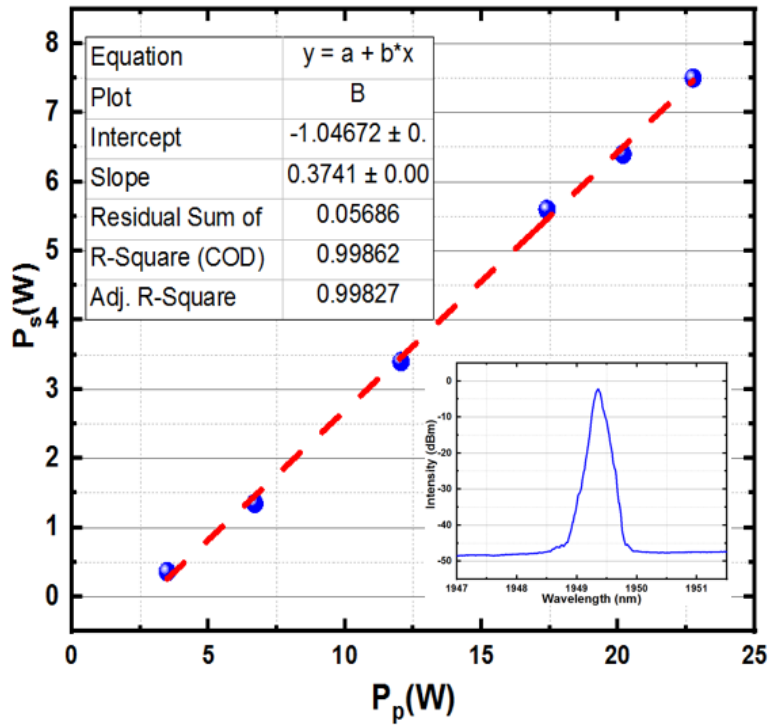


Fig. 3.7: The output signal as a function of pump power. Lower right inset: The spectrum of laser output.

We also examined 1.6 m gain fiber, but the setup was different as shown in Fig. 3.8. The lasing wavelength was 1940 nm and the PR FBG had 10% reflection. The gain fiber was same as the previous experiment purchased from IXblue.

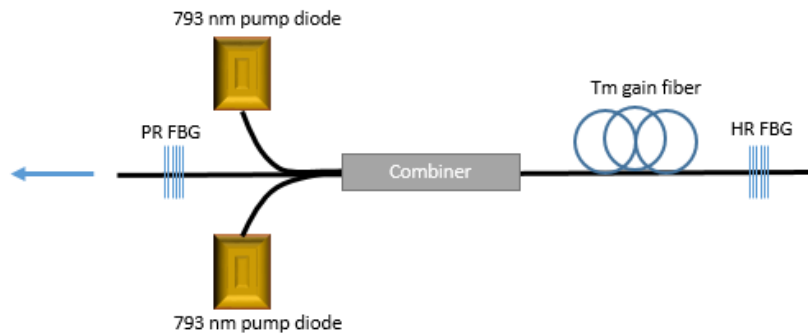


Fig. 3.8: A schematic of laser setup operating at 1940 nm with PR FBG of 10% reflection.

The signal power as a function of incident pump power is shown in Fig. 3.9. The reason we didn't pump it harder was due to the fact that we were testing this setup for Q-switched laser. The slope efficiency was about 35% and the threshold pump power was about 1.16 W. The threshold power was expected to be lower but the PR FBG had 90% transmission which caused higher threshold pump power. The maximum obtained output power was 915 mW. The residual pump power as a function of pump power is shown in inset of Fig. 3.9. As it can be seen at 3320 mW incident pump power the residual pump power was about 400 mW. Which means about 88% of the pump power is absorbed and only 12% residual pump is obtained.

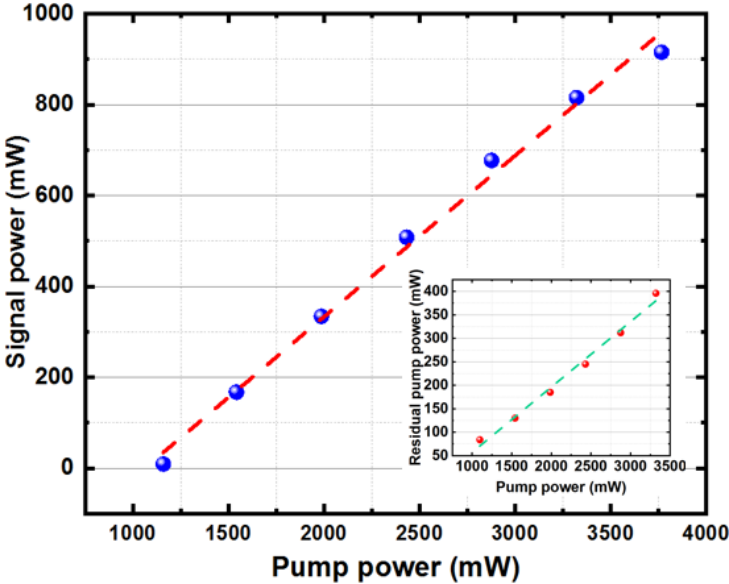


Fig. 3.9: The output signal as a function of pump power for 1.6 m gain. Lower right inset: The residual pump as a function of pump power.

In another experiment, two Q-switched lasers were built with linear cavity design and ring cavity design. The designs are based on active Q-switching using acoustic optical modulator (AOM). The ring cavity setup is shown in Fig. 3.10. 793 nm diode pump was used to pump the 1.6 m gain fiber which was a double clad fiber. After the gain fiber a pump stripping was used to dump the residual

pump in order to protect the AOM. The maximum input power for AOM was 150 mW average power. After removing the residual pump, a 50/50 coupler operating at 1940 nm was used as the output coupler. And finally an AOM was placed after the coupler. At pump power of 2.9 W and pulse with of 500 ns the average power as a function of repetition rate was measured. As shown in Table 3.2.

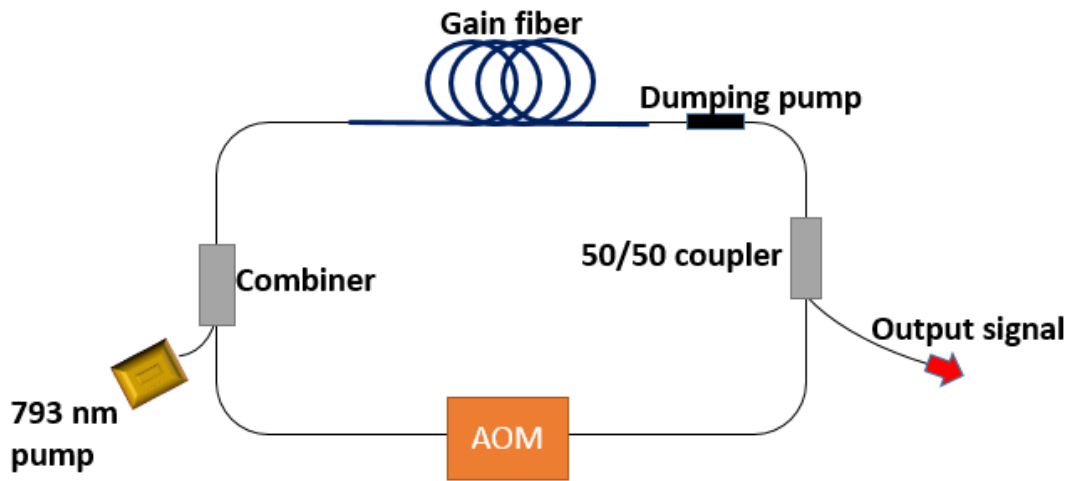


Fig. 3.10: The schematic setup for Q-switched laser ring cavity design.

Table 3.2: signal output as a function of repetition rate.

R (kHz)	P (mW)
100	31
80	20
60	18
40	16.5
20	9.5

The linear cavity setup was also tested. In linear cavity setup the AOM was spliced to the signal port of the combiner. The schematic design of linear cavity is shown in Fig. 3.11 (a). The pair of FBGs were working at 1940 nm. The HR FBG was used after the gain fiber and PR FBG was spliced to the output of AOM. The gain fiber was same as the one used in ring cavity design. Fig. 3.11 (b) shows the average signal power as a function of pump power for the repetition rate of 15 kHz and the pulse width of 50 μ s. a signal output power of 10 mW corresponding to 0.66 μ J was obtained.

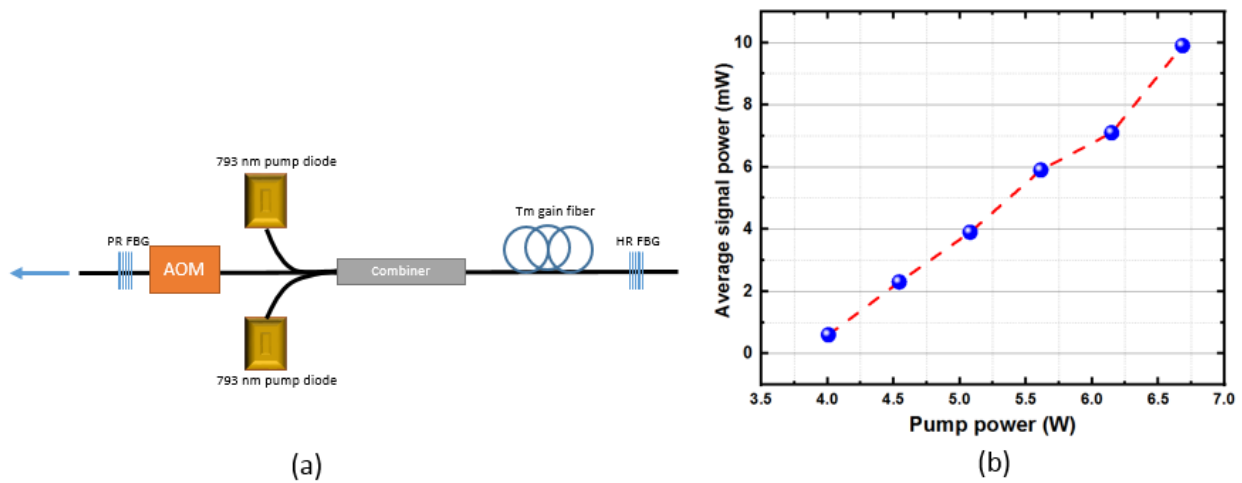


Fig. 3.11: (a) The schematic setup of linear cavity design for Q-switched laser;(b) the average signal output power as a function of pump power.

The output of linear cavity Q-switched laser was amplified with one stage amplifier and a maximum of a few μ J was obtained. Fig. 3.12 shows an example of measuring pulse width and repetition rate of the output signal. The pulse width was 10 μ s and the repetition rate was 10 kHz. In order to measure the pulse width and repetition rate of the signal a biased free space InGaAs detector was used.

In conclusion, in this experiment we were able to demonstrate a thulium doped fiber laser operating in CW regime with several watts output power in 2 μm region. 793 nm high power diode pump was used to pump the gain fiber and the slope efficiency of 35% was obtained. Ring cavity design and linear cavity design of thulium doped fiber Q-switched laser operating in 2 μm region were also demonstrated.

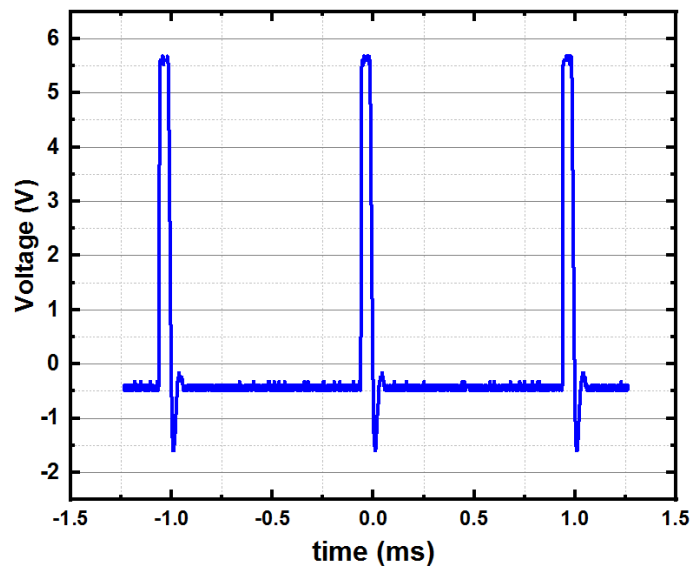


Fig. 3.12: The pulse width and repetition rate of output signal.

Chapter 4 Magneto Optical Properties of Dy³⁺-Doped Glasses

4.1 Introduction

Magneto-optical (MO) materials capable of influencing the light propagation under an applied magnetic field by use of the Faraday effect, magnetic Kerr effect, and magnetic circular dichroism have found a variety of applications ranging from optical switches, isolators, modulators to security encoding and sensing [99–101]. The Faraday effect, in which the polarization plane of a linearly polarized light beam is rotated by the interaction between the incident light and the MO material, has been extensively used for these applications. Faraday effect of a MO material is usually quantified by the Verdet constant V , which is defined as the rotation of the polarization vector for a linearly polarized light beam under a certain longitudinal (along the light propagation direction) magnetic field (usually 1 Tesla) and 1-m optical path length in the MO material. MO materials with large V and low optical absorption are usually needed for the development of optical isolators and circulators, which have been extensively used in optical communication systems and laser systems in the near-infrared. In recent years, there is an increasing demand for MO devices operating at the 2 μm wavelength region, which is atmospheric transparent, eye-safe, and low-scattering and distortion for light propagation. Yttrium iron garnet (YIG) and bismuth-substituted yttrium iron garnet (Bi-YIG) crystals are currently the most prevalent MO materials for 2 μm applications. But their fabrication is time-consuming and cost-intensive. These crystalline materials are birefringent and cannot be used for applications where an isotropic material is required. Therefore, new isotropic MO materials with large V and low optical absorption at 2 μm are in great demand.

Glasses are amorphous, easy to fabricate, and cost-effective, and can be readily made into optical components with desired sizes and shapes and even drawn into optical fibers. Therefore, MO glasses have attracted significant interest and have been investigated for many years. Undoped oxide glasses usually have diamagnetic MO properties and their Verdet constants are relatively small. MO oxide glasses with large Verdet constants can be achieved by incorporating rare-earth dopants including Eu^{3+} , Dy^{3+} , Pr^{3+} , Tb^{3+} and Ce^{3+} [102,103], which are paramagnetic and have large magnetic moments attributed to the electronic transition $4f^n \rightarrow 4f^{n-1} 5d$. However, most of these MO glasses have absorption peaks in the 2 μm wavelength region and thus cannot be used to make low-loss MO devices for 2 μm applications. Ce^{3+} and Dy^{3+} ions are candidates as dopants for MO glasses at 2 μm because they do not have absorption peaks in this wavelength region. However, it is still difficult to make highly Ce^{3+} -doped glasses without producing any Ce^{4+} , which is diamagnetic and reduces the Verdet constant of the glass accordingly [102]. Among the rare earth ions, Dy^{3+} (${}^6\text{H}_{15/2}$) has the largest effective magnetic moment ($\mu_{\text{eff}} = 10.6 \mu_{\text{B}}$) [103]. Large Verdet constants have already been measured with highly Dy^{3+} -doped crystals and ceramics. A Verdet constant of 119 rad/T/m at 635 nm was obtained with a Dy^{3+} -doped aluminum garnet [104]. Most recently, a Verdet constant as high as 297 rad/T/m at 633 nm was achieved with a $(\text{Dy}_{0.9}\text{Y}_{0.05}\text{La}_{0.05})_2\text{O}_3$ ceramic with a Dy doping level of 90 mol. % [105]. Due to its half integer total moment J , the energy levels of Dy^{3+} remain degenerate and thus a large magnetic moment can be obtained even for a low symmetry crystal field environment such as a glass [106]. Several studies have shown that Dy_2O_3 can be a modifier or turn into an exchange coupled Dy^{3+} ion in oxide glasses [106,107], resulting in large Verdet constants. It has been found that Dy^{3+} -doped glass has the second largest V after Tb^{3+} -doped counterpart glass in the visible range [108]. Therefore, Dy^{3+} -doped glasses are quite promising MO materials for the 2 μm wavelength region.

In order to compare Dy³⁺-doped glasses with other paramagnetic glasses, Tb³⁺-doped glasses and Ce³⁺-doped glasses were also fabricated.

4.2 Theory of Faraday rotation

The Faraday effect was discovered by Michael Faraday in 1845. He was trying to look for the effects of magnetic effect on light passing through various materials. Finally, after many unsuccessful trials, he was able to observe that a beam of polarized light can be rotated as it passes through a glass when the direction of magnetic field and light propagation is the same. The effect is known as Faraday rotation or Faraday effect. Later on, Sommerfeld explains that this effect is due to the difference between the refractive index of left circularly (n_-) and right circularly (n_+) polarized light components of light [109]. In his derivation, he considers a simple Lorentzian force and then he calculates the response of oscillators to the applied field. He finds that the difference between refractive index of n_- and n_+ can be written as[110]:

$$n_+ - n_- = \frac{Ne^3}{n\epsilon_0 m_0^2} \frac{B_0 \omega}{(\omega_0^2 - \omega^2)^2} \quad (1)$$

where N is the oscillator density, ω_0^2 is the resonance frequency, e the charge, and m_0 the mass of an oscillator, B_0 is the magnitude of the external magnetic field, ω is the frequency of the optical field, ϵ_0 is the vacuum permittivity, n is the index refraction of medium in the absence of magnetic field.

If a sample with length L that can be treated by Lorentzian equation placed in an external magnetic field B_0 , the difference in the indices leads to a rotation angle[110]:

$$\theta = \frac{\omega}{c} \left(\frac{n_- - n_+}{2} \right) L = \frac{Ne^3 B_0 L}{2nm_0^2 c \epsilon_0} \frac{\omega^2}{(\omega_0^2 - \omega^2)^2} = VLB_0/\mu_0 \quad (2)$$

So then Verdet constant can be written as:

$$V = \frac{Ne^3\mu_0}{2nm_0^2c\epsilon_0} \frac{\omega^2}{(\omega_0^2 - \omega^2)^2} = \frac{e\mu_0}{2m_0c} \omega \frac{dn}{d\omega} \quad (3)$$

It is seen that the Verdet constant is proportional to the dispersion of the medium.

Based on equation (3), the relationship between the Verdet constant and the wavelength of the light for diamagnetic materials can be written as a simplified *Borrelli* equation as[111]:

$$V = \frac{c\lambda^2}{\left(1 - \frac{\lambda^2}{\lambda_0^2}\right)^2} \quad (4)$$

Van Vleck-Hebb derived a relationship between the paramagnetic contribution of the Verdet constant and the magnetic susceptibility which can be written as following for the room temperature operation when electronic dipole transitions are dominated [111]:

$$V = \frac{4\pi^2 N v^2 \mu_{eff}^2}{3chktg\mu_B} \sum_n \frac{C_n}{v^2 - v_n^2} \quad (5)$$

where c , h , k , T , g , μ_B , N , μ_{eff} , v , v_n^2 , C_n , are speed of light, Planck constant, Boltzmann constant, temperature, Lande splitting factor, Bohr magneton number, paramagnetic ion concentration, effective magnetic moment, light frequency, frequency related to the excited state, and transition moments, respectively. Based on the equation, Verdet constant is linearly proportional to the inverse of temperature and, proportional to the paramagnetic ion concentration.

4.3 Glass fabrication and characterization

The Dy³⁺-doped glasses, Tb³⁺-doped glasses and Ce³⁺-doped glasses were made by conventional glass fabrication methods. High purity chemical powders, GeO₂, SiO₂, P₂O₅, B₂O₃, Al₂O₃, Ga₂O₃, and Re₂O₃ (Dy₂O₃, Ce₂O₃, Tb₂O₃) with specific weights according to the composition for making stable glasses, were prepared as the starting materials. The powders were mixed and loaded into a platinum crucible. The crucible was then put in a furnace at a temperature between 1450-1650 °C for a period of 15-48 hours depending on the quantity of the raw materials. During the process, chemical reactions occurred and a glass melt was formed. The crucible was then removed from the furnace and the glass melt was poured into a preheated metal mold and quenched to a glassy solid. Finally, the glass was placed in an oven for annealing at its glass transition temperature for 2-10 hours depending on the volume of the glass and cooled down slowly to room temperature at a rate of 20 °C/hour.

Three different glasses of 20 wt.% Dy³⁺ doped germanate glass, 20 wt.% Ce³⁺ doped germanate phosphate glass, and 25 wt.% Tb³⁺ doped phosphate glass are shown in Fig. 4.1. As it can be seen from the color of the glasses, Tb³⁺ doped phosphate glass is completely transparent for the naked eyes.

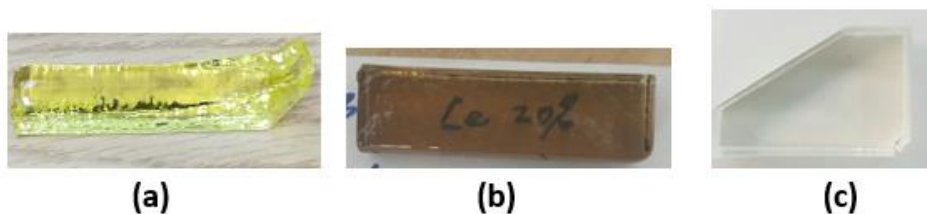


Fig. 4.1: (a) 20 wt.% Dy³⁺ doped germanate glass; (b) 20 wt.% Ce³⁺ doped germanate phosphate glass; (c) 25 wt.% Tb³⁺ doped phosphate glass.

The transmission spectra of the three glasses of 20 wt.% Dy³⁺ doped germanate glass, 20 wt.% Ce³⁺ doped germanate phosphate glass, and 25 wt.% Tb³⁺ doped phosphate glass are shown Fig. 4.2.

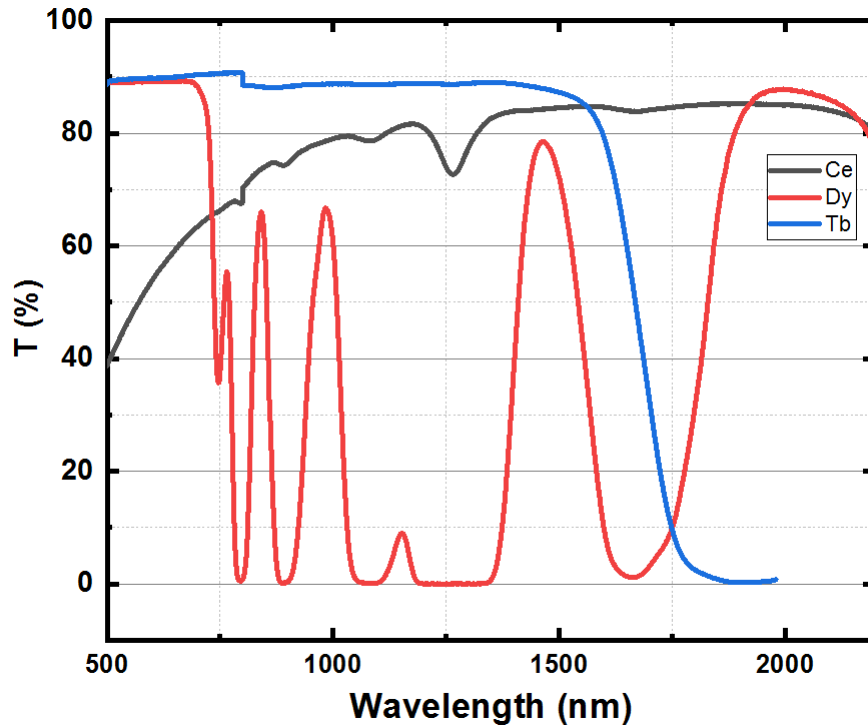


Fig. 4.2: The transmission spectra of the three glasses of 20 wt.% Dy³⁺ doped germanate glass, 20 wt.% Ce³⁺ doped germanate phosphate glass.

Tb³⁺ doped phosphate glass is transparent to 1600 nm. There is a jump at 800 nm due to the changing grating of the Cary 5000 which was used to measure the transmission. Ce³⁺ doped germanate phosphate glass is transparent between 1300 nm to 2200 nm. Dy³⁺ doped germanate glass transparency window is between 1900 nm to 2200 nm.

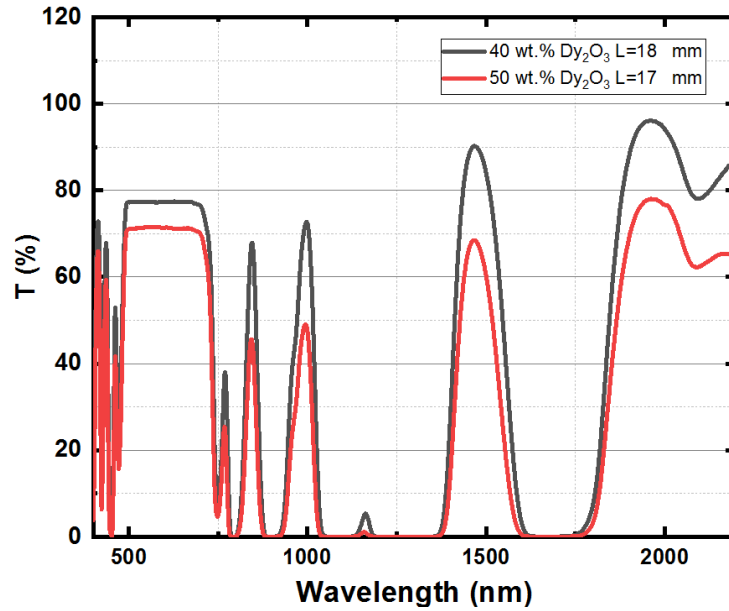


Fig. 4.3: Transmission spectra of 40 and 50 wt.% Dy₂O₃ doped phosphate glass.

We started with germanate glass as the host matrix and the maximum concentration without crystallization was 20 wt.% Dy₂O₃, in order to get to higher concentration the P₂O₅ content of the host matrix increased and 40 and 50 wt.% Dy₂O₃ doped phosphate glass was fabricated as shown in Fig. 4.3. The difference between germanate glass and phosphate glass as host is the dip in phosphate glass around 2100 nm which can't be seen in germanate glass.

A Metricon Model 2010 prism coupler was used to measure the refractive indices of 40 and 50 wt.% Dy₂O₃ doped phosphate glasses at 633, 816, 1305, 1555 nm. Fig. 4.4 shows the refractive indices of Dy³⁺-doped glasses at different wavelengths. It is clear that the refractive index increases with the increased concentration of Dy³⁺.

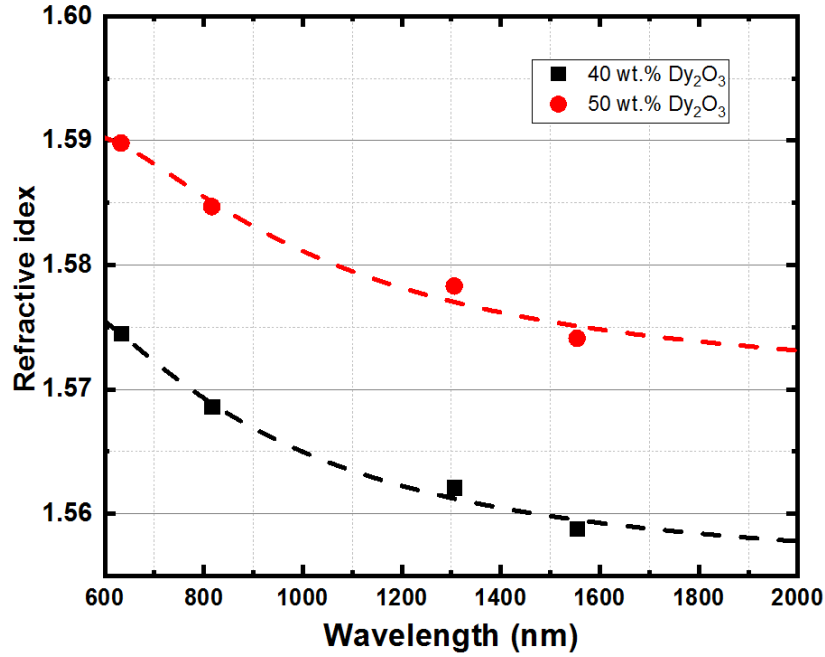


Fig. 4.4: The refractive indices of Dy³⁺-doped phosphate glasses measured at 633, 816, 1305, and 1555 nm and the fitting curves with Cauchy equation.

The refractive index dispersion of a glass can be described by Cauchy equation as following:

$$n = A + \frac{B}{\lambda^2} + \frac{C}{\lambda^4} \quad (1)$$

where, λ is the wavelength of the light, A, B, and C are the coefficients of Cauchy equation, which can be obtained by fitting the experimental data and are shown in Table 4.1.

Table 4.1: The coefficient of Cauchy equation for Dy³⁺-doped phosphate glasses

Wt.%	A	B (10 ⁴)	C (10 ⁹)
40	1.5550	1.1419	-1.45882
50	1.5699	1.3386	-2.18858

In another experiment, the highly Dy³⁺ concentrated in multicomponent glasses were also made by conventional glass fabrication methods. High purity chemical powders, SiO₂, P₂O₅, B₂O₃, Al₂O₃, AlF₃, Ga₂O₃, and Dy₂O₃, with specific weights according to the composition for making stable glasses, were prepared as the starting materials. The powders were mixed and loaded into a platinum crucible. The crucible was then put in a furnace at a temperature between 1450-1650 °C for a period of 15-48 hours depending on the quantity of the raw materials. During the process, chemical reactions occurred and a glass melt was formed. The crucible was then removed from the furnace and the glass melt was poured into a preheated metal mold and quenched to a glassy solid. Finally, the glass was placed in an oven for annealing at its glass transition temperature for 2-10 hours depending on the volume of the glass and cooled down slowly to room temperature at a rate of 20 °C/hour.

Five highly Dy³⁺ concentrated in multicomponent glasses with different Dy₂O₃ wt.% from 40 to 75 were successfully made. The other compositions wt.% varied differently for each Dy glass, Ga₂O₃ (8-15.7 wt.%), P₂O₅ (3.2-7 wt.%), SiO₂ (3.24-7.6 wt.%), B₂O₃ (7.3-13.8 wt.%), Al₂O₃ (2-15.81 wt.%), and AlF₃ (1.14-1.22 wt.%). Five different highly Dy³⁺ concentrated in multi component glasses with Dy₂O₃ concentration of 40 wt.% (Dy40), 50 wt.% (Dy50), 60 wt.% (Dy60), 65 wt.% (Dy65), and 75 wt.% (Dy75) were made. The ion concentrations of the five Dy³⁺-doped glasses are $5.5 \times 10^{27} \text{ m}^{-3}$ (Dy40), $7.3 \times 10^{27} \text{ m}^{-3}$ (Dy50), $9.4 \times 10^{27} \text{ m}^{-3}$ (Dy60), $1.26 \times 10^{28} \text{ m}^{-3}$ (Dy65), and $1.52 \times 10^{28} \text{ m}^{-3}$ (Dy75), respectively.

All the five Dy³⁺-doped glasses were cut, polished and prepared for optical transmission measurements. The prepared samples were cut to the thicknesses of 3 to 5 mm with both sides polished. The optical transmission spectra of all five samples are shown in Fig. 4.5. Clearly, the

Dy³⁺-doped glasses have high transmission around the 2 μm wavelength region. It should be noted that the Fresnel reflections of the glasses are included in the transmission spectra.

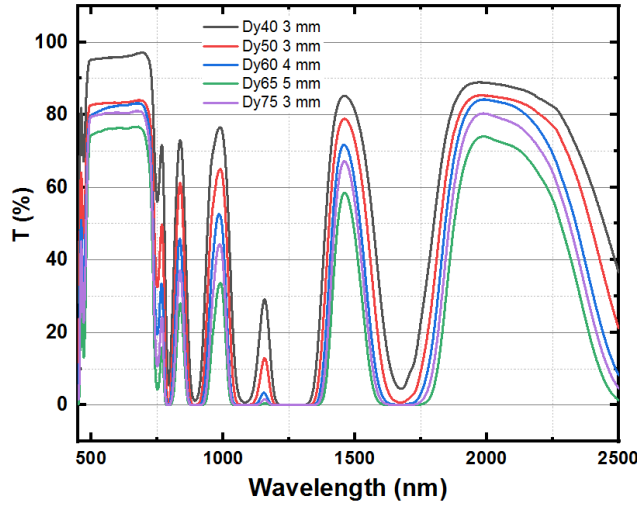


Fig. 4.5: Optical transmission spectra of Dy³⁺-doped borate glass samples with different concentrations.

Fig. 4.6 shows the X-ray diffraction (XRD) measurement result of the Dy75 glass at room temperature. The broad diffraction with no peaks associated with any crystalline phase verifies the amorphous nature of Dy75.

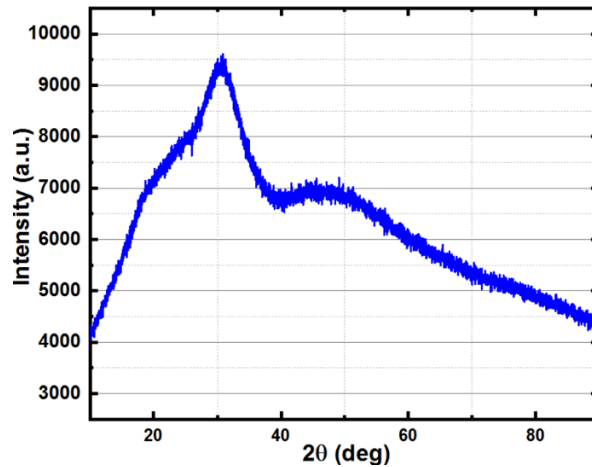


Fig. 4.6: XRD measurement result for the Dy75 glass.

Again, a Metricon Model 2010 prism coupler was used to measure the refractive indices of all 5 samples (Dy40, Dy50, Dy60, Dy65, Dy75) at 633, 816, 1305, 1555 nm. Fig. 4.7 shows the refractive indices of Dy³⁺-doped glasses at different wavelengths. It is clear that the refractive index increases with the increased concentration of Dy³⁺. The refractive index dispersion of a glass can be described by Cauchy equation. A, B, and C the coefficients of Cauchy equation, which can be obtained by fitting the experimental data and are shown in Table 4.2.

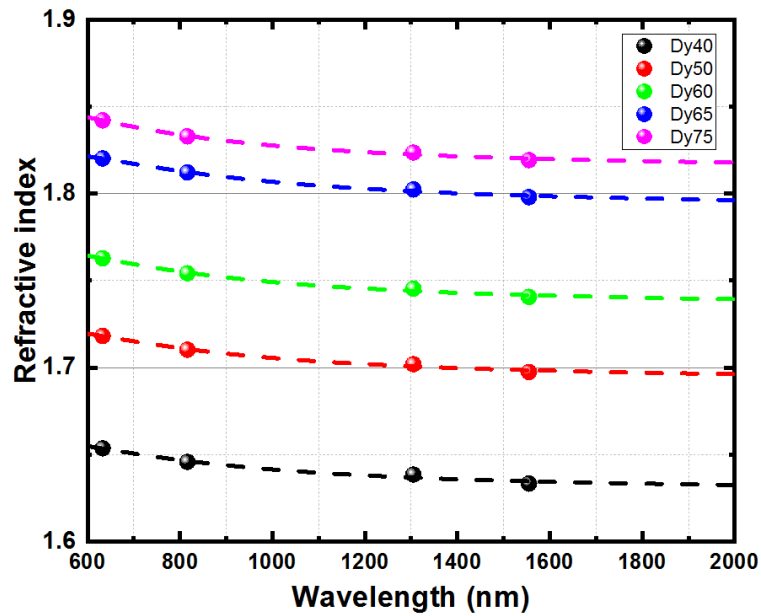


Fig. 4.7: The refractive indices of Dy³⁺-doped borate glasses measured at 633, 816, 1305, and 1555 nm and the fitting curves with Cauchy equation.

Table 4.2: Coefficients of the Cauchy equation for Dy³⁺-doped borate glasses

Samples	A	B (10 ⁴)	C (10 ⁹)
Dy40	1.6290	1.4030	-1.7133
Dy50	1.6926	1.4675	-1.8062
Dy60	1.7355	1.5420	-1.8202
Dy65	1.7922	1.6889	-2.2877
Dy75	1.8142	1.4961	-1.5344

The refractive indices of the Dy³⁺-doped borate glasses as a function of Dy³⁺ concentration at 633, 816, 1305, 1555 nm are plotted in Fig. 4.8. The refractive indices increase linearly with the increased Dy³⁺ concentration for all the four wavelengths and their slopes were found to be close, ranging from 0.00190 to 0.00187, which were obtained by fitting the experimental data to line.

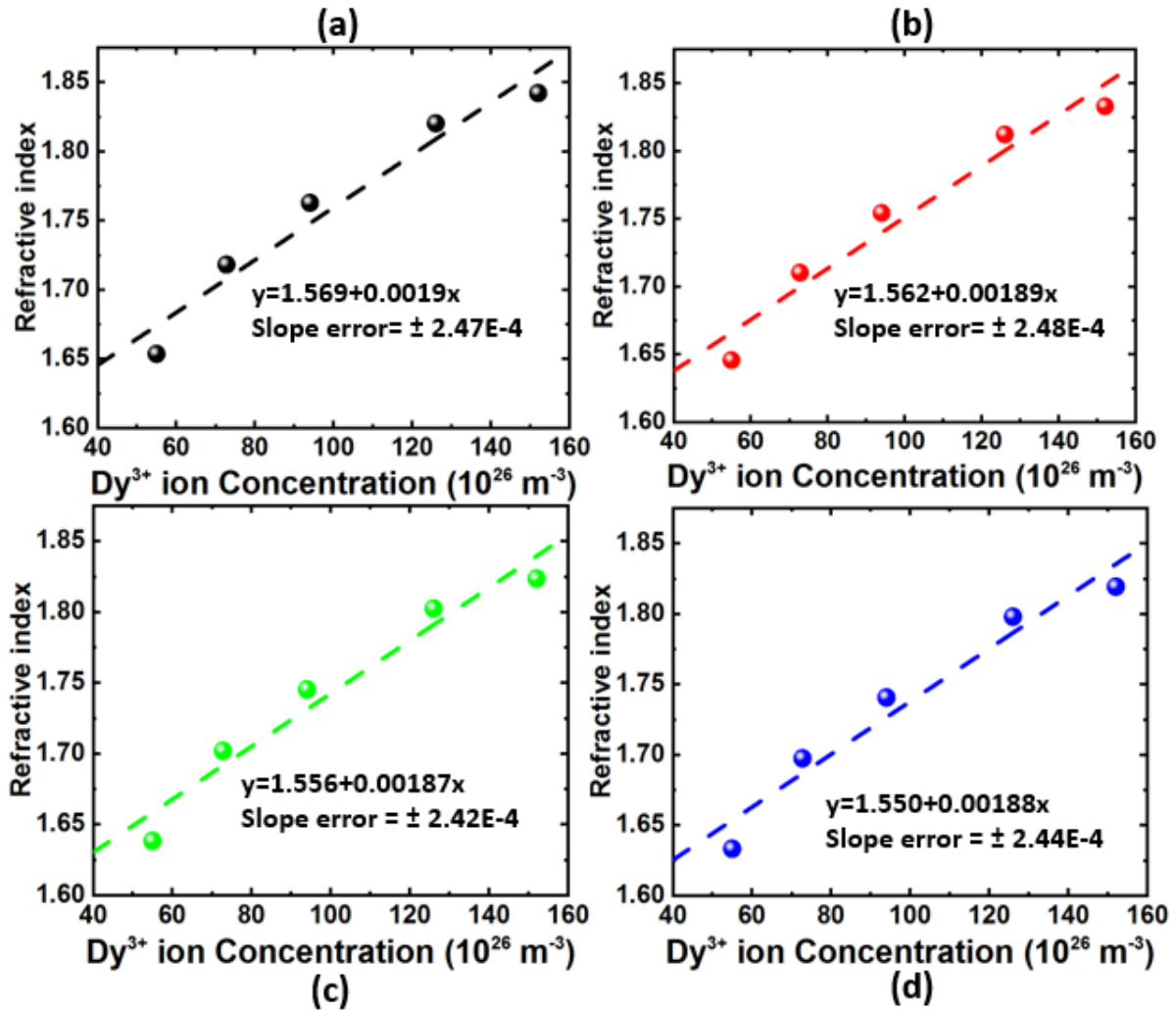


Fig. 4.8: The refractive indices of the Dy³⁺-doped borate glasses as a function of Dy³⁺ concentration at (a) 633 nm; (b) 816 nm; (c) 1305 nm; (d) 1555 nm.

4.4 Experiment, result and discussion

The Verdet constants of the three glass samples were measured using the experimental setup depicted in Fig. 4.9 which consists of a light source, a Glan-Thompson (GT) polarizer, an achromatic half wave plate, a solenoid, a Wollaston polarizer, and two photodetectors to measure the power of the S-polarized and P-polarized light. Linearly polarized light with a polarization extinction ratio of more 30 dB is achieved with a GT polarizer. The plane of the polarized light can be adjusted by a half-wave ($\lambda/2$) plate so that it is at an angle of 45° as the light goes through the MO glass in the absence of a magnetic field and arrives at the Wollaston polarizer, which can separate the S and P polarized light equally. When a magnetic field is applied to the MO glass by the solenoid, the plane of the polarized light rotates. The rotation angle can be calculated from the power of S and P polarized light measured by the two photodetectors. The measurement resolution of the setup for Faraday rotation was higher than 0.01° . The Verdet constant can be calculated from the change in rotation angle of the linearly polarized light, the applied magnetic field, and the glass length with following equation.

$$\theta = V * H \quad (6)$$

$$H = \int B \, dz \quad (7)$$

Where θ is rotated angle, V is Verdet constant and H is defined as the integration of magnetic flux over the length of the sample.

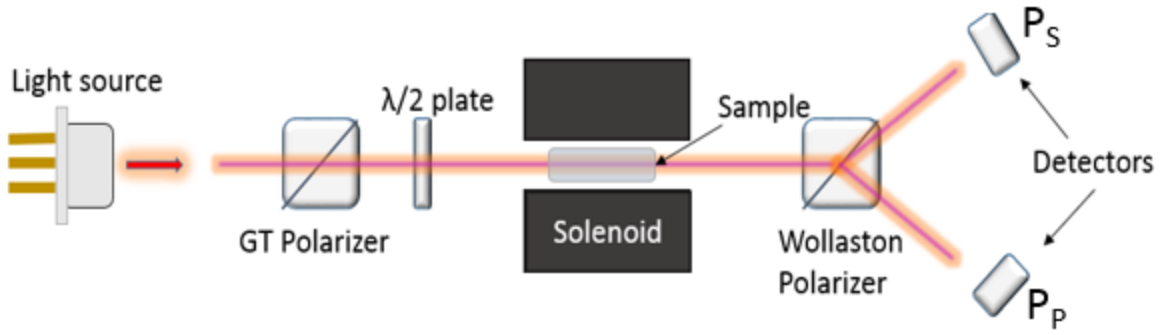


Fig. 4.9: The schematic of the experimental setup for the Verdet constant measurement.

To make it clearer how to find θ , the following equations were used:

$$P_{\text{tot}} = P_s \cos^2 \theta \quad (8)$$

$$P_{\text{tot}} = P_p \sin^2 \theta \quad (9)$$

$$\theta = \tan^{-1} \sqrt{\frac{P_s}{P_p}} \quad (10)$$

Where P_{tot} , P_s , and P_p are the total power, the power of S polarized light, and the power of P polarized light respectively. The Wollaston polarizer separates the two orthogonal linearly polarized lights denoted as P_s , and P_p . Then two detectors measure their powers simultaneously.

Fig. 4.10 shows the Verdet constant measurement at 976 nm for 20 wt.% Ce^{3+} doped germanate-phosphate. The slope of the fitted line gives the Verdet constant.

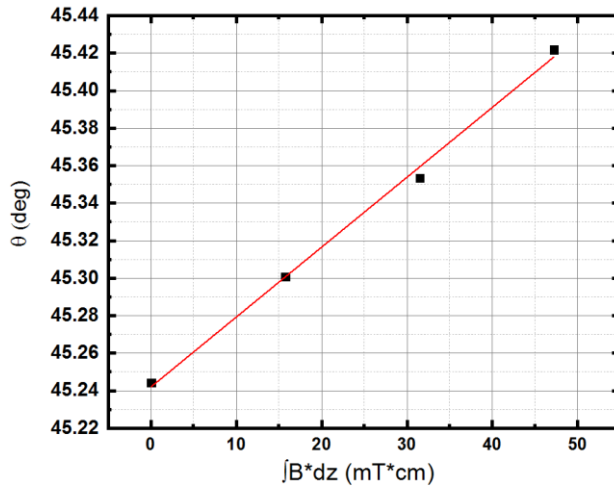


Fig. 4.10: Verdet constant measurement for 20 wt.% Ce doped germanate-phosphate glass at 976 nm.

The Verdet constant of 20 wt.% Dy^{3+} doped germanate glass, 20 wt.% Ce^{3+} doped germanate phosphate glass, and 25 wt.% Tb^{3+} doped phosphate glass were found to be -7.85 rad/T/m, -6.80 rad/T/m, and -12.03 rad/T/m respectively. The Verdet constant of Tb^{3+} doped phosphate glass is almost two times greater than Ce^{3+} doped germanate phosphate glass and significantly higher than Dy^{3+} doped germanate glass. But since the Tb^{3+} is not transmitted in 2 μm , it can't be used for optical isolator and circulator in this wavelength area. Comparing Ce^{3+} and Dy^{3+} with the same weight percent, shows that Dy^{3+} doped glass has higher Verdet constant.

The Verdet constant of 25 wt.% Tb^{3+} doped phosphate glass was measured at 478 nm, 633 nm, 976 nm, and 1480 nm. According to the Van Vleck-Hebb single oscillator model for the MO activity of paramagnetic rare earth ions, the Verdet constant can be expressed as below:

$$V = \frac{A}{\lambda^2 - \lambda_0^2} \quad (11)$$

Where, A is a wavelength independent constant, and λ_0 is the effective transition wavelength of the rare earth ion.

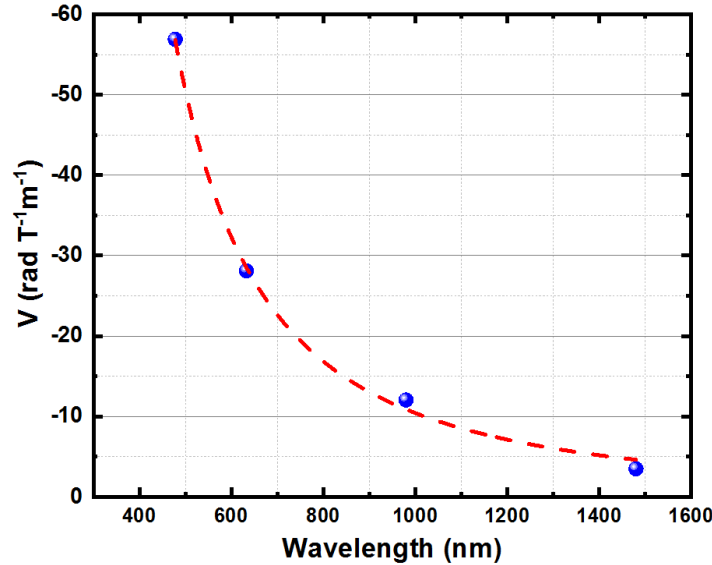


Fig. 4.11: The Verdet constant of Tb^{3+} doped phosphate glass at different wavelengths. Fitted curve is based on Van Vleck-Hebb single oscillator model.

Based on the Van Vleck-Hebb single oscillator model the effective transition wavelength was found to be 235 nm, which is in the same range as other works have reported[112].

The Verdet constants of the Dy^{3+} -doped glasses with different concentrations were measured at 478, 633, 976, 1480, and 1950 nm and are shown in Fig. 4.12. **Error! Reference source not found.** It is clear that the Verdet constants increase with increased concentration of Dy^{3+} , which is due to the fact that V is proportional to paramagnetic susceptibility, which is linearly proportional to the ion concentration. The Verdet constants at all five wavelengths show a linear behavior as a function of Dy^{3+} concentration. The R^2 of linear fits were found to be between 0.99 to 0.98.

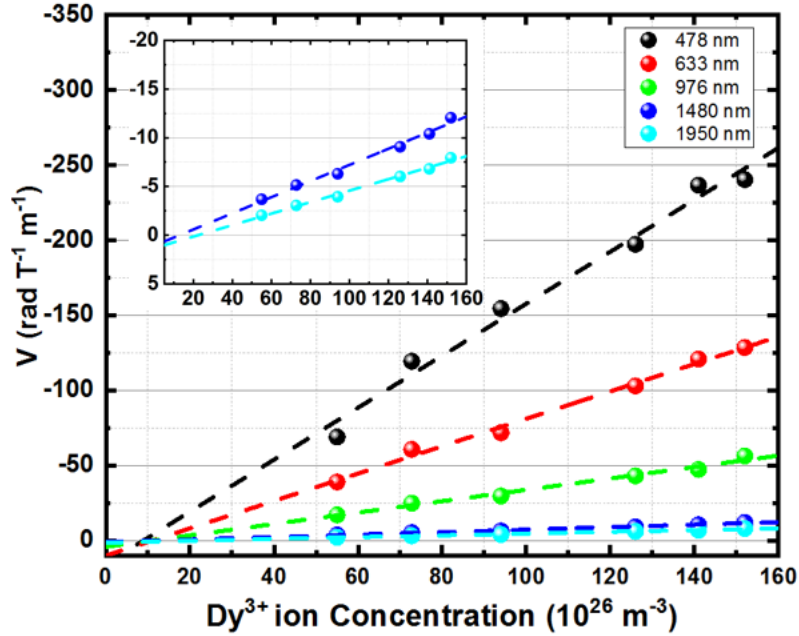


Fig. 4.12: Verdet constants of the Dy³⁺-doped borate glasses with different concentrations measured at 478, 633, 976, 1480, and 1950 nm. Inset shows the results at 1480 and 1950 nm in a small scale.

The Van Vleck-Hebb single oscillator model for the MO activity of paramagnetic rare earth ions can be written in terms of the inverse of the Verdet constant as a function of λ^2 :

$$\frac{1}{V} = a(\lambda^2 - \lambda_0^2) \quad (12)$$

Here, a is a wavelength independent constant, and λ_0 is the effective transition wavelength of the rare earth ion. The inverse of the Verdet constant as a function of λ^2 for the Dy40, Dy50, Dy60, Dy65, and Dy75 is plotted in Fig. 4.13. The experimental results are in good agreement with the Van Vleck-Hebb model in the visible and short-wave near-infrared. As the wavelength enters the long-wave near-infrared, the reciprocal of the measured Verdet constant no longer follows a linear increase with λ^2 . Similar behavior has also been observed in several other MO materials including Dy³⁺-doped ceramic, terbium gallium garnet (TGG), terbium scandium aluminum

garnet crystals (TSAG), and cerium fluoride (CeF₃)[105,113,114].. Therefore, the Van Vleck-Hebbs single-oscillator model is only valid over a certain short wavelength range and becomes inaccurate for longer wavelengths, as expected for a single oscillator model.

The effective transition wavelength λ_0 and the constant a for the Dy³⁺-doped glasses can be obtained by fitting the experimental results at the visible and short-wave near-IR with the Van Vleck-Hebb single oscillator model as shown in Fig. 4.13. The effective transition wavelength was found to be $\lambda_0 = 178$ nm. The λ_0 of the single-oscillator model for the paramagnetic rare earth ions is related to $4f^n \rightarrow 4f^{n-1} 5d$ and could vary slightly in different host materials. For example, the transition wavelength of Dy³⁺ in CaF₂ crystal is 170 nm [115], those of Dy³⁺: LiYF₄, Dy³⁺: YF₃, and Dy³⁺: LaFS are 191 nm, 154 nm, and 154 nm, respectively [116]. The a coefficients were found to be -0.06495, -0.04381, -0.03678, -0.02543, and -0.01963 (T·m)/(rad· μm^2), for Dy40, Dy50, Dy60, Dy65, Dy75, respectively with the R² of 0.99 for all five samples, within the range of linear behavior. It is clear that the a coefficient decreases as the concentration increases.

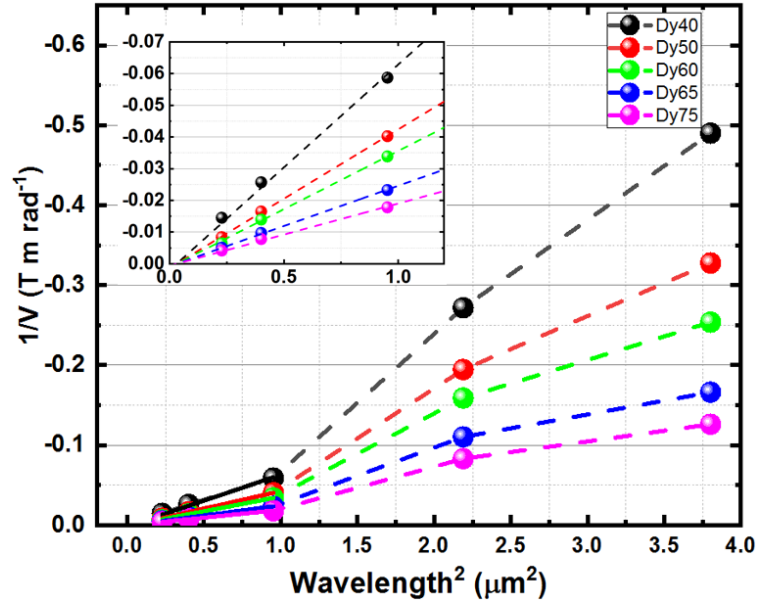


Fig. 4.13: Inverse of the Verdet constant as a function of squared wavelength for Dy40, Dy50, Dy60, Dy65 and Dy75. Inset shows the experimental data and fitted lines at a squared wavelength range of 0-1 μm^2 .

The Verdet constants of Dy40, Dy50, Dy60, Dy65, and Dy75 at 478nm, 633 nm, 976 nm, 1480nm, and 1950 nm is shown Fig. 4.14. The Verdet constants of Dy75 at 478nm, 633 nm, 976 nm, 1480nm, and 1950 nm were found to be about -240 rad/T/m, -128 rad/T/m, -56 rad/T/m, -12 rad/T/m, and -8 rad/T/m respectively.

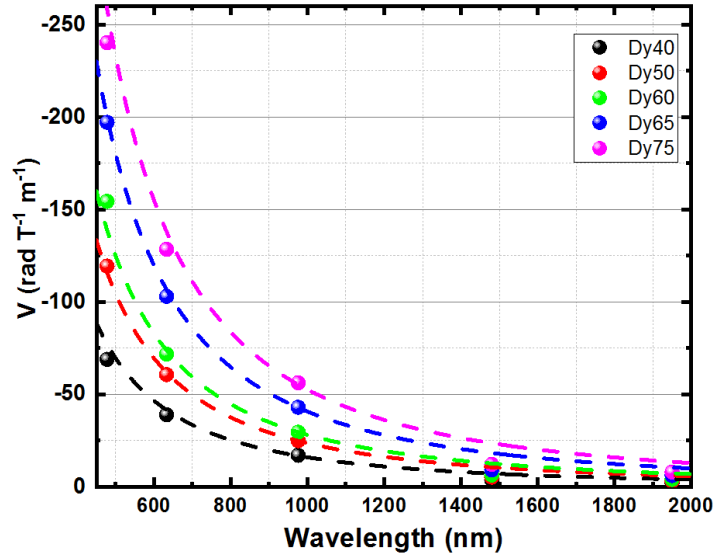


Fig. 4.14: The Verdet constants of Dy40, Dy50, Dy60, Dy65, and Dy75 at 478nm, 633 nm, 976 nm, 1480nm, and 1950 nm.

The Verdet constants of 40 and 50 wt.% Dy_2O_3 doped phosphate glasses are also shown in Fig. 4.15. The Verdet constant of 40 wt.% Dy_2O_3 doped phosphate at 478 nm is about -75 rad/T/m

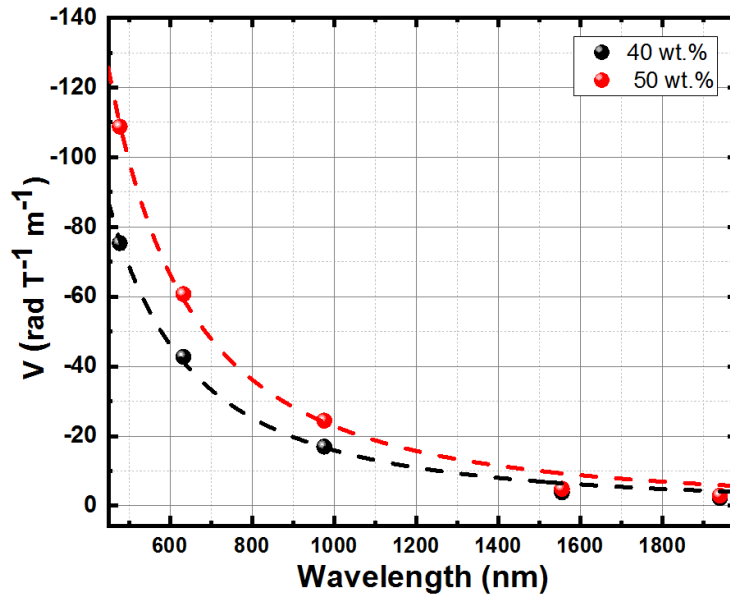


Fig. 4.15: The Verdet constants of 40 and 50 wt.% Dy_2O_3 doped phosphate glasses at different wavelengths.

In conclusion, highly Dy³⁺-doped multicomponent glasses were fabricated and their magneto-optical properties were studied. The refractive index measurement results indicate that the refractive index increases linearly with the increased Dy₂O₃ concentration. It was found that the measured Verdet constants of Dy³⁺-doped glasses are in a good agreement with the Van Vleck-Hebb model in the visible and short-wave near IR region and are smaller than the modeling results at longer wavelengths. Nevertheless, a Verdet constant as high as -7.94 rad/T/m at 1950 nm was measured with a 75 wt.% Dy³⁺ doped borate glass which is the highest number reported for a paramagnetic glass at this wavelength. Our experimental results show that highly Dy³⁺-doped oxide glasses are promising amorphous MO materials in the 2 μm wavelength region.

Chapter 5 Magneto Optical Properties of New Chalcogenide Glasses

5.1 Introduction

As it was discussed in the previous chapter, Magneto-Optical (MO) materials have attracted a lot of attention due to their extensive applications in optical switches, isolators, circulators, modulators, security encoding and sensing components [99,101,117]. In particular, optical isolators and circulators are highly needed in optical systems to protect upstream devices from the influence of the backward propagated light or force the light to propagate unidirectionally [118].

Generally, MO materials can be categorized into diamagnetic materials and paramagnetic materials. Rare-earth doped glasses are paramagnetic materials, which are highly temperature dependent[119] and thus cannot work steadily and consistently in a harsh environment. High Verdet constant of a paramagnetic glass can generally be achieved with increasing the doping concentration of rare-earth elements. But it also leads to deterioration in the chemical stability and optical transmittance. Undoped glasses are diamagnetic materials, which usually have a very low temperature dependence [119]. Oxide glasses have been extensively used in the visible and near-infrared (IR) wavelength regions and their MO properties have also been studied. However, the Verdet constants of oxide glasses are usually low. For example, silica glass has a Verdet constant of 57 deg/T/m in 1064 nm[120] and even for zinc-tellurite glass, V is about 570 deg/T/m at 1 μm [121]. Moreover, the short multi-phonon IR absorption of most oxide glasses also limit their applications in the mid-IR. Compared to oxide glasses, chalcogenide glasses have much longer multi-phonon IR absorption edge and have been made into optical components and optical fibers for a variety of mid-IR applications. Due to their large refractive index dispersion,

chalcogenide glasses also exhibit attractive MO properties. For instance, the Verdet constant of $\text{Ge}_{33}\text{As}_{12}\text{Se}_{55}$ was measured to be 806 deg/T/m at 1550 nm and that of $75\text{GeS}_2\cdot 25\text{Ga}_2\text{S}_3$ was measured to be 831 deg/T/m at 1340 nm [122,123]. Both of them are much larger than that of zinc-tellurite glass at the two wavelengths. By incorporating some large atoms to increase the polarizability, Verdet constants of 1080 deg/T/m and 1197 deg/T/m at 1319 nm were measured in $80\text{GeS}_2\cdot 20\text{Sb}_2\text{S}_3$ and $60\text{GeS}_2\cdot 15\text{In}_2\text{S}_3\cdot 25\text{PbI}_2$, respectively [124,125]. Therefore, a chalcogenide glass with improved MO properties in the mid-IR may be synthesized by introducing large atoms that can lead to high polarizability and long absorption edges. Here, we present the MO properties of $\text{Te}_{20}\text{As}_{30}\text{Se}_{50}$, which has a multi-phonon IR absorption edge of 18 μm and a bandgap short-wavelength absorption edge of 1200 nm. Compared to the other chalcogenide glasses, such as $\text{Ge}_{10}\text{Se}_{90}$, and $\text{Ge}_{25}\text{As}_{15}\text{S}_{60}$, $\text{Te}_{20}\text{As}_{30}\text{Se}_{50}$ glass has much higher Verdet constant at near-IR and mid-IR wavelength due to its smaller electronic bandgap. Verdet constants of 1300 deg/T/m and 870 deg/T/m were measured at 1555 nm and 1950 nm, respectively, which are the highest reported Verdet constants of diamagnetic materials in the mid-IR, to the best of our knowledge. The Figure of Merit (FOM) of the $\text{Te}_{20}\text{As}_{30}\text{Se}_{50}$ was measured to be more than 500 deg/T at 1950 nm, which makes it a promising material for MO applications.

5.2 Glass preparation and experimental setup

Glasses from the Te-As-Se [126], Ge-Se [127] and Ge-As-S [128] systems were selected due to their technological relevance for the production of advanced infrared optics such as single mode fibers, non-linear devices or supercontinuum generation. Specific compositions were selected for their excellent glass-forming properties and potential for very low loss fiber fabrication [129]. Three chalcogenide glass samples were synthesized by the melting quench method starting from high purity raw elements Ge (5N),

As (6N), S (5N), Se (5N) and Te (5N). Stoichiometric amounts of different glass compositions were weighed in a glove box under argon and introduced in silica tube under vacuum (10^{-6} mbar) before sealing the ampoules. The melts were homogenized in a rocking furnace for 10 hours between 800°C–850°C and the temperature was subsequently lowered to 600–650°C in 2 hours before quenching the ampoules in water at room temperature. The ampoules were then readily introduced in an annealing oven preheated at 10°C below the glass transition temperature (T_g) for 5 hours, then the ampoules were slowly cooled down to room temperature at 0.5°C/min.

The optical near-IR and IR transmission of the three glasses were measured at room temperature using a Cary 5000 UV-Vis-NIR Spectrometer and a Bruker Tensor 27 FTIR spectrometer, respectively. Fig. 5.1 shows the optical transmission loss spectra of $\text{Te}_{20}\text{As}_{30}\text{Se}_{50}$, $\text{Ge}_{10}\text{Se}_{90}$, and $\text{Ge}_{25}\text{As}_{15}\text{S}_{60}$, which were calculated from the measured optical transmission spectra of the glass samples with different lengths.

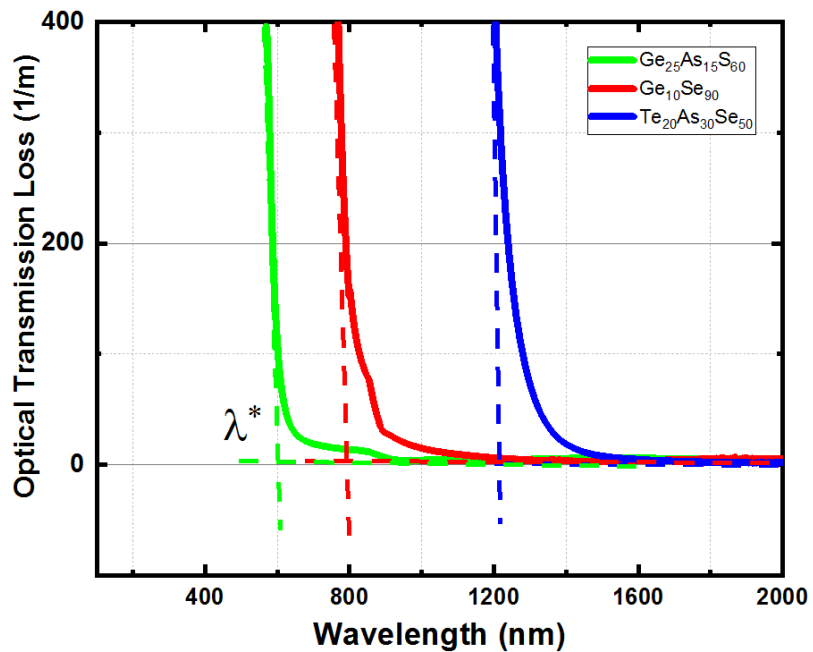


Fig. 5.1: Optical transmission loss spectra of $\text{Te}_{20}\text{As}_{30}\text{Se}_{50}$, $\text{Ge}_{10}\text{Se}_{90}$, and $\text{Ge}_{25}\text{As}_{15}\text{S}_{60}$. The crossing point of two dashed lines show the bandgap absorption edge.

All three glasses have a low absorption in the region near 2 μm . The bandgap absorption edge, λ^* , of a glass is related to the energy gap between the valence band and the conduction band and is determined by the crossing point of the two tangent dashed lines, as shown in Fig. 5.1. The bandgap absorption edges of $\text{Te}_{20}\text{As}_{30}\text{Se}_{50}$, $\text{Ge}_{10}\text{Se}_{90}$, and $\text{Ge}_{25}\text{As}_{15}\text{S}_{60}$ were found to be 1200, 780, and 592 nm, respectively. Clearly, $\text{Te}_{20}\text{As}_{30}\text{Se}_{50}$ glass has a much longer bandgap absorption edge than $\text{Ge}_{10}\text{Se}_{90}$, and $\text{Ge}_{25}\text{As}_{15}\text{S}_{60}$ due to the large tellurium atom.

Fig. 5.2 shows the IR transmission spectra of all three glasses from 1 μm to 20 μm . The transparency window of $\text{Te}_{20}\text{As}_{30}\text{Se}_{50}$ is extended up to 18 μm , while that of $\text{Ge}_{10}\text{Se}_{90}$ and $\text{Ge}_{25}\text{As}_{15}\text{S}_{60}$ is only extended up to 16 μm and 11 μm , respectively. The longer IR absorption edge of $\text{Te}_{20}\text{As}_{30}\text{Se}_{50}$ is due to the heavy atom of tellurium.

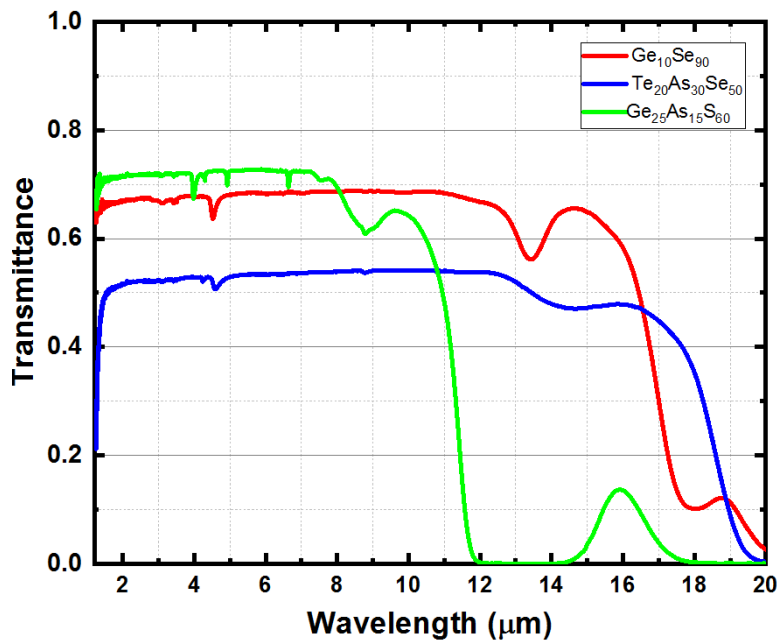


Fig. 5.2: IR transmission spectra of $\text{Te}_{20}\text{As}_{30}\text{Se}_{50}$, $\text{Ge}_{10}\text{Se}_{90}$, and $\text{Ge}_{25}\text{As}_{15}\text{S}_{60}$.

The Verdet constants of the three glass samples were measured using the experimental setup depicted in Fig. 5.3 which consists of a light source, a Glan-Thompson (GT) polarizer, an

achromatic half wave plate, a solenoid, a Wollaston polarizer, and two photodetectors to measure the power of the S-polarized and P-polarized light. Linearly polarized light with a polarization extinction ratio of more 30 dB is achieved with a GT polarizer. The plane of the polarized light can be adjusted by a half-wave ($\lambda/2$) plate so that it is at an angle of 45° as the light goes through the MO glass in the absence of a magnetic field and arrives at the Wollaston polarizer, which can separate the S and P polarized light equally. When a magnetic field is applied to the MO glass by the solenoid, the plane of the polarized light rotates. The rotation angle can be calculated from the power of S and P polarized light measured by the two photodetectors. The measurement resolution of the setup for Faraday rotation was higher than 0.01° . The Verdet constant can be calculated from the change in rotation angle of the linearly polarized light, the applied magnetic field, and the glass length with following equation.

$$V = \frac{\theta}{BL} \quad (1)$$

Where, θ is the angle of the linearly polarized light rotated by the solenoid, B is the magnetic flux of the solenoid, and L is the glass length.

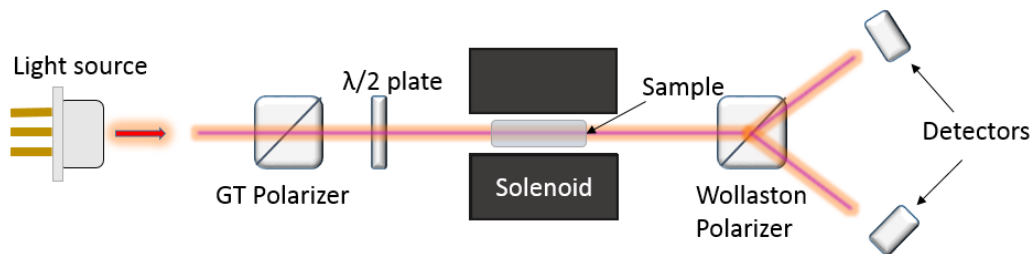


Fig. 5.3: The schematic setup for Verdet constant measurement.

5.3 Result and discussion

The Verdet constants of the three glasses were measured at 1240, 1476, 1555, and 1950 nm and are shown in Fig. 5.4. Clearly, compared to $\text{Ge}_{25}\text{As}_{15}\text{S}_{60}$, and $\text{Ge}_{10}\text{Se}_{90}$ glasses, $\text{Te}_{20}\text{As}_{30}\text{Se}_{50}$ glass has much larger Verdet constant due to the longer bandgap absorption edge. Based on the model of single oscillator with a narrow band resonance wavelength, the wavelength dependence of Verdet constant can be written as a simplified *Borrelli* equation as [111]:

$$V = \frac{c\lambda^2}{\left(1 - \frac{\lambda^2}{\lambda_0^2}\right)^2} \quad (2)$$

Where V , λ , and λ_0 are the Verdet constant, the wavelength of the light, and the average resonant wavelength of the material, respectively. C is a wavelength independent constant that includes the Landé factor, the velocity of light, the Planck constant, and the effective transition probability.

The C and λ_0 for each glass can be found by fitting the experimental results with equation (2) as shown by the dashed curves in Fig. 5.4. The C and λ_0 of $\text{Te}_{20}\text{As}_{30}\text{Se}_{50}$ were found to be $0.1079 \text{ deg}\cdot\text{T}^{-1}\cdot\text{m}^{-1}\cdot\text{nm}^{-2}$ and 400 nm, respectively. For $\text{Ge}_{10}\text{Se}_{90}$, C and λ_0 were found to be $0.1517 \text{ deg}\cdot\text{T}^{-1}\cdot\text{m}^{-1}\cdot\text{nm}^{-2}$ and 300 nm, respectively. For $\text{Ge}_{25}\text{As}_{15}\text{S}_{60}$, C and λ_0 were found to be $0.2041 \text{ deg}\cdot\text{T}^{-1}\cdot\text{m}^{-1}\cdot\text{nm}^{-2}$ and 250 nm, respectively. Because the average resonance wavelength of $\text{Te}_{20}\text{As}_{30}\text{Se}_{50}$ is longer than that of $\text{Ge}_{25}\text{As}_{15}\text{S}_{60}$, and $\text{Ge}_{10}\text{Se}_{90}$, a Verdet constant of 870 deg/T/m at 1950 nm is much larger than 229 deg/T/m and 374 deg/T/m of two germanium-based chalcogenide glasses. It is also the highest Verdet constant of glass materials that has been reported in the 2 μm region, to the best of our knowledge.

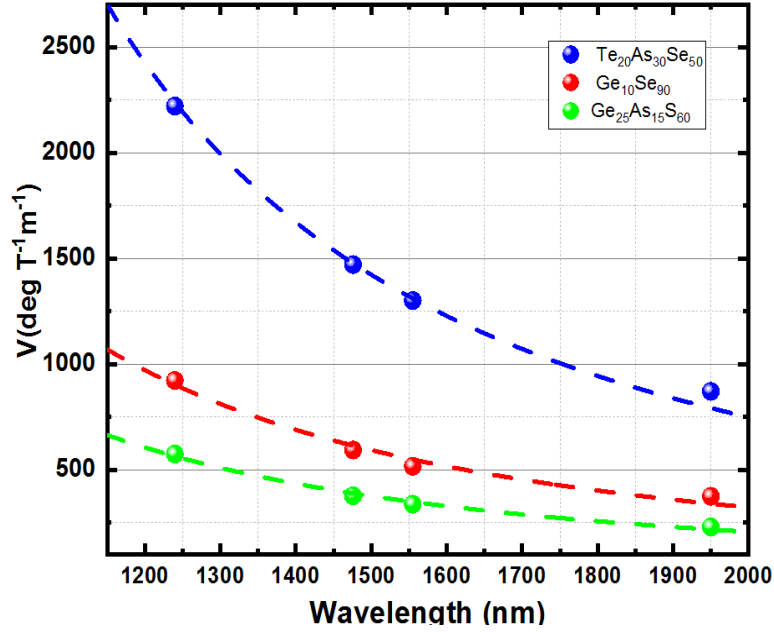


Fig. 5.4: Verdet constants of the three glasses measured at 1240, 1476, 1555, and 1950 nm. The dashed lines are the fitting curves.

Previous studies have shown that the Verdet constants of diamagnetic glasses at $\lambda \gg \lambda_0$ always increase with the increased bandgap absorption edge [122,125]. This can be verified by our experimental data. The measured Verdet constants of $\text{Te}_{20}\text{As}_{30}\text{Se}_{50}$, $\text{Ge}_{25}\text{As}_{15}\text{S}_{60}$, and $\text{Ge}_{10}\text{Se}_{90}$ glasses measured at 1240, 1476, 1555, and 1950 nm were plotted versus the squared bandgap absorption edge and are shown in Fig. 5.5. All the measurement data at the four wavelengths can be fitted with linear curves, indicating that the Verdet constant is approximately proportional to λ^{*2} , which is in agreement with previous observation reported by Jianrong et al.[130]. Therefore, synthesizing diamagnetic glass with a long bandgap absorption edge is an effective method to achieve a high Verdet constant in the mid-IR.

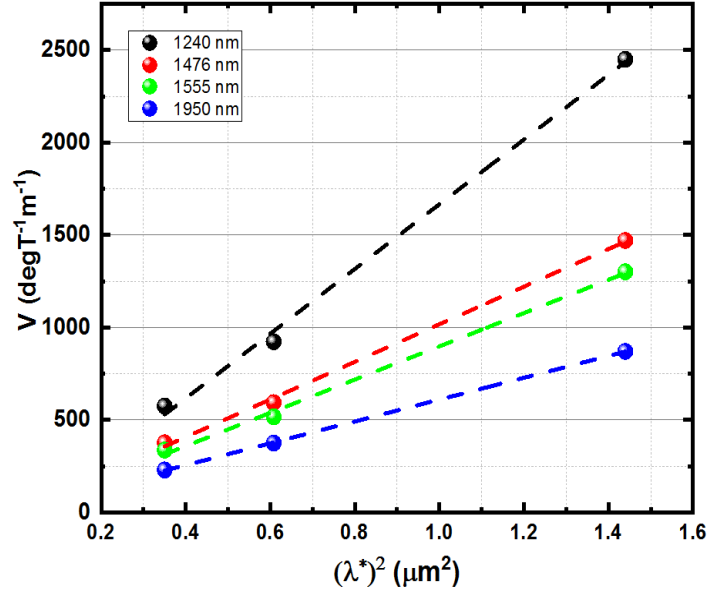


Fig. 5.5: Verdet constants of the three glasses were plotted at the λ^{*2} for the light wavelengths of 1240, 1476, 1555, and 1950 nm.

In addition to large Verdet constant, very low loss is also a desired feature of a MO material. The performance of a MO material is usually evaluated by FOM, which is defined as:

$$\text{FOM} = \frac{V}{\alpha} \quad (3)$$

Where V and α is the Verdet constant and optical transmission loss, respectively. FOM of all three glasses were calculated with measured optical transmission loss and the Verdet constants shown in Fig. 5.6 and are shown in Fig. 5.6. It is clear that the FOM of $\text{Te}_{20}\text{As}_{30}\text{Se}_{50}$ is significantly higher than that of the other two glasses at 1700 - 2100 nm, indicating that $\text{Te}_{20}\text{As}_{30}\text{Se}_{50}$ is a very promising diamagnetic material for MO applications in the 2 μm wavelength region. Similar to the general feature of FOM for other materials, the FOM of $\text{Te}_{20}\text{As}_{30}\text{Se}_{50}$ is very small at short wavelengths close to the bandgap absorption edge due to the large absorption. Because the bandgap absorption always decreases with the increasing wavelength in undoped glasses, the FOM increases as the wavelength goes to longer wavelengths. A maximum FOM of

500 deg/T is obtained at 1905 nm because the Verdet constant also decreases with the increasing wavelength as shown in Fig. 5.4. The FOM beyond 1905 nm decreases with the increasing wavelength because the Verdet constant decreases more rapidly than the optical transmission loss. The FOM of $\text{Ge}_{10}\text{Se}_{90}$ exhibits similar features and has a maximum value of 212 deg/T around 1440 nm. Because the bandgap absorption edges of $\text{Ge}_{25}\text{As}_{15}\text{S}_{60}$ is 592 nm, which is far from the measurement range of 1200-2100 nm, the FOM continuously decreases with the increasing wavelength.

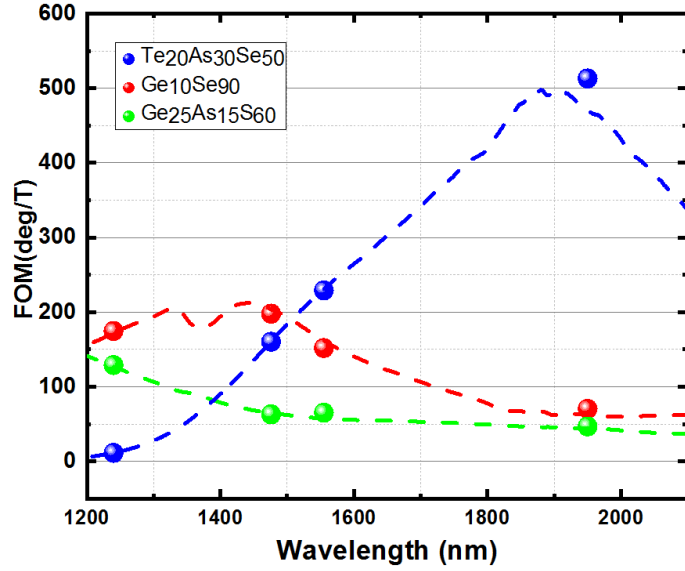


Fig. 5.6: FOMs of $\text{Te}_{20}\text{As}_{30}\text{Se}_{50}$, $\text{Ge}_{25}\text{As}_{15}\text{S}_{60}$, and $\text{Ge}_{10}\text{Se}_{90}$ glasses as a function of the wavelength. The solid dots show the measured FOM.

Aio et al. measured the refractive index of $\text{Te}_{20}\text{As}_{30}\text{Se}_{50}$ in mid IR range[131]. As shown in Fig. 5.7, the black squares are the data measured by *Aio et al.* and Cauchy formula was used to fit the data. The Cauchy coefficients are shown in Fig. 5.7.

Based on the classical electromagnetism theory, the Verdet constant is related to the dispersion of refractive index[132]:

$$V = \left(\frac{-e}{2mc}\gamma\right)\lambda \frac{dn}{d\lambda} (4)$$

Where e , m , c , γ , and $\frac{dn}{d\lambda}$ are electron charge, electron mass, speed of light, magneto optical anomaly factor, and the optical dispersion of the glass respectively. The magneto optical anomaly factor is a function of wavelength and it increases with wavelength for almost all known materials[132]. High value for γ factor (close to unity) shows predominantly ionic bonding and as it deviates from unity, indicates covalent bonding. The following formula was used to find γ factor:

$$\gamma = \frac{V}{\left(\frac{-e}{2mc}\right) \lambda \frac{dn}{d\lambda}} \quad (5)$$

Where V is the Verdet constant obtained from equation (1) for the tellurium based glass. The inset of Fig. 5.7 shows γ factor as a function of wavelength. As it was expected γ factor shows that the nature of bonding in chalcogenide glasses are covalent bond. γ factor also decreases with increasing wavelength.

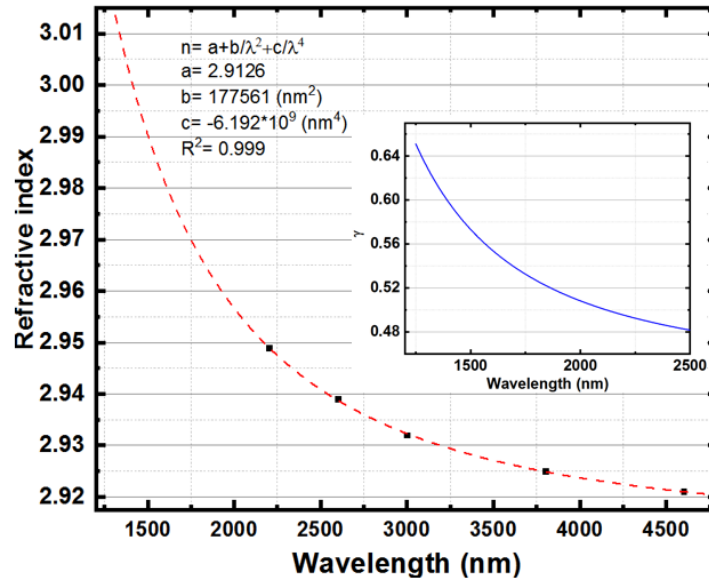


Fig. 5.7: Refractive index of $\text{Te}_2\text{As}_3\text{Se}_5$ glass measured by *Aio et al.* and the dashed line is fitted Cauchy equation. Inset shows the magneto optical anomaly factor as a function of wavelength.

In conclusion, $\text{Te}_{20}\text{As}_{30}\text{Se}_{50}$, $\text{Ge}_{25}\text{As}_{15}\text{S}_{60}$, and $\text{Ge}_{10}\text{Se}_{90}$ glasses were fabricated and their MO properties were measured and analyzed. The bandgap absorption edge and IR multi-phonon absorption edge of $\text{Te}_{20}\text{As}_{30}\text{Se}_{50}$ glass were measured to be 1200 nm and 18 μm , respectively. The Verdet constants at 1555 nm and 1950 nm were measured to be 1300 deg/T/m and 870 deg/T/m, which are much larger than other chalcogenide glasses. The FOM was found to be more than 400 deg/T at the 2 μm wavelength region. All these results show that $\text{Te}_{20}\text{As}_{30}\text{Se}_{50}$ glass is a very promising MO material with low temperature dependence for mid-IR applications.

Chapter 6 Summary and Prospect

6.1 Blue Laser Fiber Amplifier

In this work, the single-frequency blue laser all-fiber amplifier was demonstrated for the first time with more than 150 mW continuous-wave, single frequency and single-transverse-mode blue laser output by pump power of 2 W at 1125 nm. The effect of lasing at 783 nm on blue laser was demonstrated for the first time. We also showed that the effect of photodarkening is not uniform across the fiber and the role of infrared emission is more significant than blue emission in photodarkening. A single-mode fiber amplifier operating at 478 nm was also demonstrated for the concept of blue diode laser oscillator and fiber power amplifier for underwater optical communication system. About 240 mW continuous-wave output signal power was obtained at 478 nm, with 3 W pump laser operating at 1125 nm and then output power began to decrease due to the onset of the 800 nm emission. The net gain amplifier was found to be about 9.2 dB with 9% slope efficiency.

In order to enhance the output power of blue laser fiber amplifier, 800 nm emission needs to be suppressed. Using a double clad Tm^{3+} doped ZBLAN fiber in which the outer cladding was doped with Nd^{3+} was used. It was observed that, 800 nm emission was partially suppressed, but not completely. So, an optimum Nd^{3+} doping level needs to be investigated to enhance the blue emission output. Bending fiber experiment also showed the possibility of suppressing 800 nm lasing. A new fiber design can be investigated with leaky mode for 800 nm emission and guided mode for blue emission to suppress the competitive mode. Photodarkening is also a major limiting factor for further power scaling and long-lived operation of Tm^{3+} -doped ZBLAN fiber amplifiers. Photodarkening in a Tm^{3+} -doped ZBLAN fiber amplifier can be effectively mitigated

by optimizing the Tm^{3+} concentration and the pump power density to reduce the further excited-state excitation from $^1\text{G}_4$ to higher states, and co-doping the fiber core with other elements such as cerium and lanthanum, which serve as traps for free electrons or holes so that the creation of color centers can be inhibited. Further power scaling can also be achieved with more stages of fiber amplifiers with very large core gain fibers. Since a 150 mW output power from first stage amplifier with 10 dB gain was obtained, the second stage amplifier can increase the output power to 1.5 W with 10 dB gain, but an optimum length of second amplifier needs to be investigated. Fig. 6.1 shows a schematic setup of two stages fiber amplifiers for blue laser.

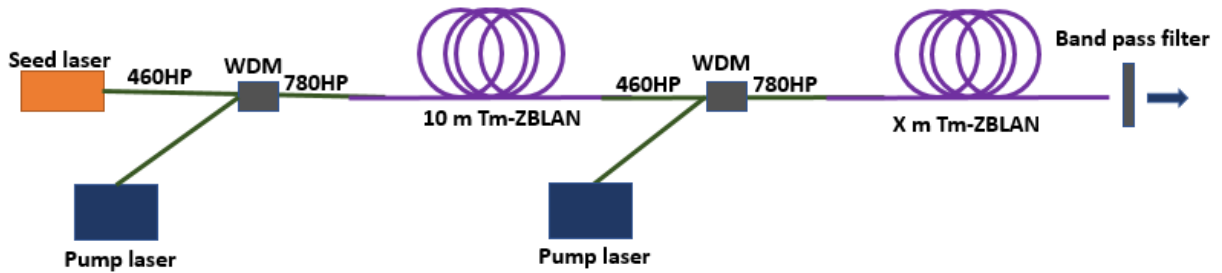


Fig. 6.1: Two stages fiber amplifiers to increase the output power.

6.2 Tm^{3+} doped fluoride fiber laser at 785 nm

An all-single-mode fiber Tm^{3+} -doped ZBLAN laser operating at 785 nm was developed and an output power of about 0.5 W was obtained at a pump power of 8.7 W. A maximum slope efficiency of 17.8 % was obtained with the 3-m fiber as the pump power exceeded 7 W. The overlap between pump, laser, and fiber core was not optimized in the gain fiber. So a new fiber design with higher filling factor is desirable to increase the efficiency and output power. Another major obstacle in this work was high absorption of laser by the gain medium. A new pumping

scheme as shown in Fig. 6.2 can deplete the ground state more effectively. Consequently, it increases the efficiency and output power.

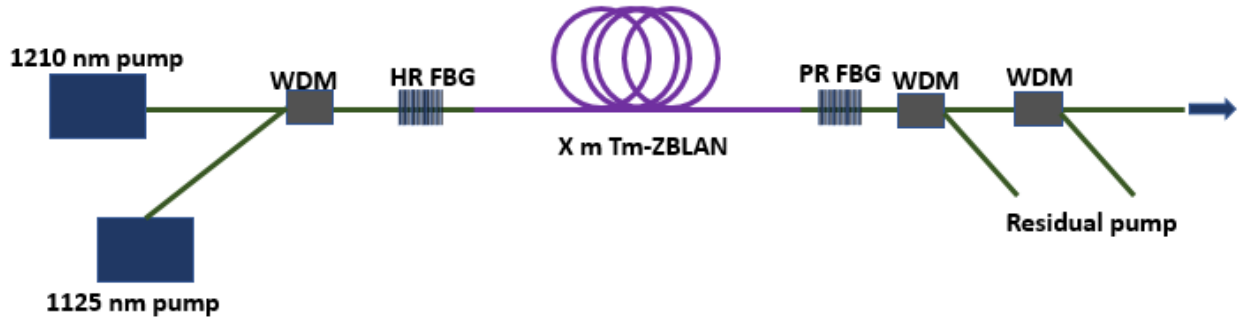


Fig. 6.2: Dual wavelength pumping schemes for 785 nm fiber laser

6.3 Magneto optical properties of Dy^{3+} doped glasses and chalcogenide glasses

In this work, highly Dy^{3+} -doped glasses were fabricated and their magneto-optical properties were studied. The refractive index measurement results indicate that the refractive index increases linearly with the increased Dy_2O_3 concentration. It was found that the measured Verdet constants of Dy^{3+} -doped glasses are in a good agreement with the Van Vleck-Hebb model in the visible and short-wave near IR region and are smaller than the modeling results at longer wavelengths. Nevertheless, a Verdet constant as high as -455 deg/T/m at 1950 nm was measured with a $75 \text{ wt.}\%$ Dy^{3+} doped borate glass which is the highest number reported for a paramagnetic glass at this wavelength.

Three different chalcogenide glasses namely, $Te_{20}As_{30}Se_{50}$, $Ge_{25}As_{15}S_{60}$, and $Ge_{10}Se_{90}$ were also fabricated and their MO properties were measured and analyzed. The bandgap absorption edge and IR multi-phonon absorption edge of $Te_{20}As_{30}Se_{50}$ glass were measured to be 1200 nm and $18 \mu\text{m}$, respectively. The Verdet constants at 1555 nm and 1950 nm were measured to be 1300

deg/T/m and 870 deg/T/m, which are much larger than other chalcogenide glasses. The FOM was found to be more than 400 deg/T at the 2 μ m wavelength region. All these results show that $\text{Te}_{20}\text{As}_{30}\text{Se}_{50}$ glass is a very promising MO material with low temperature dependence for mid-IR applications.

One of the most important applications of magneto optical glasses, is to fabricate all fiber isolator. The main component of an all fiber isolator is the Faraday rotator. The Faraday rotator needs to rotate the linearly polarized light for 45 degrees. Since the Verdet constant in long wavelength decreases significantly, the role of magnet is very important. The strongest magnetic tube, feasible to fabricate based on the different companies that have been contacted is a magnetic tube with 240 mm outer diameter, 10 mm inner diameter, and thickness range from 20 mm to 50 mm. Based on the mentioned dimension and using Nd52 grade, the magnetic field was calculated as shown in Fig. 6.3.

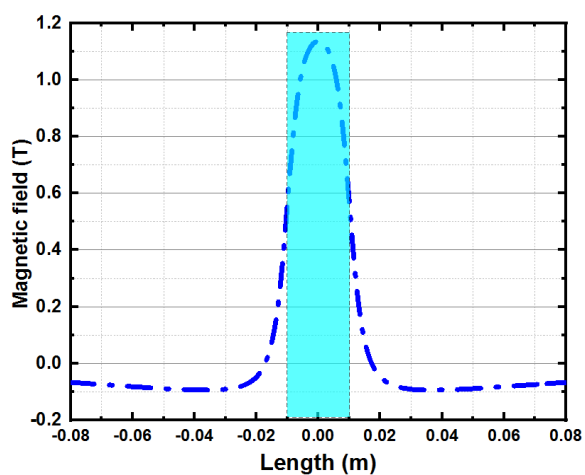


Fig. 6.3: Magnetic field distribution of cylindrical N52 magnets with 5mm inner radius, 120 mm outer radius and thickness of 20 mm.

The rectangular box shows the inside of magnetic tube. As it can be seen the magnetic field out

of magnetic tube is negative.

Faraday rotation as function of thickness of magnetic field for Dy75 glass was simulated as shown in Fig. 6.4. To get 45 degrees rotation just in one magnetic tube, the thickness must be around 25 cm, but with two magnetic tubes of 6.2 cm as marked in Fig. 6.4, and a good magnetic shield, a Faraday rotator with a length of 14 cm can be built. Therefore, a shorter Dy fiber is needed.

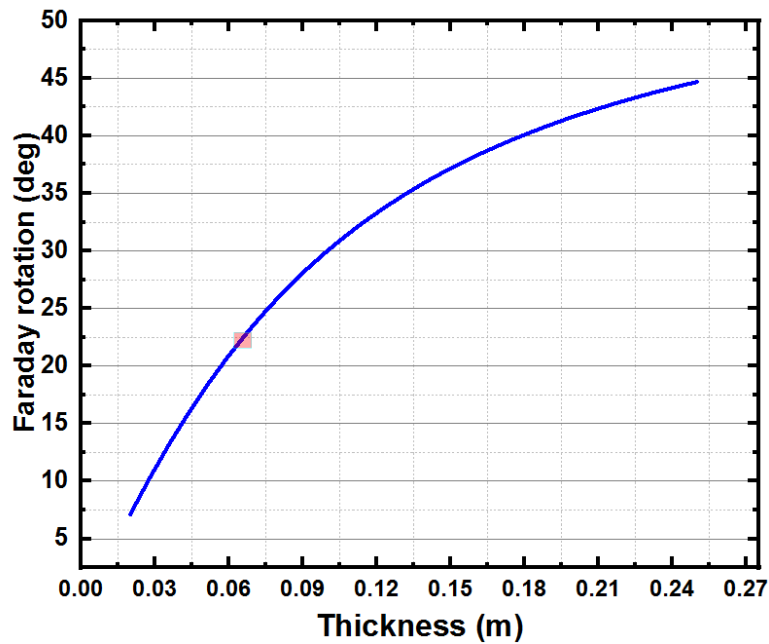


Fig. 6.4: Faraday rotation as a function of thickness of magnetic tube for Dy75 glass.

Faraday rotation as function of thickness of magnetic field for $\text{Te}_{20}\text{As}_{30}\text{Se}_5$ glass was simulated as shown in Fig. 6.5. due to high Verdet constant of $\text{Te}_{20}\text{As}_{30}\text{Se}_5$ glass, a magnetic tube with a thickness of 8 cm is enough to obtain 45 deg rotation. The disadvantage of chalcogenide fibers is that they are not able to handle high power.

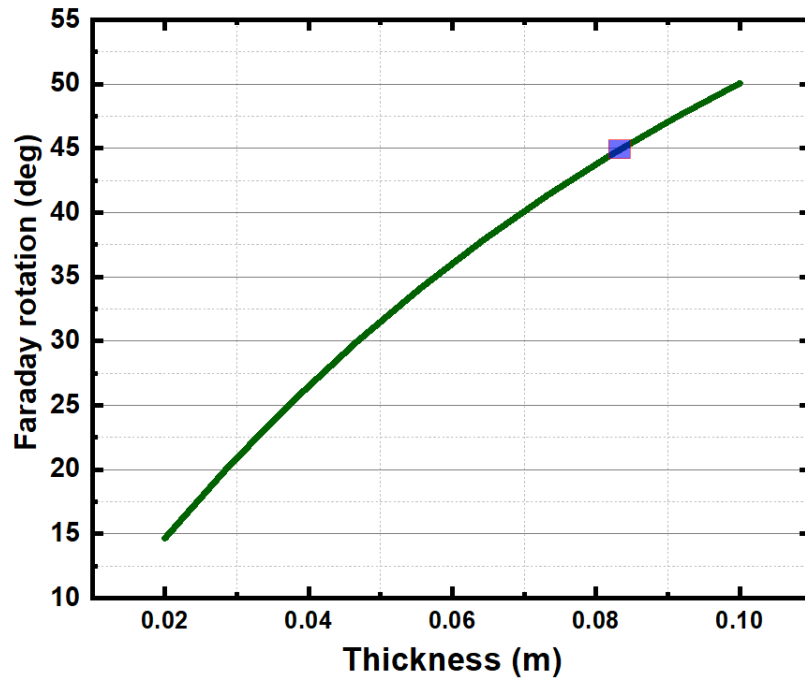


Fig. 6.5: Faraday rotation as a function of thickness of magnetic tube for tellurium based glass.

References

1. K. Muirhead and A. P. Cracknell, "Airborne lidar bathymetry," *Int. J. Remote Sens.* **7**(5), 597–614 (1986).
2. T. Tanaka, K. Takahashi, K. Sako, R. Kasegawa, M. Toishi, K. Watanabe, D. Samuels, and M. Takeya, "Littrow-type external-cavity blue laser for holographic data storage.," *Appl. Opt.* **46**(17), 3583–3592 (2007).
3. N. Yoshida, N. Yagi, Y. Inada, M. Kugai, T. Okayama, K. Kamada, K. Katada, K. Uchiyama, T. Ishikawa, O. Handa, T. Takagi, H. Konishi, S. Kokura, A. Yanagisawa, and Y. Naito, "Ability of a novel blue laser imaging system for the diagnosis of colorectal polyps," *Dig. Endosc.* **26**(2), 250–258 (2014).
4. R. Toriumi, H. Tai, and N. Takeuchi, "Tunable solid-state blue laser differential absorption lidar system for NO₂ monitoring," *Opt. Eng.* **35**(8), 2371–2375 (1996).
5. Kazutomo Togashi, D. Nemoto, K. Utano, N. Isohata, Kensuke Kumamoto, S. Endo, and A. K. Lefor, "Blue laser imaging endoscopy system for the early detection and characterization of colorectal lesions: a guide for the endoscopist," *Ther. Adv. Gastroenterol* **9**(1), 50–56 (2016).
6. T. C. Wu, Y. C. Chi, H. Y. Wang, C. T. Tsai, and G. R. Lin, "Blue laser diode enables underwater communication at 12.4 gbps," *Sci. Rep.* **7**(December 2016), 1–10 (2017).
7. O. Svelto, *Principles of Lasers*, 5th ed. (Springer, 2010).
8. S. C. Wang and A. E. Siegman, "Hollow-Cathode Transverse Discharge He-Ne and He-

- Cd Lasers," *Appl. Phys.* **2**, 143–150 (1973).
9. S. Nakamura, M. Senoh, S. I. Nagahama, N. Iwasa, T. Yamada, T. Matsushita, H. Kiyoku, and Y. Sugimoto, "InGaN-Based Multi-Quantum-Well-Structure Laser Diodes," *Jpn. J. Appl. Phys.* **35**, L74–L76 (1996).
 10. S. Nakamura, S. Pearton, and G. Fasol, *The Blue Laser Diode: The Complete Story*, 2nd ed. (Springer, 2000).
 11. Wallace R. W and Harris S. E, "Oscillation and Doubling of the 0.946 μm Line in Nd:YAG," *Appl. Phys. Lett.* **15**(4), 111–112 (1969).
 12. Z. Quan, Y. Yi, L. Bin, Q. Dapeng, and Z. Ling, "13.2 W laser-diode-pumped Nd:YVO₄/LBO blue laser at 457 nm," *J. Opt. Soc. Am. B* **26**(6), 1238–1242 (2010).
 13. M. Lukowski, C. Hassenius, and M. Fallahi, "Widely Tunable High-Power Two-Color VECSELs for New Wavelength Generation," *IEEE J. Sel. Top. Quantum Electron.* **21**(1), 432–439 (2015).
 14. M. Ghotbi, M. Ebrahim-Zadeh, A. Majchrowski, E. Michalski, and I. V Kityk, "High-average-power femtosecond pulse generation in the blue using BiB₃O₆," *Opt. Lett.* **29**(21), 2530–2532 (2004).
 15. R. G. Smart, D. C. Hanna, A. C. Tropper, S. T. Davey, S. F. Carter, and D. Szebesta, "CW Room Temperature Upconversion Lasing at Blue, Green and Red Wavelengths in Infrared-Pumped Pr³⁺-Doped Fluoride Fibre," *Electron. Lett.* **27**(14), 1307–1309 (1991).
 16. S. G. Grubb, K. W. Bennett, R. S. Cannon, and W. F. Humer, "CW room-temperature

- blue upconversion fibre laser," *Electron. Lett.* **28**(13), 1243–1244 (1992).
17. X. Zhu and N. Peyghambarian, "High-power ZBLAN glass fiber lasers: Review and prospect," *Adv. Optoelectron.* **2010**, (2010).
 18. R. Allen and L. Esterowitz, "Cw Diode Pumped 2.3 Mm Fiber Laser," *Appl. Phys. Lett.* **55**(8), 721–722 (1989).
 19. M. Mollaei, X. Zhu, J. Zong, K. Wiersma, A. Chavez-Pirson, R. A. Norwood, and N. Peyghambarian, "Half-Watt Tm³⁺-Doped Fluoride Fiber Laser at 785 nm," *IEEE Photonics Technol. Lett.* **30**(17), 1563–1566 (2018).
 20. M. Mollaei, X. Zhu, J. Zong, K. Wiersma, A. Chavez-Pirson, M. Akbulut, Y. Kaneda, L. Lacombe, A. Schülzgen, and A. N. Peyghambarian, "Single-frequency blue laser fiber amplifier," *Opt. Lett.* **43**(3), 423–426 (2018).
 21. J. Y. Allain, M. Monerie, and H. Poignant, "Blue Upconversion Fluorozirconate Fibre Laser," *Electron. Lett.* **26**(3), 166–168 (1990).
 22. S. G. Grubb, K. W. Bennett, R. S. Cannon, and W. F. Humer, "CW Room- Temperature Blue Upconversion Fiber Laser," in *CLEO* (1992), p. CPD18.
 23. S. Sanders, R. G. Waarts, D. G. Mehuys, and D. F. Welch, "Laser diode pumped 106 mW blue upconversion fiber laser," *Appl. Phys. Lett.* **67**(13), 1815–1817 (1995).
 24. H. Zellmer, S. Buteau, A. Tünnermann, and H. Welling, "All fibre laser system with 0.1 W output power in blue spectral range," *Electron. Lett.* **33**(16), 1383–1384 (1997).
 25. R. Paschotta, N. Moore, W. A. Clarkson, A. C. Tropper, D. C. Hanna, and G. Mazé, "230

- mW of blue light from a thulium-doped upconversion fiber laser," *IEEE J. Sel. Top. Quantum Electron.* **3**(4), 1100–1102 (1997).
26. T. Maiman, "Stimulated Optical Radiation in Ruby," *Nature* **187**(4736), 493–494 (1960).
 27. T. Qiu, L. Li, A. Schülzgen, V. L. Temyanko, T. Luo, S. Jiang, A. Mafi, J. V. Moloney, and N. Peyghambarian, "Generation of 9.3-W multimode and 4-W single-mode output from 7-cm short fiber lasers," *IEEE Photonics Technol. Lett.* **16**(12), 2592–2594 (2004).
 28. J. S. Sanghera, L. B. Shaw, P. Pureza, V. Q. Nguyen, D. Gibson, L. Busse, I. D. Aggarwal, C. M. Florea, and F. H. Kung, "Nonlinear Properties of Chalcogenide Glass Fibers," *Int. J. Appl. Glas. Sci.* **1**(3), 296–308 (2010).
 29. R. E. Slusher, G. Lenz, J. Hodelin, J. Sanghera, L. B. Shaw, and I. D. Aggarwal, "Large Raman gain and nonlinear phase shifts in high-purity As₂Se₃ chalcogenide fibers," *J. Opt. Soc. Am. B* **21**(6), 1146 (2004).
 30. A. Mori, Y. Ohishi, T. Kanamori, and S. Shoichi, "Optical amplification with neodymium-doped chalcogenide glass fiber," *Appl. Phys. Lett.* **70**, 1230–1232 (1997).
 31. T. Schweizer, B. N. Samson, R. C. Moore, D. W. Hewak, and D. N. Payne, "Rare-earth doped chalcogenide glass fibre laser," *Electron. Lett.* **33**(5), 414–416 (1997).
 32. V. Fortin, M. Bernier, S. T. Bah, and R. Vallée, "30 W fluoride glass all-fiber laser at 2.94 μm ," *Opt. Lett.* **40**(12), 2882–2885 (2015).
 33. S. Tokita, M. Murakami, S. Shimizu, M. Hashida, and S. Sakabe, "Liquid-cooled 24 W mid-infrared Er:ZBLAN fiber laser," *Opt. Lett.* **34**(20), 3062–3064 (2009).

34. J. S. Sanghera, L. B. Shaw, L. E. Busse, V. Q. Nguyen, P. C. Pureza, B. C. Cole, B. B. Harrison, I. D. Aggarwal, R. Mossadegh, F. Kung, D. Talley, D. Roselle, and R. Miklos, "Development and Infrared Applications of Chalcogenide Glass Optical Fibers," *Fiber Integr. Opt.* **19**, 251–274 (2000).
35. M. Poulain, M. Poulain, and J. Lucas, "Verres fluores au tetrafluorure de zirconium proprietes optiques d'un verre dope au Nd³⁺," *Mater. Res. Bull.* **10**(4), 243–246 (1975).
36. K. Ohsawa, T. Shibata, K. Nakamura, and S. Yoshida, "Fluorozirconate glasses for infrared transmitting optical fibers," in *The 7th European Conference on Optical Communication* (1981), pp. 1–1.
37. P. . France, M. G. Drexhage, J. M. Parker, M. W. Moore, S. F. Carter, and J. V Wright, *Fluoride Glass Optical Fibers*, 1st ed. (CRC Press, 1990).
38. M. Saad, "High purity fluoride glass synthesis: a review," in *SPIE Photonics West, Laser Refrigeration of Solids II*, (2009), **7228**, pp. 72280G1-72280G13.
39. J. M. Parker, "Fluoride glasses," *Annu. Rev. Mater. Sci.* **19**(1), 21–41 (1989).
40. T. Kanamori and S. Sakaguchi, "Preparation of Elevated NA Fluoride Optical Fibers," *Jpn. J. Appl. Phys.* **25**(6), L468–L470 (1986).
41. F. Gan, "Optical properties of fluoride glasses: a review," *J. Non. Cryst. Solids* **184**, 9–20106 (1995).
42. L. Qin, Z. X. Shen, B. L. Low, H. K. Lee, T. J. Lu, Y. S. Dai, S. H. Tang, and M. H. Kuok, "Crystallization study of heavy metal fluoride glasses ZBLAN by Raman

- spectroscopy," *J. Raman Spectrosc.* **28**(7), 495–499 (1997).
43. J. Schneider, C. Carbonnier, and U. B., "Characterization of a Ho³⁺-doped fluoride fiber laser with a 3.9 μm emission wavelength," *Appl. Opt.* **36**(33), 8595–8600 (1997).
 44. R. M. El-Agmy, "Upconversion CW laser at 284 nm in a Nd:YAG-pumped double-cladding thulium-doped ZBLAN fiber laser," *Laser Phys.* **18**(6), 803–806 (2008).
 45. D. D. Davis and R. M. Bozorth, "Magnetic Properties of Thulium Metal," *Phys. Rev.* **118**(6), 1543–1545 (1960).
 46. W. Tian and B. Rami Reddy, "Ultraviolet upconversion in thulium-doped fluorozirconate fiber observed under two-color excitation," *Opt. Lett.* **26**(20), 1580 (2001).
 47. H. Yang and J. Gao, "Different dynamics of ultraviolet upconversion in Tm³⁺:ZBLAN glass under blue laser excitation," *Phys. B Condens. Matter* **426**(3888), 31–34 (2013).
 48. J. L. Doualan, S. Girard, H. Haquin, J. L. Adam, and J. Montagne, "Spectroscopic properties and laser emission of Tm doped ZBLAN glass at 1.8 μm ," *Opt. Mater. (Amst.)* **24**(3), 563–574 (2003).
 49. B. M. Walsh and N. P. Barnes, "Comparison of Tm: ZBLAN and Tm: Silica fiber lasers; Spectroscopy and tunable pulsed laser operation around 1.9 μm ," *Appl. Phys. B Lasers Opt.* **78**(3–4), 325–333 (2004).
 50. J. Sanz, R. Cases, and R. Alcalá, "Optical properties of Tm³⁺ in fluorozirconate glass," *J. Non. Cryst. Solids* **93**(2–3), 377–386 (1987).
 51. P. Peterka, I. Kasik, A. Dhar, B. Dussardier, and W. Blanc, "Theoretical modeling of fiber

- laser at 810 nm based on thulium-doped silica fibers with enhanced 3H4 level lifetime.," *Opt. Express* **19**(3), 2773–2781 (2011).
52. J. W. Dawson, M. J. Messerly, R. J. Beach, M. Y. Shverdin, E. A. Stappaerts, A. K. Sridharan, P. H. Pax, J. E. Heebner, C. W. Siders, and C. P. J. Barty, "Analysis of the scalability of diffraction-limited fiber lasers and amplifiers to high average power," *Opt. Express* **16**(17), 13240–13266 (2008).
53. P. Laperle, A. Chandonnet, and R. Vallée, "Photobleaching of thulium-doped ZBLAN fibers with visible light," *Opt. Lett.* **22**(3), 178–80 (1997).
54. G. Qin, S. Huang, Y. Feng, A. Shirakawa, M. Musha, and K. I. Ueda, "Photodegradation and photocuring in the operation of a blue upconversion fiber laser," *J. Appl. Phys.* **97**(12), 1–4 (2005).
55. S. Q. Duntley, "Light in the Sea," *J. Opt. Soc. Am.* **53**(2), 214–233 (1961).
56. J. Xu, M. Kong, A. Lin, Y. Song, X. Yu, F. Qu, J. Han, and N. Deng, "OFDM-based broadband underwater wireless optical communication system using a compact blue LED," *Opt. Commun.* **369**, 100–105 (2016).
57. M. Doniec, M. Angermann, and D. Rus, "An end-to-end signal strength model for underwater optical communications," *IEEE J. Ocean. Eng.* **38**(4), 743–757 (2013).
58. T. C. Wu, Y. C. Chi, H. Y. Wang, C. T. Tsai, and G. R. Lin, "Blue laser diode enables underwater communication at 12.4 gbps," *Sci. Rep.* **7**, 1–10 (2017).
59. K. Nakamura, I. Mizukoshi, and M. Hanawa, "Optical wireless transmission of 405 nm,

- 145 Gbit/s optical IM/DD-OFDM signals through a 48 m underwater channel," *Opt. Express* **23**(2), 1558–1566 (2015).
60. H. M. Oubei, J. R. Duran, B. Janjua, H.-Y. Wang, C.-T. Tsai, Y.-C. Chi, T. K. Ng, H.-C. Kuo, J.-H. He, M.-S. Alouini, G.-R. Lin, and B. S. Ooi, "48 Gbit/s 16-QAM-OFDM transmission based on compact 450-nm laser for underwater wireless optical communication," *Opt. Express* **23**(18), 23302–23309 (2015).
61. P. Tian, X. Liu, S. Yi, Y. Huang, S. Zhang, X. Zhou, L. Hu, L. Zheng, and R. Liu, "High-speed underwater optical wireless communication using a blue GaN-based micro-LED," *Opt. Express* **25**(2), 1193–1201 (2017).
62. B. B. Shih, D. Allan, F. de Gruijl, and L. E. R; Rhodes, "Robust Detection of Minimal Sunburn in Pigmented Skin by 785 nm Laser Speckle Contrast Imaging of Blood Flux," *J. Invest. Dermatol.* **135**(4), 1197–1199 (2015).
63. H. J. Butler, L. Ashton, B. Bird, G. Cinque, K. Curtis, J. Dorney, K. Esmonde-White, N. J. Fullwood, B. Gardner, P. L. Martin-Hirsch, M. J. Walsh, M. R. McAinsh, N. Stone, and F. L. Martin, "Using Raman spectroscopy to characterize biological materials," *Nat. Protoc.* **11**, 664–687 (2016).
64. S.-T. Ha, C. Shen, J. Zhang, and Q. Xiong, "Laser cooling of organic–inorganic lead halide perovskites," *Nat. Photonics* **10**, 115–121 (2016).
65. B. Sumpf, J. Fricke, M. Maiwald, A. Müller, P. Ressel, F. Bugge, G. Erbert, and G. Tränkle, "Wavelength stabilized 785 nm DBR-ridge waveguide lasers with an output power of up to 215 mW," *Semicond. Sci. Technol.* **29**(4), 045025 (2014).

66. V. Bolpasi and W. Von Klitzing, "Double-pass tapered amplifier diode laser with an output power of 1 W for an injection power of only 200 μ W," *Cit. Rev. Sci. Instruments* **81**(101), (2010).
67. Y. Wei, H. Lu, P. Jin, A. K. Peng, H. D. Lu, J. Su, C. D. Xie, and K. C. Peng, "Self-injection locked CW single-frequency tunable Ti:sapphire laser," *Opt. Express* **25**(18), 21379–21387 (2017).
68. S.-W. Chiow, T. Kovachy, J. M. Hogan, and M. A. Kasevich, "Generation of 43 W of quasi-continuous 780 nm laser light via high-efficiency, single-pass frequency doubling in periodically poled lithium niobate crystals," *Opt. Lett.* **37**(18), 3861–3863 (2012).
69. M. L. Dennis, J. W. Dixon, and I. Aggarwal, "High power upconversion lasing at 810nm. Tm-ZBLAN fibre," *Electron. Lett.* **30**(2), 1993–1994 (1994).
70. A. F. H. Librantz, L. Gomes, G. Pairier, S. J. L. Ribeiro, and Y. Messaddeq, "Tm and Tm–Tb-doped germanate glasses for S-band amplifiers," *J. Lumin.* **128**, 51–59 (2008).
71. G. Androz, D. Faucher, D. Gingras, and R. Vallée, "Self-pulsing dynamics of a dual-wavelength Tm³⁺:ZBLAN upconversion fiber laser emitting around 800 nm," *J. Opt. Soc. Am. B* **24**(11), 2907–2913 (2007).
72. J. Y. Allain, M. Monerie, and H. Poignant, "Tunable CW lasing around 0.82, 1.48, 1.88 and 2.35 μ m in thulium-doped fluorozirconate fibre," *Electron. Lett.* **25**(24), 1660–1662 (1989).
73. F. Duclos and P. Urquhart, "Thulium-doped ZBLAN blue upconversion fiber laser:

- theory," *J. Opt. Soc. Am. B* **12**(4), 709–717 (1995).
74. B. M. Walsh and U. N. P. Barnes, "Applied Physics B Comparison of Tm : ZBLAN and Tm : silica fiber lasers; Spectroscopy and tunable pulsed laser operation around 1.9 μm ," *Appl. Phys. B* **78**, 325–333 (2004).
 75. G. S. Qin, S. H. Huang, Y. Feng, A. Shirakawa, and K. Ueda, "784-nm amplified spontaneous emission from Tm³⁺-doped fluoride glass fiber pumped by an 1120-nm fiber laser," *Opt. Lett.* **30**(3), 269–271 (2005).
 76. G. Qin, S. Huang, F. Yan, A. Shirakawa, and K. I. Ueda, "Multiple-Wavelength Up-Conversion Laser in Tm³⁺-Doped ZBLAN Glass Fiber," *IEEE Photonics Technol. Lett.* **17**(9), 1818–1820 (2005).
 77. S. Jiang and J. Wang, "Method of fusion splicing silica fiber with low-temperature multi-component glass fiber," (2004).
 78. X. Wang, X. Jin, P. Zhou, X. Wang, H. Xiao, Z. Liu, Z. Li, A. M. Heidt, P. S. Teh, M. Berendt, J. K. Sahu, R. Phelan, B. Kelly, S. U. Alam, and D. J. Richardson, "105 W ultra-narrowband nanosecond pulsed laser at 2 μm based on monolithic Tm-doped fiber MOPA," *Opt. Express* **23**(47), 4233–4241 (2015).
 79. K. Scholle, S. Lamrini, P. Koopmann, and P. Fuhrberg, *Frontiers in Guided Wave Optics and Optoelectronics* (2010).
 80. D. Kracht, H. Sayinc, S. Yilmaz, M. Wyszomolek, K. Hausmann, C. Ottenhues, D. Wandt, A. Wienke, and J. Neumann, "Innovative laser sources operating around 2 μm ," *Phys.*

- Procedia **83**, 1184–1195 (2016).
81. N. Leindecker, A. Marandi, R. L. Byer, K. L. Vodopyanov, J. Jiang, I. Hartl, M. Fermann, and P. G. Schunemann, "Octave-spanning ultrafast OPO with 26-61 μ m instantaneous bandwidth pumped by femtosecond Tm-fiber laser," *Opt. Express* **20**(7), 7046 (2012).
 82. S. Agger and J. H. Povlsen, "Single-frequency thulium-doped distributed-feedback fiber laser," *Opt. Lett.* **29**(13), 1503–1505 (2004).
 83. N. Y. Voo, J. K. Sahu, and M. Ibsen, "345-mW 1836-nm single-frequency DFB fiber laser MOPA," *IEEE Photonics Technol. Lett.* **17**(12), 2550–2552 (2005).
 84. J. Geng, Q. Wang, T. Luo, S. Jiang, and F. Amzajerdian, "Single-frequency narrow-linewidth Tm-doped fiber laser using silicate glass fiber," *Opt. Lett.* **34**(22), 3493–3495 (2009).
 85. Z. Zhang, A. J. Boyland, J. K. Sahu, W. A. Clarkson, and M. Ibsen, "High-power single-frequency thulium-doped fiber DBR laser at 1943 nm," *IEEE Photonics Technol. Lett.* **23**(7), 417–419 (2011).
 86. X. Wang, P. Zhou, X. Wang, H. Xiao, L. Si, N. Park, J. W. Dawson, K. J. Vahala, C. Miller, C. Yang, S. Xu, S. Mo, C. Li, Z. Feng, D. Chen, Z. Yang, and Z. Jiang, "102 W monolithic single frequency Tm-doped fiber MOPA," *Opt. Express* **21**(26), 32386–32392 (2013).
 87. C. W. Rudy, M. J. F. Digonnet, and R. L. Byer, "Advances in 2- μ m Tm-doped mode-locked fiber lasers," *Opt. Fiber Technol.* **20**(6), 642–649 (2014).

88. J. Geng, Q. Wang, J. Smith, T. Luo, F. Amzajerjian, and S. Jiang, "All-fiber Q-switched single-frequency Tm-doped laser near 2 μm ," *34*(23), 3713–3715 (2009).
89. E. Lucas, L. Lombard, Y. Jaouën, S. Bordais, and G. Canat, "1 kW peak power, 110 ns single-frequency thulium doped fiber amplifier at 2050 nm," *Appl. Opt.* **53**(20), 4413–4419 (2014).
90. Q. Fang, K. Kieu, W. Shi, E. Petersen, A. Chavez-Pirson, and N. Peyghambarian, "High energy high peak power monolithic single frequency 2 μm nanosecond pulsed fiber laser system," *Opt. Express* **20**(15), 16410–16420 (2012).
91. W. Shi, E. B. Petersen, D. T. Nguyen, Z. Yao, A. Chavez-Pirson, N. Peyghambarian, and J. Yu, "220 μJ monolithic single-frequency Q-switched fiber laser at 2 μm by using highly Tm-doped germanate fibers," *Opt. Lett.* **36**(18), 3575 (2011).
92. L. E. Nelson, E. P. Ippen, and H. A. Haus, "Broadly tunable sub-500 fs pulses from an additive-pulse mode-locked thulium-doped fiber ring laser," *Appl. Phys. Lett.* **67**(19), (1995).
93. R. C. Sharp, D. E. Spock, N. Pan, and J. Elliot, "190 Fs Passively Mode-Locked Thulium Fiber Laser With Low Threshold," *Opt. Lett.* **21**(12), 31 (1996).
94. F. Haxsen, A. Ruehl, M. Engelbrecht, D. Wandt, U. Morgner, and D. Kracht, "Stretched-pulse operation of a thulium-doped fiber laser," *Opt. Express* **16**(25), 20471 (2008).
95. J. Jiang, C. Mohr, J. Bethge, A. Mills, W. Mefford, I. Hartl, M. E. Fermann, C. C. Lee, S. Suzuki, T. R. Schibli, N. Leindecker, K. L. Vodopyanov, and P. G. Schunemann, "500

- MHz, 58fs highly coherent Tm fiber soliton laser," CLEO Appl. Technol. CLEO_AT 2012 2–3 (2012).
96. R. Andrew Sims, P. Kadwani, L. Shah, and M. Richardson, "All thulium fiber CPA system with 107 fs pulse duration and 42 nm bandwidth," Opt. InfoBase Conf. Pap. 4–6 (2011).
 97. J. Cajzl, P. Peterka, M. Kowalczyk, J. Tarka, G. Sobon, J. Sotor, J. Aubrecht, P. Honzátko, and I. Kašík, "Thulium-Doped Silica fibers with enhanced fluorescence lifetime and their application in ultrafast fiber lasers," *Fibers* **6**(3), (2018).
 98. S. D. Jackson and S. Mossman, "Efficiency dependence on the Tm³⁺ and Al³⁺ concentrations for Tm³⁺-doped silica double-clad fiber lasers," *Appl. Opt.* **42**(15), 2702 (2003).
 99. G. Bendelli, S. Donati, E. Universita, and V. Abbiategrasso, "Optical Isolators for Telecommunications: Review and Current Trends," *Opt. Commun.* **3**, 373–380 (1992).
 100. L. Sun, S. Jiang, and J. R. Marciante, "All-fiber optical magnetic-field sensor based on Faraday rotation in highly terbium-doped fiber," *Opt. Express* **18**(6), 5407 (2010).
 101. Y. Huang, H. Chen, W. Dong, F. Pang, J. Wen, Z. Chen, and T. Wang, "Fabrication of europium-doped silica optical fiber with high Verdet constant," *Opt. Express* **24**(16), 181–189 (2016).
 102. Q. Chen, Y. Qiao, H. Wang, and Q. Chen, "Spectra and magneto optical behavior of CeO₂ doped heavy metal diamagnetic glass," *J. Non. Cryst. Solids* **470**, 70–77 (2017).

103. J. M. Lock, "Magnetism and the Rare-Earth Metals," *R. Radar Establ. J.* 93–105 (1958).
104. C. B. Rubinstein, L. G. Van Uitert, and W. H. Grodkiewicz, "Magneto-Optical Properties of Rare Earth (III) Aluminum Garnets," *J. Appl. Phys.* **35**(121), 3069–3071 (1964).
105. I. L. Snetkov, A. I. Yakovlev, D. A. Permin, S. S. Balabanov, and O. V Palashov, "Magneto-optical Faraday effect in dysprosium oxide (Dy_2O_3) based ceramics obtained by vacuum sintering," *Opt. Lett.* **43**(16), 4041–4044 (2018).
106. A. V Malakhovskii, I. S. Edelman, Y. Radzyner, Y. Yeshurun, A. M. Potseluyko, T. V Zarubina, A. V Zamkov, and A. I. Zaitzev, "Magnetic and magneto-optical properties of oxide glasses containing Pr^{3+} , Dy^{3+} and Nd^{3+} ions," *J. Magn. Magn. Mater.* **263**, 161–172 (2003).
107. E. Culea and I. Bratu, "Structural and magnetic behaviour of some borate glasses containing dysprosium ions," *J. Non-Cryst. Solids* **262**, 287–290 (2000).
108. C. B. Rubinstein, S. B. Berger, L. G. Van Uitert, and W. A. Bonner, "Faraday Rotation of Rare-Earth (III) Borate Glasses," *J. Appl. Phys.* **35**(8), 2338–2340 (1964).
109. A. Sommerfeld, "Optics (trans: Laporte, O., Moldauer, PA)," A., New York (1964).
110. P. R. Berman, "Optical Faraday rotation," *Am. J. Phys.* **78**(3), 270–276 (2010).
111. N. F. Borrelli, "Faraday Rotation in Glasses," *J. Chem. Phys* **41**, 3289–3293 (1964).
112. G. Gao, A. Winterstein-beckmann, O. Surzhenko, C. Dubs, and J. Dellith, "Faraday rotation and photoluminescence in heavily Tb -doped $\text{GeO}_2\text{-B}_2\text{O}_3\text{-Al}_2\text{O}_3\text{-Ga}_2\text{O}_3$ glasses for fiber-integrated magneto-optics," *Sci. Rep.* **5**, 1–6 (2015).

113. I. L. Snetkov, R. Yasuhara, A. V. Starobor, E. A. Mironov, and O. V. Palashov, "Thermo-Optical and Magneto-Optical Characteristics of Terbium Scandium Aluminum Garnet Crystals," *IEEE J. Quantum Electron.* **51**(7), (2015).
114. D. Vojna, R. Yasuhara, O. Slezák, J. Mužík, A. Lucianetti, and T. Mocek, "Verdet constant dispersion of CeF₃ in the visible and near-infrared spectral range," *Opt. Eng.* **56**(6), 1–4 (2017).
115. N. B. Er and E. Loh, "Lowest 4f ~ 5d Transition of Trivalent Rare-Earth Ions in CaF₂ Crystals," *Phys. Rev.* **147**, (1966).
116. J. C. Krupa and M. Queffelec, "UV and VUV optical excitations in wide band gap materials doped with rare earth ions: 4f-5d transitions," *J. Alloys Compd.* **250**, 287–292 (1997).
117. L. Sun, S. Jiang, and J. R. Marciante, "All-fiber optical magnetic-field sensor based on Faraday rotation in highly terbium-doped fiber," *Opt. Express* **18**(6), 5407–5412 (2010).
118. H. Dötsch, N. Bahlmann, O. Zhuromskyy, M. Hammer, L. Wilkens, R. Gerhardt, P. Hertel, and A. F. Popkov, "Applications of magneto-optical waveguides in integrated optics: review," *J. Opt. Soc. Am. B* **22**, 240–253 (2005).
119. W. A. Crossley, R. W. Copper, and J. L. Page, "Faraday Rotation in Rare-Earth Iron Garnets," *Phys. Rev.* **181**, 896–904 (1969).
120. L. Sun, S. Jiang, J. D. Zuegel, and J. R. Marciante, "Effective Verdet constant in a terbium-doped-core phosphate fiber," *Opt. Lett.* **34**(11), 1699–1701 (2009).

121. A. I. Yakovlev, I. L. Snetkov, V. V. Dorofeev, and S. E. Motorin, "Magneto-optical properties of high-purity zinc-tellurite glasses," *J. Non. Cryst. Solids* **480**(August 2017), 90–94 (2018).
122. Y. Ruan, R. A. Jarvis, A. V Rode, S. Madden, and B. Luther-Davies, "Wavelength dispersion of Verdet constants in chalcogenide glasses for magneto-optical waveguide devices," *Opt. Commun.* **252**, 39–45 (2005).
123. X. Xiao, X. Cui, F. Gao, J. Cui, X. Liu, H. Guo, J. She, G. Chen, B. Peng, C. J. Firby, A. Y. Elezzabi, H. Dötsch, N. Bahlmann, O. Zhuromskyy, M. Hammer, L. Wilkens, R. Gerhardt, P. Hertel, and A. F. Popkov, "Improvement of the Faraday effect in Ge-S based chalcogenide glasses via gallium and lead compositional modifications," *Opt. Mater. Express* **8**(7), 1754 (2018).
124. Y. Xu, H. Guo, X. Xiao, P. Wang, X. Cui, M. Lu, C. Lin, S. Dai, and B. O. Peng, "High Verdet constants and diamagnetic responses of GeS₂-In₂S₃-PbI₂ chalcogenide glasses for integrated optics applications," *Opt. Express* **25**, 20410–20420 (2017).
125. G. Chen, Y. Xu, H. Guo, X. Cui, P. Wang, M. Lu, X. Xiao, Q. Guo, and B. Peng, "Magneto-optical effects of Ge-Ga-Sb(In)-S chalcogenide glasses with diamagnetic responses," *J. Am. Ceram. Soc.* **100**, 2914–2920 (2017).
126. P. Houizot, C. Boussard-Plédel, A. J. Faber, L. K. Cheng, B. Bureau, P. A. Van Nijnatten, W. L. M. Gielesen, J. Pereira Do Carmo, J. Lucas, J. R. P. Angel, A. Y. S. Cheng, N. J. Woolf, J. C. Flanagan, D. J. Richardson, M. J. Foster, I. Bakalski, E. Bonhomme, A. Pradel, J. E. Broquin, L. Labadie, and P. Kern, "Infrared single mode chalcogenide glass

- fiber for space," *Opt. Express* **15**, 12529 (2007).
127. H. Patrick, S. Frédéric, C. Vincent, T. Johann, and G. Ludovic, "Selenide glass single mode optical fiber for nonlinear optics," *Opt. Mater. (Amst)*. **29**, 651–656 (2007).
128. Y. Yu, B. Zhang, X. Gai, C. Zhai, S. Qi, W. Guo, Z. Yang, R. Wang, D.-Y. Choi, S. Madden, and B. Luther-Davies, ".8-10 μm mid-infrared supercontinuum generated in a step-index chalcogenide fiber using low peak pump power," *Opt. Lett.* **40**, 1081–1084 (2015).
129. V. S. Shiryaev, J. L. Adam, X. H. Zhang, C. Boussard-Plédel, J. Lucas, and M. F. Churbanov, "Infrared fibers based on Te-As-Se glass system with low optical losses," *J. Non. Cryst. Solids* (2004).
130. J. Qiu and K. Hirao, "The Faraday effect in diamagnetic glasses," *J. Mater. Res.* **13**, 1358–1362 (1998).
131. L. G. Aio, A. M. Efimov, and V. F. Kokorina, "REFRACTIVE INDEX OF CHALCOGENIDE GLASSES OVER A WIDE RANGE OF COMPOSITIONS," *J. Non. Cryst. Solids* **27**, 299–307 (1978).
132. E. Munin, J. A. Roversi, and A. B. Villaverde, "Faraday Effect and Energy Gap in Optical Materials," *J. Phys. D. Appl. Phys.* **25**, 1635–1639 (1992).